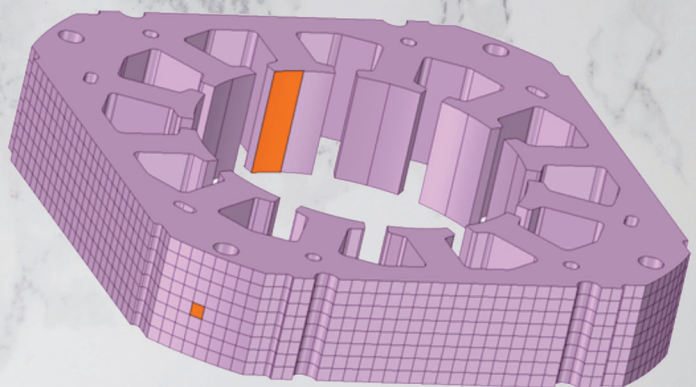
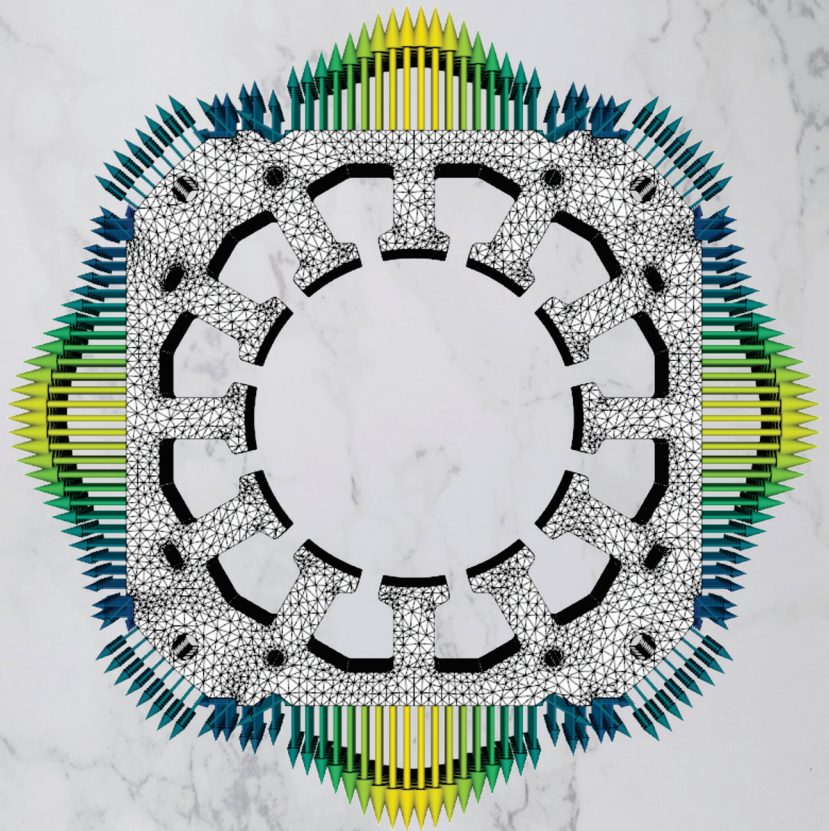




Strojniški vestnik

Journal of Mechanical Engineering



no. **9**

year **2019**

volume **65**

Strojniški vestnik – Journal of Mechanical Engineering (SV-JME)

Aim and Scope

The international journal publishes original and (mini)review articles covering the concepts of materials science, mechanics, kinematics, thermodynamics, energy and environment, mechatronics and robotics, fluid mechanics, tribology, cybernetics, industrial engineering and structural analysis.

The journal follows new trends and progress proven practice in the mechanical engineering and also in the closely related sciences as are electrical, civil and process engineering, medicine, microbiology, ecology, agriculture, transport systems, aviation, and others, thus creating a unique forum for interdisciplinary or multidisciplinary dialogue.

The international conferences selected papers are welcome for publishing as a special issue of SV-JME with invited co-editor(s).

Editor in Chief

Vincenc Butala

University of Ljubljana, Faculty of Mechanical Engineering, Slovenia

Technical Editor

Pika Škraba

University of Ljubljana, Faculty of Mechanical Engineering, Slovenia

Founding Editor

Bojan Kraut

University of Ljubljana, Faculty of Mechanical Engineering, Slovenia

Editorial Office

University of Ljubljana, Faculty of Mechanical Engineering

SV-JME, Aškerčeva 6, SI-1000 Ljubljana, Slovenia

Phone: 386 (0)1 4771 137

Fax: 386 (0)1 2518 567

info@sv-jme.eu, <http://www.sv-jme.eu>

Print: Papirografika, printed in 300 copies

Founders and Publishers

University of Ljubljana, Faculty of Mechanical Engineering, Slovenia

University of Maribor, Faculty of Mechanical Engineering, Slovenia

Association of Mechanical Engineers of Slovenia

Chamber of Commerce and Industry of Slovenia,

Metal Processing Industry Association

President of Publishing Council

Mitjan Kalin

University of Ljubljana, Faculty of Mechanical Engineering, Slovenia

Vice-President of Publishing Council

Bojan Dolšak

University of Maribor, Faculty of Mechanical Engineering, Slovenia

International Editorial Board

Kamil Arslan, Karabuk University, Turkey

Hafiz Muhammad Ali, University of Engineering and Technology, Pakistan

Josep M. Bergada, Politechnical University of Catalonia, Spain

Anton Bergant, Litoštroj Power, Slovenia

Miha Boltežar, University of Ljubljana, Slovenia

Filippo Cianetti, University of Perugia, Italy

Franci Čuš, University of Maribor, Slovenia

Janez Diaci, University of Ljubljana, Slovenia

Anselmo Eduardo Diniz, State University of Campinas, Brazil

Jožef Duhovnik, University of Ljubljana, Slovenia

Igor Emri, University of Ljubljana, Slovenia

Imre Felde, Obuda University, Faculty of Informatics, Hungary

Janez Grum, University of Ljubljana, Slovenia

Imre Horvath, Delft University of Technology, The Netherlands

Aleš Hribernik, University of Maribor, Slovenia

Soichi Ibaraki, Kyoto University, Department of Micro Eng., Japan

Julius Kaplunov, Brunel University, West London, UK

Iyas Khader, Fraunhofer Institute for Mechanics of Materials, Germany

Jernej Klemenc, University of Ljubljana, Slovenia

Milan Kljajin, J.J. Strossmayer University of Osijek, Croatia

Peter Krajnik, Chalmers University of Technology, Sweden

Janez Kušar, University of Ljubljana, Slovenia

Gorazd Lojen, University of Maribor, Slovenia

Thomas Lübben, University of Bremen, Germany

Jure Marn, University of Maribor, Slovenia

George K. Nikas, KADMOS Engineering, UK

Tomaž Pepelnjak, University of Ljubljana, Slovenia

Vladimir Popović, University of Belgrade, Serbia

Franci Pušavec, University of Ljubljana, Slovenia

Mohammad Reza Safaei, Florida International University, USA

Marco Sortino, University of Udine, Italy

Branko Vasić, University of Belgrade, Serbia

Arkady Voloshin, Lehigh University, Bethlehem, USA

General information

Strojniški vestnik – Journal of Mechanical Engineering is published in 11 issues per year (July and August is a double issue).

Institutional prices include print & online access: institutional subscription price and foreign subscription €100,00 (the price of a single issue is €10,00); general public subscription and student subscription €50,00 (the price of a single issue is €5,00). Prices are exclusive of tax. Delivery is included in the price. The recipient is responsible for paying any import duties or taxes. Legal title passes to the customer on dispatch by our distributor. Single issues from current and recent volumes are available at the current single-issue price. To order the journal, please complete the form on our website. For submissions, subscriptions and all other information please visit: <http://www.sv-jme.eu>.

You can advertise on the inner and outer side of the back cover of the journal. The authors of the published papers are invited to send photos or pictures with short explanation for cover content.

We would like to thank the reviewers who have taken part in the peer-review process.

The journal is subsidized by Slovenian Research Agency.

Strojniški vestnik - Journal of Mechanical Engineering is available on <https://www.sv-jme.eu>.



Cover:

Vibration response of stator in the surfaces' normal direction due to the electromagnetic excitation forces on stator teeth. Vibration response is calculated in the frequency domain based on response model, which is calculated for 3D mechanical FE model of stator shown on the lower part of the figure.

Image courtesy:

University of Ljubljana, Faculty of Mechanical Engineering, Laboratory for Dynamics of Machines and Structures (LADISK), Slovenia

ISSN 0039-2480, ISSN 2536-2948 (online)

© 2019 Strojniški vestnik - Journal of Mechanical Engineering. All rights reserved. SV-JME is indexed / abstracted in: SCI-Expanded, Compendex, Inspec, ProQuest-CSA, SCOPUS, TEMA. The list of the remaining bases, in which SV-JME is indexed, is available on the website.

Contents

Strojniški vestnik - Journal of Mechanical Engineering
volume 65, (2019), number 9
Ljubljana, September 2019
ISSN 0039-2480

Published monthly

Papers

Janez Luznar, Janko Slavič, Miha Boltežar: Structure-Borne Noise at PWM Excitation Using an Extended Field Reconstruction Method and Modal Decomposition	471
Mario Sokac, Djordje Vukelic, Zivana Jakovljevic, Zeljko Santosi, Miodrag Hadzistevic, Igor Budak: Fuzzy Hybrid Method for the Reconstruction of 3D Models Based on CT/MRI Data	482
Wojciech Depczyński: Selected Microstructural and Mechanical Properties of Open-Cell Metal Foams	495
Shahin Ghanbari, Kouros Javaherdeh: Experimental Assessment of Turbulence Convective Heat Transfer and Pressure Drop in Annuli Using Nanoporous Graphene Non-Newtonian Nanofluid	503
Min Song, Hongliang Wang, Haiou Liu, Pai Peng, Xianhui Wang, Dawei Pi, Chen Yang, Gang He: Double-layer Control of an Automatic Mechanical Transmission Clutch during Commercial Vehicle Start-up	515
Branko Nečemer, Matej Vesenjajk, Srečko Glodež: Fatigue of Cellular Structures – a Review	525

Structure-Borne Noise at PWM Excitation Using an Extended Field Reconstruction Method and Modal Decomposition

Janez Luznar¹ – Janko Slavič^{2,*} – Miha Boltežar²

¹Domel, d.o.o., Slovenia

²University of Ljubljana, Faculty of Mechanical Engineering, Slovenia

Pulse-width modulation (PWM) represents a carrier-frequency-dependent structural excitation. The PWM's excitation harmonics are also reflected in the air gap's electromagnetic forces, the vibration response and the resulting structure-borne noise. The last of these can be numerically predicted with a multiphysics finite element analysis (FEA) containing electronic, electromagnetic, mechanical and acoustic field problems. The multiphysics FEA are precise, but computationally inefficient and consequently inadequate for parametric studies. This paper introduces a method for a fast structure-borne noise prediction at PWM excitation. The presented approach contains the Extended field reconstruction method (EFRM) to handle the magnetic saturation and slotting effects in magnetics, and the modal decomposition to couple the electromagnetic and mechanical domains. Finally, the structure-borne sound power level is calculated via the vibration-velocity response. Indeed, this approach demands a pre-calculation of the basis functions and modal parameters from the FEA, but afterwards the effect of the different PWM excitation cases can be evaluated in a few seconds. The proposed method can calculate the structure-borne noise at PWM excitation accurately and is more than 10^4 times faster than the conventional multiphysics FEA approach.

Keywords: carrier frequency, electromagnetic forces, extended field reconstruction method, modal decomposition, structure-borne noise

Highlights

- The structure-borne noise of PWM controlled machines can be reduced by the appropriate carrier-frequency selection in accordance with the structural dynamics.
- Based on the extended field reconstruction method, a fast method for structure-borne noise prediction at PWM excitation is introduced.
- The proposed method was shown to calculate the structure-borne noise at custom PWM excitation accurately and efficiently.
- Parametric study with densely spaced PWM carrier-frequency show a 30 dB(A) difference in total sound power level.

0 INTRODUCTION

In permanent-magnet synchronous motor (PMSM) the variable speed can be controlled by pulse-width modulation (PWM), which composes current waveforms of the desired fundamental frequency component together with a number of higher switching harmonics [1]. The latter enriches the Maxwell force spectrum, escalating the vibrations and the noise of electromagnetic origin [2]. Electromagnetic noise depends on the different motor types, motor powers, rotor speeds, PWM techniques and the carrier frequency [3]. The influence of the PWM carrier frequency on the structure-borne noise was experimentally researched in [4], where densely spaced carrier frequency measurements indicated a strong variation in the total emitted noise. However, the influence of the PWM carrier frequency on the structure-borne noise can also be estimated numerically, as shown in this article.

An accurate assessment of the noise in electrical machines requires a multiphysics analysis encompassing electronic, electromagnetic, mechanical and acoustic field problems, which can be solved

by using an analytical or a numerical approach. Analytical methods allow quick computation, but suffer from poor accuracy and are usually limited to simple geometries [5] to [7]. In contrast, a finite element analysis (FEA) can obtain accurate results, but requires substantial computational resources [8] to [10]. The most time-consuming part in this multiphysics analysis is the electromagnetic transient simulation, which can be replaced with the computationally efficient field reconstruction method (FRM).

The FRM utilizes the field generated by one stator slot and a permanent magnet (PM) over one pole to construct the entire field distribution in the air gap [11]. Therefore, by using the FRM, the magnetic flux density for an arbitrary stator current excitation can be reconstructed efficiently. Sutthiphornsombot et al. [12] used the FRM to compute the electromagnetic forces and employed an optimization method to minimize the force pulsation and consequently reduce the acoustic noise. However, the coupling between the electromagnetic and the structural model was not involved. Furthermore, Torregrossa et al. [13] proposed an efficient computational model for a fast

*Corr. Author's Address: University of Ljubljana, Faculty of Mechanical Engineering, Aškerčeva 6, SI-1000 Ljubljana, Slovenia, janko.slavic@fs.uni-lj.si

and accurate calculation of the electromagnetically induced vibrations in a PMSM using the FRM and knowledge of the mechanical impulse response. The vibration response was calculated with a convolution of the excitation force and the mechanical impulse response, which could be better handled directly in the frequency domain by using a frequency-response matrix.

The listed investigations show the great usefulness of the FRM, which reduces the computation time compared to the FEA, but is only applicable within the linear magnetic region of ferromagnetic materials [11]. To consider the magnetic saturation and slotting effects, an extended field reconstruction method (EFRM) was recently introduced by Gu et al. [14], where the field density distribution in the air gap can be reconstructed by using a set of pre-calculated basis functions. Comparisons with the FEA showed that the EFRM has an acceptable accuracy and takes significantly less time to compute [14]. However, there is a lack of vibro-acoustic investigations using the EFRM, which could expand the usage of previously investigated FRM-based methods.

The aim of this investigation is to establish a fast multiphysics numerical modeling of the structure-borne noise at PWM excitation. The proposed method is programmed with our own code and includes FEA imports, necessary for the EFRM and the structural model calculations. The manuscript is organized as follows. Section 1 presents the conventional method to simulate the structure-borne noise at PWM excitation with the multiphysics FEA. Section 2 presents the steps of the proposed fast multiphysics numerical simulation method, based on the EFRM and the modal decomposition. Section 3 shows the case study and the validation of the proposed method with the FEA. Section 4 shows the parametric study at different PWM excitations to emphasize the computational efficiency. Section 5 draws the conclusions.

1 SIMULATION USING FINITE ELEMENT ANALYSES

The conventional method to simulate structure-borne noise at PWM excitation, which is used later to compare the results to the newly proposed approach, is made with a multiphysics FEA containing all these domains:

- Electronic model: controlling the power electronics to generate a 3-phase PWM voltage excitation.
- Electrical model: the voltage excitation will cause electrical currents in the 3-phase windings,

inducing spatially distributed electromagnetic flux waves in the air-gap of the motor.

- Electromagnetic model: the induced rotating flux density waves will cause both the tangential and radial force components generating the motor torque and unwanted vibrations.
- Structural model: the response of the structure depends on the frequency harmonics of the electromagnetic forces and the corresponding structural behavior of the motor.
- Acoustic model: surface vibrations will cause the pressure variations in the surrounding air, leading to radiated acoustic noise.

Different models can be weakly coupled since there is no significant feedback from the mechanical domain to the electromagnetic domain, and also none from the acoustic domain to the mechanical domain [15]. The case study presented in Section 3 is modelled with the commercial software package ANSYS 18.1 using the following modules:

1.1 Simplorer and Maxwell

A co-simulation with Maxwell and Simplorer is used to link the electromagnetic model with the electrical circuit for a 3-phase voltage-source inverter, as shown in Fig. 1. Transient simulation at PWM voltage excitation demands a small time step ($\leq 1 \mu s$) to obtain the well-discretized PWM voltage pulses and, therefore, the appropriate frequency domain of the electromagnetic forces. To analyze the machine in a steady state, a transient simulation must accomplish at least a few electric cycles (at least 3 for the case study in Section 3). The electromagnetic forces acting on the tips of the stator's teeth are calculated within the last simulation cycle and transformed in the frequency domain for further analyses.

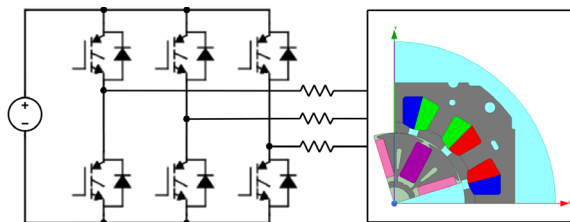


Fig. 1. Co-simulation using Maxwell and Simplorer in ANSYS 18.1

1.2 Modal and Harmonic Response

The Modal analysis and Harmonic response modules are used to couple the electromagnetic forces and the structural model, resulting in vibrational and

acoustic responses, as shown in Fig. 2. The Modal analysis of the 3D mechanical model is used to obtain the structural dynamics parameters, i.e., the mode shapes, mode frequencies and mode damping, which represent the basis for further response calculations. By importing the modal results and the excitation magnetic forces, the vibration-velocity response is calculated with the Harmonic response module using the mode-superposition method. Finally, the vibration-velocity response of all the external surfaces is imported into another Harmonic Response module to simulate the acoustics and to calculate the sound power level of the structure-borne noise.

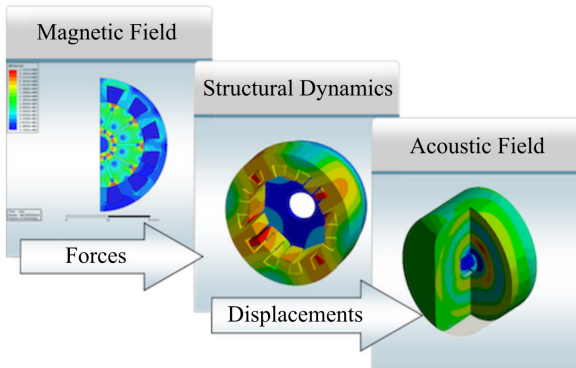


Fig. 2. Using the modal analysis and Harmonic response modules to calculate the vibration response and simulate acoustics in ANSYS 18.1

2 FAST MULTIPHYSICS SIMULATION METHOD, BASED ON EFRM AND MODAL DECOMPOSITION

As the conventional FEA multiphysics simulation is time consuming, an efficient multiphysics method, combining the EFRM and modal decomposition, is proposed in this investigation. The EFRM has been used to model the electric and electromagnetic domains, while the vibration velocity is calculated with the mechanical response model, defined by the modal decomposition. This approach requires some data pre-calculation from the FEA, but then the structure-borne noise at custom PWM excitation can be predicted efficiently.

2.1 Custom PWM Excitation

The PWM time domain presents a sequence of positive and negative voltage pulses, which result in a broadband frequency excitation. The program code to generate the PWM phase excitations (u_a, u_b, u_c) for different PWM parameters, i.e., carrier type, carrier frequency, fundamental frequency and

amplitude, was developed from scratch [4]. The PWM excitation frequency contents involve the fundamental component f_1 with additional switching harmonics at the frequencies f_h [16]:

$$f_h = n \cdot f_c \pm k \cdot f_1, \tag{1}$$

where $n=1,2,3,\dots$, and f_c is the carrier frequency. When n is odd, $k=\pm 2, \pm 4, \dots$, and when n is even, $k=\pm 1, \pm 5, \dots$. Fig. 3 shows the voltage harmonics for sine-triangle PWM with the fundamental at 100 Hz and the carrier frequency at 3000 Hz.

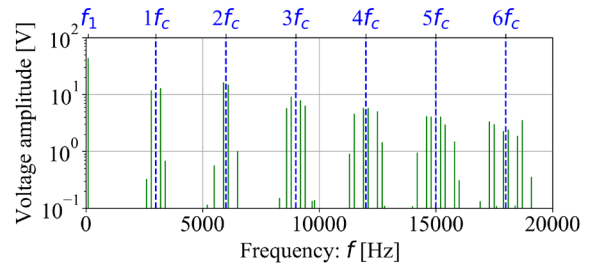


Fig. 3. Frequency contents for a sine-triangle PWM

2.2 Electric Model of the PMSM

In order to implement the EFRM, the 3-phase quantities (voltages, currents and flux linkages) are transformed into the dq rotor reference frame, as shown for the voltages in Eq. (2) using the transformation matrix T , defined in Eq. (3):

$$\begin{bmatrix} u_d \\ u_q \end{bmatrix} = T \cdot \begin{bmatrix} u_a \\ u_b \\ u_c \end{bmatrix}, \tag{2}$$

$$T = \frac{2}{3} \begin{bmatrix} \cos(\theta) & \cos\left(\theta - \frac{2\pi}{3}\right) & \cos\left(\theta + \frac{2\pi}{3}\right) \\ -\sin(\theta) & -\sin\left(\theta - \frac{2\pi}{3}\right) & -\sin\left(\theta + \frac{2\pi}{3}\right) \end{bmatrix}, \tag{3}$$

where u_d, u_q are the d and q components of the stator voltage vector, θ is the angle between the stator fixed a axis and the rotor rotating d axis. The vector representation of the transformation is presented in Fig. 4, where ω_e is the synchronous electrical speed. The a axis points towards the center of the flux linkage A , the d axis is pointed at the center of the PM, and the q axis is defined as being 90 electrical degrees ahead of the d axis.

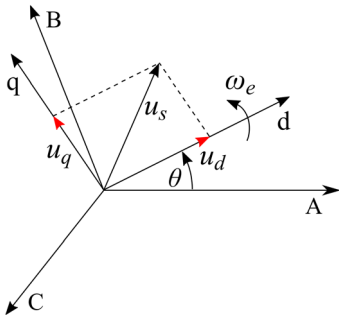


Fig. 4. Vector representation of the *abc* to *dq* frame transformation

The voltage equations of the PMSM in the rotor reference *dq*-axis frame are defined in Eq. (4) [17]:

$$\begin{bmatrix} u_d \\ u_q \end{bmatrix} = \begin{bmatrix} R_s + pL_d & -\omega_e L_q + pL_{dq} \\ \omega_e L_d + pL_{qd} & R_s + pL_q \end{bmatrix} \begin{bmatrix} i_d \\ i_q \end{bmatrix} + \begin{bmatrix} 0 \\ \omega_e \psi_m \end{bmatrix}, \quad (4)$$

where i_d , i_q , L_d , L_q , L_{dq} , L_{qd} are the *d* and *q* axis currents, self and mutual inductances, respectively. R_s is the phase resistance, ψ_m is the flux linkage due to the permanent magnets and $p = d/dt$. Like in [18], we used the field components in the air gap to estimate the flux linkages, which can be calculated by integrating the radial flux density B_n under each stator phase i [18] and [19]:

$$\psi_i = PN \int_0^{2\pi/P} B_n L_{sk} r d\theta, \quad i = a, b, c, \quad (5)$$

where P represents the number of magnetic pole pairs, N is the number of conductors in each coil, L_{sk} is the stack length and r is the radius of the closed contour in the air-gap. Furthermore, the values of ψ_d and ψ_q can be defined using the transformation matrix, Eq. (3). The incremental self and mutual inductances can be then determined according to Eq. (6):

$$\begin{aligned} L_d &= \partial \psi_d / \partial i_d, & L_{dq} &= \partial \psi_d / \partial i_q, \\ L_{qd} &= \partial \psi_q / \partial i_d, & L_q &= \partial \psi_q / \partial i_q. \end{aligned} \quad (6)$$

As shown in Section 2.3, the magnetic flux density can be reconstructed using the EFRM. Therefore, the flux linkages and inductances can also be calculated with Eqs. (3), (5) and (6). Lastly the custom PWM voltage excitation causes the transient currents i_d and i_q , which can be numerically calculated step-by-step using the electrical model, Eq. (4) together with magnetic coupling, which is included via the EFRM based flux linkages and inductances.

2.3 Magnetic Field Reconstruction with EFRM

The FRM enables an efficient calculation of the normal and tangential flux densities in the air gap,

assuming that the ferromagnetic material operates in a linear magnetic region. This is not the case for an interior mounted PMSM (IPMSM), which includes the saturation effect. The latter can be considered with an extended FRM, introduced by Gu et al. [14]. Unlike the traditional FRM, the EFRM considers the stator and rotor flux at the same time. The flux linkage in the air gap is decoupled into the *d* and *q* axis fluxes and the saturation effects in these two directions are modeled independently [19]. The *d* axis flux density is the result of both the I_d and PM flux, while the *q* axis flux density originates only from I_q and is obtained after replacing the PM with air. The flux densities in the *d* and *q* axis (B_d , B_q) are obtained using the decoupling principle, Eq. (7) [14]:

$$\begin{aligned} B_d &= B_{dn} + B_{dt}, & I_q &= 0, \\ B_q &= B_{qn} + B_{qt}, & I_d &= 0, & PM &= 0, \end{aligned} \quad (7)$$

where B_{dn} , B_{dt} , B_{qn} , B_{qt} represent their normal and tangential components, and the I_d , I_q single current values. While neglecting the cross-coupling effect between the *d* and *q* axis, the normal and tangential components of the flux density distributions (B_n , B_t) can be expressed as a superposition of the *d* and *q* axis flux densities:

$$\begin{aligned} B_n &= B_{dn} + B_{qn}, \\ B_t &= B_{dt} + B_{qt}. \end{aligned} \quad (8)$$

As seen from Eq. (8), the EFRM reconstructs the flux density components B_n and B_t by summing their *d* and *q* contributions, Eq. (7). These are treated separately and depend on the flux density distributions along the air-gap contour, which are pre-calculated with FEA and stored as a basis functions. The latter represent a look-up table including B_{dn} , B_{qn} , B_{dt} , B_{qt} distributions along the air-gap contour at different rotor positions to take into account the spatial machine harmonics and different I_d or I_q current levels to consider the saturation effect. With the basis functions, the magnetic field density distribution at any rotor position with any current values lower than rated can be interpolated and rebuilt according to Eq. (8).

2.4 Electromagnetic Forces

The electromagnetic forces in electrical machines can be calculated with the Maxwell stress tensor (MST) method, which provides a detailed local force distribution. According to the MST, the tangential and normal force densities in the air gap can be expressed as [11] and [12]:

$$f_t = \frac{1}{\mu_0} (B_n B_t), \quad (9)$$

$$f_n = \frac{1}{2\mu_0} (B_n^2 - B_t^2), \quad (10)$$

where μ_0 is the permeability of air. The cumulative tangential and radial forces acting on the tip of each stator tooth k can be computed by integrating the force density components Eqs. (9) and (10) over the respective surface area S_k :

$$F_{k,t} = \int_{S_k} f_t dS_k, \quad (11)$$

$$F_{k,n} = \int_{S_k} f_n dS_k. \quad (12)$$

2.5 Vibration Response Using Modal Decomposition

The dynamics of an arbitrary system with N degrees of freedom (DOF) is determined by the equation of motion in the time domain [20]:

$$\mathbf{M}\ddot{x}(t) + \mathbf{D}\dot{x}(t) + \mathbf{K}x(t) = \mathbf{f}(t), \quad (13)$$

where \mathbf{M} , \mathbf{D} , \mathbf{K} are the mass, damping and stiffness matrices, $x(t)$ is the displacement, $\dot{x}(t)$ is the velocity and $\ddot{x}(t)$ is the acceleration vector. The excitation forces are denoted by $\mathbf{f}(t)$. Using a Fourier transformation, Eq. (13) can be transformed into the frequency domain as:

$$[-\omega^2 \mathbf{M} + i\omega \mathbf{D} + \mathbf{K}] \mathbf{X}(\omega) = \mathbf{F}(\omega), \quad (14)$$

where ω represents the angular velocity, i the imaginary unit and $\mathbf{X}(\omega)$, $\mathbf{F}(\omega)$ the response and excitation vectors in the frequency domain, whose amplitudes are complex numbers characterizing the amplitude as well as the phase delay. Eq. (14) can be further rewritten into the response model [21]:

$$\mathbf{X}(\omega) = \mathbf{H}(\omega) \mathbf{F}(\omega), \quad (15)$$

where the response matrix $\mathbf{H}(\omega)$ contains all the combinations of the Frequency response function (FRF) between the input excitations and the output response points, as shown in Eq. (16):

$$\mathbf{H}(\omega) = \begin{bmatrix} H_{11}(\omega) & H_{12}(\omega) & \cdots & H_{1N}(\omega) \\ H_{21}(\omega) & H_{22}(\omega) & \cdots & H_{2N}(\omega) \\ \vdots & \vdots & \ddots & \vdots \\ H_{N1}(\omega) & H_{N2}(\omega) & \cdots & H_{NN}(\omega) \end{bmatrix}. \quad (16)$$

The individual displacement FRF $H_{jk}(\omega)$ of a response point j to an excitation at point k is defined as [20]:

$$H_{jk}(\omega) = \sum_{r=1}^N \left(\frac{{}_r A_{jk}}{i\omega - \lambda_r} + \frac{{}_r A_{jk}^*}{i\omega - \lambda_r^*} \right), \quad (17)$$

where ${}_r A_{jk} = \phi_{jr} \phi_{kr}$ is the modal constant, ϕ_r is the mass-normalized eigenvector of mode r , λ_r are the system eigen-values containing the angular eigenfrequencies ω_r and the damping ratios ζ_r according to:

$$\lambda_r = -\zeta_r \omega_r \pm i\omega_r \sqrt{1 - \zeta_r^2}. \quad (18)$$

The formulation of Eq. (17) indicates the modal decomposition, where the response equals the sum of the modes (λ_r , ${}_r A_{jk}$) and their complex conjugates (λ_r^* , ${}_r A_{jk}^*$). Finally, the vibration velocity vector $\mathbf{v}(\omega)$, i.e., the time derivative of the displacement vector $\mathbf{X}(\omega)$ is expressed in the frequency domain using Eq. (15) as:

$$\mathbf{v}(\omega) = i\omega \cdot \mathbf{H}(\omega) \mathbf{F}(\omega). \quad (19)$$

2.6 A-Weighted Airborne Sound Power Level

The A-weighted airborne sound power radiated by a machine caused by the structure vibrations of its outer surface P_A is determined with ISO/TS 7849-1 [22]:

$$P_A = \sigma \rho c S \bar{v}_a^2, \quad (20)$$

where σ represents the radiation efficiency, ρ is the air density, c is the speed of sound in the air, and \bar{v}_a^2 is the squared spatial average of the A-weighted vibration velocity component perpendicular to the outer surface of the machine S . Eq. (20) can be rewritten for the surface segments S_j and their A-weighted normal velocity components v_{aj} and thus the A-weighted sound power level L_{WA} can be calculated with Eq. (21), where the reference value P_0 is 10^{-12} W:

$$L_{WA} = 10 \log \frac{\sigma \rho c \sum S_j v_{aj}^2}{P_0}. \quad (21)$$

3 CASE STUDY: PWM EXCITATION OF THE IPMSM

Section 2 shows the steps of the proposed method, which are programmed with our own code and used in the case study. This method requires a pre-calculation of the basis functions and the modal parameters, which are imported from the commercial FEA, but afterwards the effect of different PWM excitation cases can be evaluated within a few seconds. To

prove the credibility of the proposed method, the same case study is also set up with commercial FEA tools, presented in Section 1. Then the results of both approaches are compared, and the main advantage of the proposed method, i.e., computational efficiency, is emphasized. All the calculations are made on the same desktop computer with an Intel Core i7 2.5-GHz CPU and 16 GB RAM.

The IPMSM used for the case study involves partial magnetic saturation, which can be considered with the EFRM. The main parameters of the used IPMSM are listed in Table 1. The rated value of the phase current is 3.6 A; therefore, the basis function is obtained at different I_d and I_q values, within ± 5 A. Details of the 2D electromagnetic and 3D mechanical models are presented in Sections 3.1 and 3.2.

Table 1. Main parameters of the used IPMSM

Outer diameter of stator	135 mm
Inner diameter of stator	65.8 mm
Number of stator slots	12
Stator / rotor material	M400-50A
Rotor diameter	65 mm
Thickness of magnet	8 mm
Magnet remanence	0.4 T
Stack length	22 mm
Airgap length	0.4 mm
Number of phases	3
Number of coil turns	116
Rated current	3.6 A
Rated torque	1.7 Nm
Rated speed	1500 RPM

3.1 2D Electromagnetic Model

Fig. 5 shows the 2D electromagnetic finite element (FE) model. The flux-density variation repeats every 3 stator teeth; therefore, only one-quarter of the IPMSM needs to be considered to obtain the complete flux-density distribution. As shown in Fig. 5, the rotor rotates anticlockwise and contains permanent magnets, whereas the stator is fixed and contains 3-phase windings (A, B, C). The rotor and stator generate the common rotating magnetic field.

The 2D electromagnetic FE model is used to obtain the basis functions for the EFRM and is also included in the conventional multiphysics FEA approach. The basis functions in this case study are spatially discretized with 900 points along the air-gap and obtained for 400 different rotor positions (to include the spatial machine harmonics) and 21 different current levels I_d or I_q from -5 A to 5 A (to

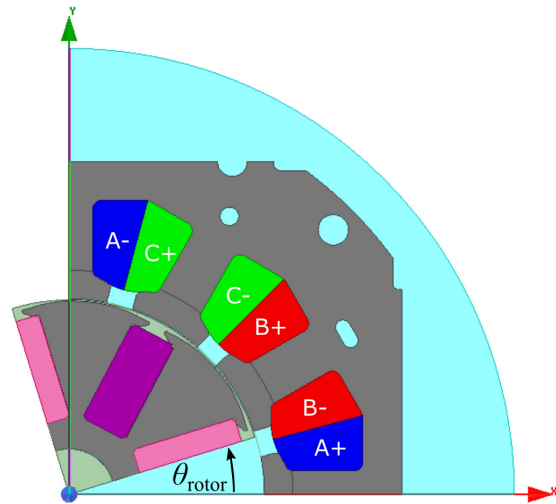


Fig. 5. 2D electromagnetic FE model

consider the saturation effect). The whole basis functions are pre-calculated in 42 h. By using the basis functions, the flux-density distribution at any rotor position with any current value lower than the rated current can be interpolated and rebuilt with Eqs. (7) and (8). Fig. 6 shows the basis functions at rotor position 0° contributed by the d axis flux, which are

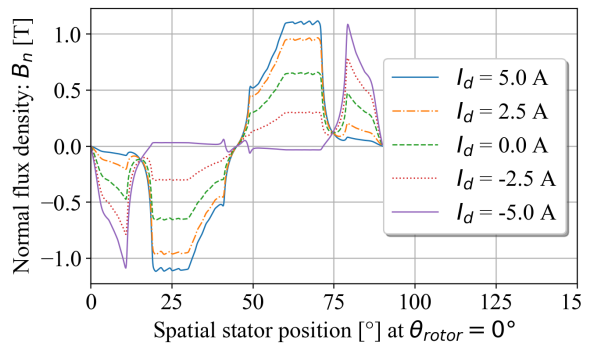


Fig. 6. Radial flux density distribution contributed by I_d

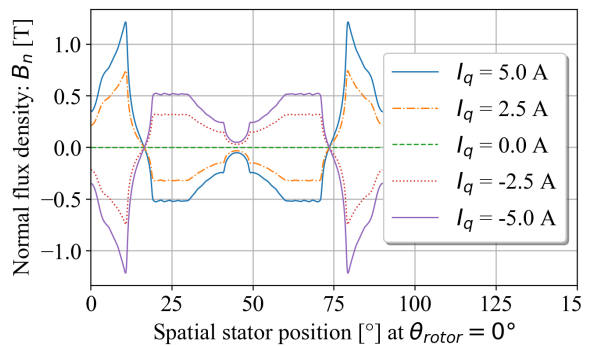


Fig. 7. Radial flux density distribution contributed by I_q

the result of both the PM and the different I_d current. The curve at $I_d = 0$ A represents the flux-density distribution due to the PM flux only. The curves in Fig. 6 show that the PM flux density distribution increases with positive I_d and decreases with negative I_d . The curve at $I_d = 5$ A indicates the saturation effect, since the increment of the flux density is degraded compared to the curve at $I_d = 2.5$ A. Similarly, Fig. 7 shows the basis function at rotor position 0° for different I_q currents without considering the d axis flux. The flux density at $I_q = 0$ A represents the zero array, while the positive and negative I_q values result in the opposite magnetic flux distribution.

The EFRM was validated with a co-simulation using Maxwell and Simplorer in the ANSYS commercial package. The tested case used PWM voltage excitation with the fundamental component at a frequency of 100 Hz and a switching frequency at 3000 Hz, shown in Fig. 3. To compare the results in steady state at least 3 electrical cycles must be accomplished. Using a small time step ($1 \mu\text{s}$) results in $3 \cdot 10000 = 30000$ steps, which are computed in 75 h

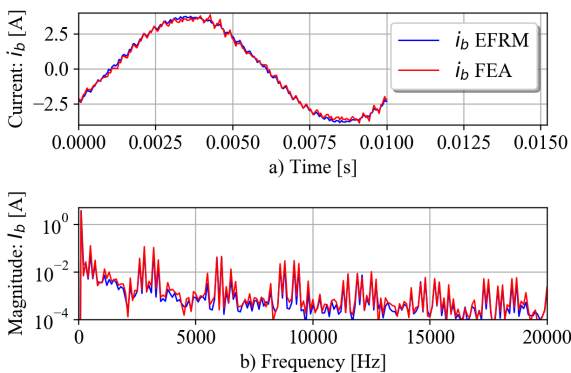


Fig. 8. Phase current at PWM excitation in a) time domain and b) in the frequency domain

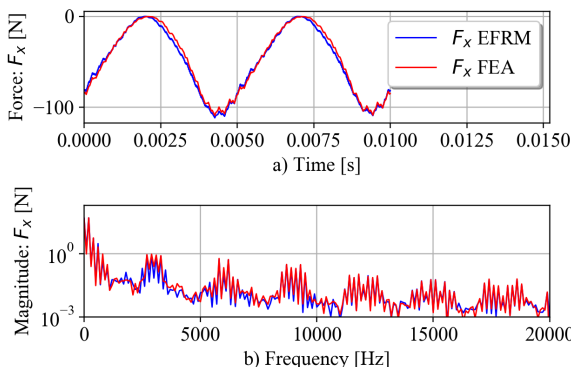


Fig. 9. Magnetic force at PWM excitation in a) time domain and b) in the frequency domain

with a 2D electromagnetic FEA or 3 s with the EFRM. Figs. 8 and 9 show the resulting phase current and magnetic force in the time and frequency domains. The frequency-domain contents show that the PWM switching harmonics are also transmitted in the phase current and magnetic force. Although the EFRM is approximate, good agreement with the FEA results is seen with respect to both the time and frequency domains.

3.2 3D Mechanical Model

The electromagnetic and mechanical models are coupled with a response model. The latter can be calculated using exported modal data from the FEA. A 3D mechanical FE model is meshed with almost 120,000 nodes, but the response model can be reduced since the only needed FRFs are between the excitation and response locations, shown in Fig. 10:

- *Excitation locations*
The air-gap force density around each stator-tooth tip causes the resultant net force and torque on its center. To involve both excitation type sources, every stator-tooth tip surface is halved, containing the net force on both halves. The stator has 12 teeth and therefore 24 excitation locations (index k).
- *Response locations*
The size of the response surfaces is defined in accordance with the well-known six-elements-per-wavelength criterion [23]. To predict the noise up to 20 kHz, the maximum response surface length should be less than one-sixth of the corresponding wavelength, which is around 2.8 mm. As shown in Fig. 10, the model contains 1360 response locations on its outer surface (index j).

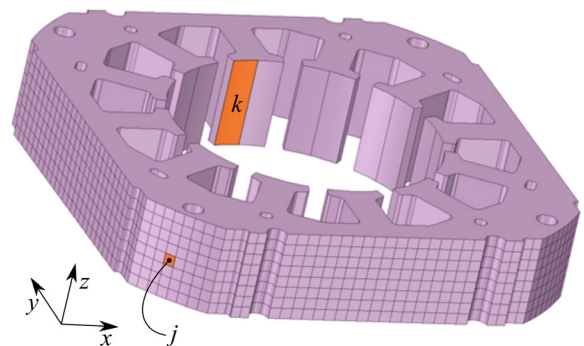


Fig. 10. 3D mechanical FE model of the stator

Using the modal decomposition, the response matrix Eq. (16) is described in terms of modal

shapes, frequencies and damping. The modal data are imported from the commercial FEA only for the selected locations, forming the reduced response model. Thus, the length of the array for the reduced response matrix is $24 \cdot 1360 \cdot 3 \cdot 3 = 293760$, where the last two multipliers stands for the 3 excitation directions of each excitation location and the 3 response directions of each response location. After importing the modal data, all these displacement FRFs are calculated using Eq. (17) in 3 minutes. It should be noted that the FRFs are calculated only once and then reused for coupling different PWM excitations with structural dynamics.

Fig. 11 shows an example of the displacement FRF $H_{jx,ky}(\omega)$ of a response point j in the x direction to an excitation at point k in the y direction, which are marked in Fig. 10. The FRF curve, calculated with modal decomposition (MD), was also validated by using the Harmonic response module in the ANSYS 18.1.

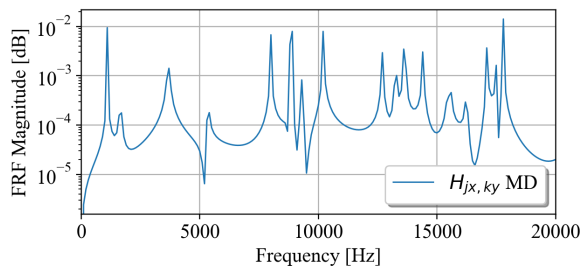


Fig. 11. FRF $H_{jx,ky}(\omega)$ from the stator-tooth tip “ k ” to the outer subsurface “ j ”

3.3 Vibration Response and Sound Power Level

Similarly as shown in Fig. 9 for single magnetic force, now magnetic forces are calculated for all 24 excitation locations in three coordinate directions (x, y, z) and transformed in the frequency domain to build the force excitation vector $F(\omega)$. By using the force excitation vector and the response matrix, Eq. (16), the vibration-velocity response vector is calculated efficiently with matrix multiplication, Eq. (19). Fig. 12 shows the vibration-velocity response in the x direction for location j , including both, the EFRM-MD and FEA results. The frequency contents in both curves are in a good agreement, showing that the proposed method approximates the FEA results with a small error.

Further, the vibration-velocity response vector, calculated for all the response locations in three coordinate directions (x, y, z), is transformed in the surfaces’ normal direction, shown in Fig. 13. These

vibration-velocity components represent the input for the acoustic field simulation, e.g., using the boundary-element method [15]. However, by using the outer surface segments S_j and the vibratory components perpendicular to them v_{aj} , the sound power level can also be estimated via Eq. (21). Fig. 14 shows the sound power level calculated with the FEA and with Eq. (21) using the radiation efficiency $\sigma = 1$. This assumption leads to a conservative estimate of the radiated air-borne sound power, but it is valid at higher frequencies [24]. Since the article is focused on the high-frequency PWM switching noise, the presented estimation of the sound power level is acceptable.

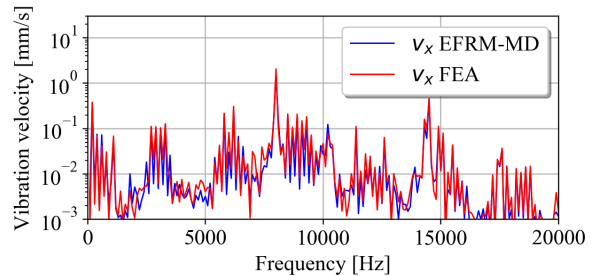


Fig. 12. Vibration response at PWM excitation in the frequency domain

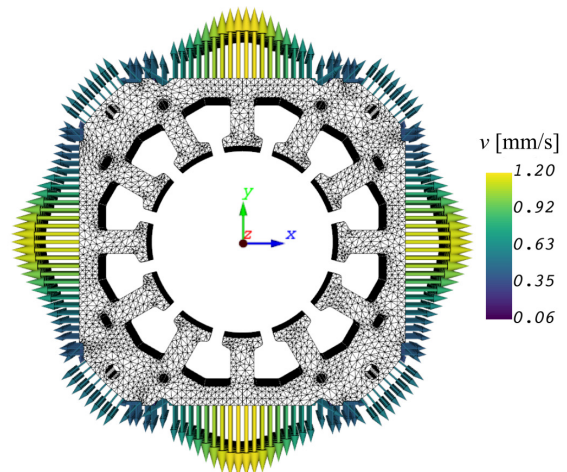


Fig. 13. Vibration response in the surfaces’ normal direction

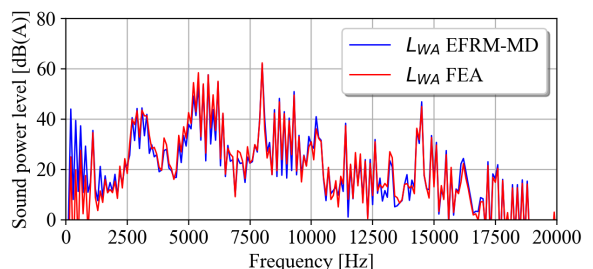


Fig. 14. Sound power level at PWM excitation in the frequency domain

4 PARAMETRIC STUDY AND COMPUTATIONAL EFFICIENCY

The proposed method enables a fast sound power level estimation and therefore a parametric study can be made within a few minutes. To show the computational efficiency, an example with many different PWM excitations is used, where each contains the same fundamental component, but a different PWM carrier frequency. The included PWM excitations result in the same motor speed and torque, but contain different PWM switching harmonics, Eq. (1). The proposed approach is used for different PWM excitations to estimate the total sound power level. Its dependency on the PWM carrier frequency is shown in Fig. 15, which contains 197 different excitation cases (400 Hz, 500 Hz, ..., 20000 Hz). The excitation case, where any of the PWM switching harmonics excite the stator natural frequency, results in greater noise. However, there are also excitation cases where the PWM switching harmonics interact with the anti-resonant regions in the FRF curves (Fig. 11), resulting in low total sound power levels. Fig. 15 shows that an appropriate PWM carrier frequency can decrease the total sound power level by more than 30 dB(A).

To prove the general usage of the proposed approach, a few characteristic excitation cases were validated also with FEA, shown with black markers in Fig. 15. Mean difference in total sound power level between the proposed method and the FEA results is 1.5 dB(A), while the standard deviation is 0.8 dB(A).

Good agreement proving that carrier-frequency selection has a great impact on structure-borne noise.

The main advantage of the proposed method is the computational efficiency. At the beginning the basis functions and the modal data must be pre-calculated using the FEA, which takes around 43 h, but then the sound power level for any PWM excitation can be calculated in a few seconds. For example, the curve in Fig. 15 contains 197 different excitations and is calculated in 10 minutes. The same parametric study using only the conventional FEA tools in an identical computational platform would take more 600 days, i.e., $197 \cdot 75 \text{ h} = 14775 \text{ h}$.

5 CONCLUSION

This article introduces a fast multiphysics numerical modeling of the structure-borne noise at PWM excitation. Firstly, the PWM excitation is used with the EFRM to obtain the electromagnetic forces on the tips of the stator teeth. Then these electromagnetic forces are coupled with the structural model to calculate the vibration-velocity response. The coupling between the electromagnetic and mechanical domains is made with the response model, which can be calculated directly in the frequency domain. Finally, the vibration-velocity response of all the outer surfaces is used to estimate the sound power level of the structure-borne noise. To prove the credibility, each step of the method is validated with the corresponding FEA.

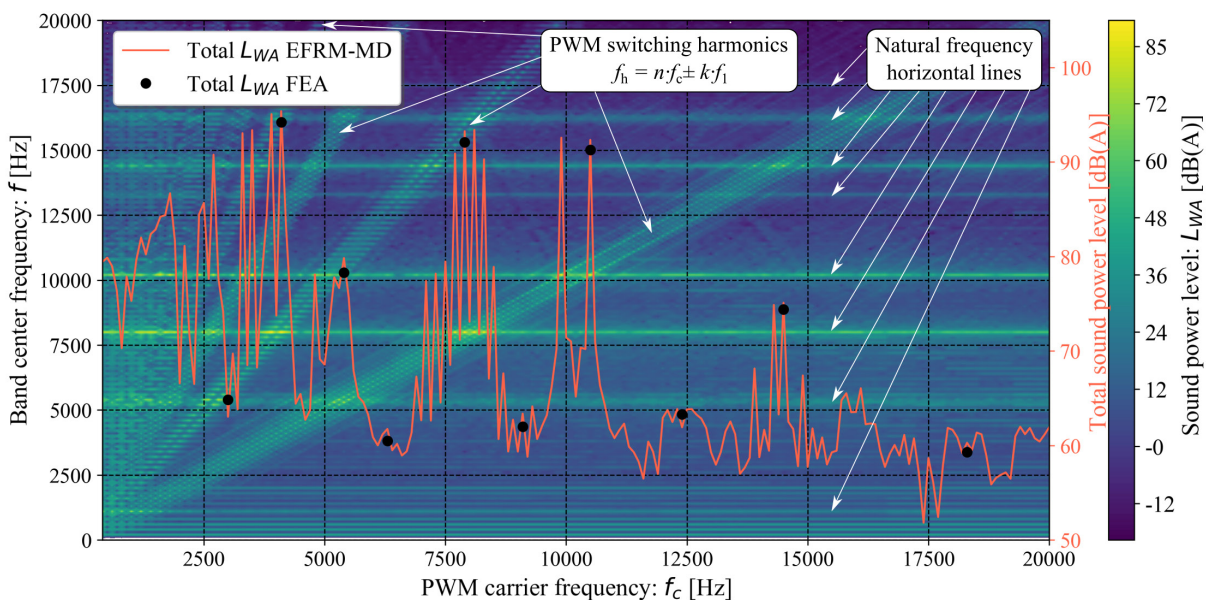


Fig. 15. Parametric study: L_{WA} at different PWM carrier frequencies

Detailed influence of the PWM carrier frequency on the structure-borne noise has been researched experimentally already before, but proposed manuscript shows how it can be estimated also numerically. Other researchers used different analytical and numerical approaches, where the first are less accurate but the second are time consuming. Instead of electromagnetic FEA an efficient EFRM can be used. EFRM was proposed in 2016, but we upgraded and validated it into the multiphysics method to calculate the structure-borne noise accurately and efficiently. If the data pre-calculation is not taken into account, the proposed method is more than 10^4 times faster than a conventional multiphysics FEA and is therefore very useful for parametric noise studies at different PWM excitations.

6 REFERENCES

- [1] Boys, J.T., Handley, P.G. (1990). Harmonic analysis of space vector modulated PWM waveforms. *IEEE Proceedings B - Electric Power Applications*, vol. 137, no. 4, p. 197-204, DOI:10.1049/ip-b.1990.0023.
- [2] Tsoumas, I.P., Tischmacher, H. (2014). Influence of the Inverter's modulation technique on the audible noise of electric motors. *IEEE Transactions on Industry Applications*, vol. 50, no. 1, p. 269-278, DOI:10.1109/TIA.2013.2268453.
- [3] Binojumar, A.C., Saritha, B., Narayanan, G. (2015). Acoustic noise characterization of space-vector modulated induction motor drives - an experimental approach. *IEEE Transactions on Industrial Electronics*, vol. 62, no. 6, p. 3362-3371, DOI:10.1109/TIE.2014.2374557.
- [4] Luznar, J., Slavič, J., Boltežar, M. (2018). Experimental research on structure-borne noise at pulse-width-modulation excitation. *Applied Acoustics*, vol. 137, p. 33-39, DOI:10.1016/j.apacoust.2018.03.005.
- [5] Le Besnerais, J., Lanfranchi, V., Hecquet, M., Brochet, P. (2010). Characterization and reduction of audible magnetic noise due to PWM supply in induction machines. *IEEE Transactions on Industrial Electronics*, vol. 57, no. 4, p. 1288-1295, DOI:10.1109/TIE.2009.2029529.
- [6] Islam, R., Husain, I. (2010). Analytical model for predicting noise and vibration in permanent-magnet synchronous motors. *IEEE Transactions on Industry Applications*, vol. 46, no. 6, p. 2346-2354, DOI:10.1109/TIA.2010.2070473.
- [7] Le Besnerais, J., Lanfranchi, V., Hecquet, M., Brochet, P., Friedrich, G. (2010). Prediction of audible magnetic noise radiated by adjustable-speed drive induction machines. *IEEE Transactions on Industry Applications*, vol. 46, no. 4, p. 1367-1373, DOI:10.1109/TIA.2010.2049624.
- [8] Lin, F., Zuo, S., Deng, W., Wu, S. (2016). Modeling and analysis of electromagnetic force, vibration, and noise in permanent-magnet synchronous motor considering current harmonics. *IEEE Transactions on Industrial Electronics*, vol. 63, no. 12, p. 7455-7466, DOI:10.1109/TIE.2016.2593683.
- [9] Pellerey, P., Lanfranchi, V., Friedrich, G. (2012). Coupled numerical simulation between electromagnetic and structural models. Influence of the supply harmonics for synchronous machine vibrations. *IEEE Transactions on Magnetics*, vol. 48, no. 2, p. 983-986, DOI:10.1109/TMAG.2011.2175714.
- [10] Druesne, F., Hallal, J., Lardeur, P., Lanfranchi, V. (2016). Modal stability procedure applied to variability in vibration from electromagnetic origin for an electric motor. *Finite Elements in Analysis and Design*, vol. 122, p. 61-74, DOI:10.1016/j.finel.2016.09.004.
- [11] Zhu, W., Fahimi, B., Pekarek, S. (2006). A field reconstruction method for optimal excitation of permanent magnet synchronous machines. *IEEE Transactions on Energy Conversion*, vol. 21, no. 2, p. 305-313, DOI:10.1109/TEC.2005.859979.
- [12] Sutthiphornsombat, B., Khoobroo, A., Fahimi, B. (2010). Mitigation of acoustic noise and vibration in permanent magnet synchronous machines drive using field reconstruction method. *IEEE Vehicle Power and Propulsion Conference*, p. 1-5, DOI:10.1109/VPPC.2010.5728997.
- [13] Torregrossa, D., Fahimi, B., Peyraut, F., Miraoui, A. (2012). Fast computation of electromagnetic vibrations in electrical machines via field reconstruction method and knowledge of mechanical impulse response. *IEEE Transactions on Industrial Electronics*, vol. 59, no. 2, p. 839-847, DOI:10.1109/TIE.2011.2143375.
- [14] Gu, L., Moallem, M., Bostanci, E., Wang, S., Devendra, P. (2016). Extended field reconstruction method for modeling of interior permanent magnet synchronous machines. *IEEE Transportation Electrification Conference and Expo (ITEC)*, p. 1-6, DOI:10.1109/ITEC.2016.7520252.
- [15] Furlan, M., Černigoj, A., Boltežar, M. (2003). A coupled electromagnetic-mechanical-acoustic model of a DC electric motor. *COMPEL-The International Journal for Computation and Mathematics in Electrical and Electronic Engineering*, vol. 22, no. 4, p. 1155-1165, DOI:10.1108/03321640310483075.
- [16] Torregrossa, D., Paire, D., Peyraut, F., Fahimi, B., Miraoui, A. (2012). Active mitigation of electromagnetic vibration radiated by PMSM in fractional-horsepower drives by optimal choice of the carrier frequency. *IEEE Transactions on Industrial Electronics*, vol. 59, no. 3, p. 1346-1354, DOI:10.1109/TIE.2010.2081961.
- [17] Neugebauer, H. (2012). *Parameter Identification of a Permanent Magnet Synchronous Motor*. MSc thesis, Chalmers University of Technology, Gothenburg.
- [18] Khoobroo, A., Fahimi, B., Pekarek, S.D. (2008). A new field reconstruction method for permanent magnet synchronous machines. *34th Annual Conference of IEEE Industrial Electronics*, p. 2009-2013, DOI:10.1109/IECON.2008.4758265.
- [19] Gu, L. (2016). *Modeling of permanent Magnet Machines Using Field Reconstruction Method*. PhD thesis, The University of Texas, Dallas.
- [20] Maia, N.M.M., Silva, J.M.M. (1997). *Theoretical and experimental Modal Analysis*. Research Studies Press, Taunton.
- [21] Ewins, D.J. (1984). *Modal Testing: Theory and Practice*. John Wiley & Sons, Ontario.

- [22] ISO/TS 7849-1 (2009). *Acoustics: Determination of Airborne Sound Power Levels Emitted by Machinery Using Vibration Measurement*. International Organization for Standardization, Geneva.
- [23] Marburg, S. (2002). Six boundary elements per wavelength: Is that enough?. *Journal of Computational Acoustics*, vol. 10, no. 1, p. 25-51, DOI:10.1142/S0218396X02001401.
- [24] Gieras, J.F., Wang, C., Lai, J.C. (2006). *Noise of Polyphase Electric Motors*. CRC Press, Boca Raton.

Fuzzy Hybrid Method for the Reconstruction of 3D Models Based on CT/MRI Data

Mario Sokac¹ – Djordje Vukelic^{1,*} – Zivana Jakovljevic² – Zeljko Santosi¹ – Miodrag Hadzistevic¹ – Igor Budak¹

¹University of Novi Sad, Faculty of Technical Sciences, Serbia

²University of Belgrade, Faculty of Mechanical Engineering, Serbia

This research proposes a hybrid method for improving the segmentation accuracy of reconstructed 3D models from computed tomography/magnetic resonance imaging (CT/MRI) data. A semi-automatic hybrid method based on combination of Fuzzy C-Means clustering (FCM) and region growing (RG) is proposed. In this approach, FCM is used in the first stage as a preprocessing step in order to classify and improve images by assigning pixels to the clusters for which they have the maximum membership, and manual selection of the membership intensity map with the best contrast separation. Afterwards, automatic seed selection is performed for RG, for which a new parameter standard deviation (STD) of pixel intensities, is included. It is based on the selection of an initial seed inside a region with maximum value of STD. To evaluate the performance of the proposed method, it was compared to several other segmentation methods. Experimental results show that the proposed method overall provides better results compared to other methods in terms of accuracy. The average sensitivity and accuracy rates for cone-beam computed tomography CBCT 1 and CBCT 2 datasets are 99 %, 98.4 %, 47.2 % and 89.9 %, respectively. For MRI 1 and MRI 2 datasets, the average sensitivity and accuracy values are 99.1 %, 100 %, 75.6 % and 99.6 %, respectively. The average values for the Dice coefficient and Jaccard index for the CBCT 1 and CBCT 2 datasets are 95.88, 0.88, 0.6, and 0.51, respectively, while for MRI 1 and MRI 2 datasets, average values are 0.96, 0.93, 0.81 and 0.7, respectively, which confirms the high accuracy of the proposed method.

Keywords: fuzzy C-means clustering, region growing, image segmentation, surface 3D model

Highlights

- A hybrid method is proposed for accurate segmentation of CT/MRI data.
- A new seed selection approach for the region growing method is developed.
- Experimental results show good accuracy and robustness.
- The segmentation accuracy has increased, which was confirmed with various performance measures.

0 INTRODUCTION

Image analysis plays a vital role in modern computer-aided systems. Images can be obtained from different modalities, such as cone beam computed tomography (CBCT), magnetic resonance imaging (MRI), positron emission tomography (PET), single-photon emission computed tomography (SPECT), ultrasound, etc. These can provide three-dimensional (3D) image datasets that contain accurate information for the generation of surface 3D models, even when compared to optical 3D digitizing methods [1]. Surface 3D models are a very useful resource for accurate diagnosis, but also for further action such as preparation of surgeries, designing different types of implants, etc. The most critical step for the generation of a surface 3D model is the accurate segmentation for extracting objects of interest from the surroundings, thus enabling 3D surface reconstruction [2] and [3].

Information acquired from medical images has a significant impact on proper diagnosis and treatment. For this purpose, the segmentation of medical images is performed, which can be either manual or automatic [4]. Nowadays, due to the large amount of data obtained

using medical imaging systems, methods used for semi-automatic or fully automatic segmentation are more favourable but still refer to manual results for verification and training purposes [5]. When a 2D image is acquired, some information may be lost, and this information loss degrades the image quality, and more importantly affects the accuracy of segmentation and geometry reconstruction, eventually endangering proper diagnosis. Therefore, accurate reconstruction of geometry is required and depends on several factors, including spatial resolution, which is determined by the layer thickness [6], and slice thickness, which affects loss of resolution quality on the reconstructed data [7]. Without some form of image enhancement, segmentation of medical images becomes very difficult and sometimes does not provide accurate results. This occurs as a result of the vague structures in poorly displayed medical images, or with the presence of homogenous surrounding structures. Thus, to improve the segmentation accuracy, it is necessary to preprocess image and to enhance its quality. With the breakthrough of additive manufacturing (AM) technologies in the medical field, it enabled physical fabrication of anatomical structures, which strongly

depends on the input data. The development of medical imaging and especially imaging software has made it possible to create various kinds of 3D models from medical images [8]. The entire process can, into three steps, which are data acquisition, image processing, and model manufacturing [9]. This integration propelled the barriers and possibilities for applications of medical implants used for different types of trauma, disease, bone damage and defects which need to be reconstructed [10]. Therefore, adequate image segmentation and reconstruction of 3D models is vital for their applications in this field.

There are several methods used for image enhancement, and one of the most commonly used for contrast enhancement of medical images is histogram equalization [11]. Besides this, other improved methods for histogram equalization such as Type II fuzzy set theory [12] or bi-histogram equalization with a plateau level [13] are presented, thus improving quality and reducing the time required for image enhancement. However, with the further development of computer technologies, intelligent systems employing genetic algorithms, fuzzy logic, machine learning, neural networks, and swarm intelligence are finding their place and are applied in different scenarios and in different fields [14] to [17]. Many researchers have combined different methods to maximize their advantages and to solve current drawbacks regarding segmentation of CT images, even going as far as implementing 4D architecture for motion estimation [18], thus improving performance. A combination of different methods can improve data extraction from CT images, as seen in [19] by implementing a deep learning model or by combining spatial fuzzy clustering and level-set methods [20]. For the segmentation of MRI images, the authors in [21] proposed a new method for joint bias field estimation and segmentation of MRI images.

Regarding common drawbacks of thresholding methods where images are corrupted with artefacts and noise, the authors in [22] proposed a new multi-region thresholding methodology by using fuzzy sets. Concerning the various implementations of the fuzzy C-means clustering (FCM) method, many researchers have combined this method with other methods such as region-based active contour [23], the level set method [24], self-organizing maps [25], region growing and particle swarm optimization method [26]. The main goal of their implementation was to improve segmentation accuracy in each of these fields.

In contrast to previous investigations, the present paper proposes a hybrid method that combines fuzzy C-means clustering and automated region growing

methods to enhance and segment medical 3D image datasets with higher accuracy. The novelty in this paper is in the newly developed method for automatic initial seed selection for region growing, which incorporates the value of standard deviation (STD) as a measure for seed selection. This, in combination with image enhancement based on FCM, completes the entire process for the segmentation of 3D image datasets. The presented method focuses on the enhancement of poorly visible structures present on CBCT and MRI datasets, which will improve segmentation and surface extraction. Two CBCT 3D image datasets and two MRI 3D image datasets were used for testing purposes and analysis of the proposed method.

1 METHODS

The approach is based on incorporating two methods that are used in image processing: FCM and the region-growing (RG) method. Their integration leads to the segmentation that consists of two stages. In the first stage, FCM is used as a tool for the enhancement of input 3D image datasets by making the borders of the vague areas more pronounced. This stage is especially crucial for corrupted CBCT images in which the vague areas are common. In the second stage, we introduce the automatic RG method based on a new principle of finding initial seed using calculated STD of pixel intensity inside regions that are present on images. The flowchart is illustrated in Fig. 1.

Besides the previously mentioned two stages, the flowchart contains an optional step that refers to the definition of region of interest (ROI). Namely, to accelerate the segmentation process, in some cases it is convenient to localize the area of interest for image segmentation on large 3D image datasets. For these purposes, a user can opt to utilize a specially designed tool for manually defining ROI and for localizing the area on image for segmentation.

1.1 Image Enhancement Based on Fuzzy Clustering

Fuzzy C-means is one of the most popular fuzzy clustering techniques because it is easy to implement, as well as being efficient and straightforward. FCM clustering generates fuzzy partitions for any set of numerical data, allowing one piece of data to belong to two or more clusters simultaneously [27].

FCM is used as a tool for image enhancement. To achieve computational efficiency, and to reduce time required for segmentation of large 3D image datasets,

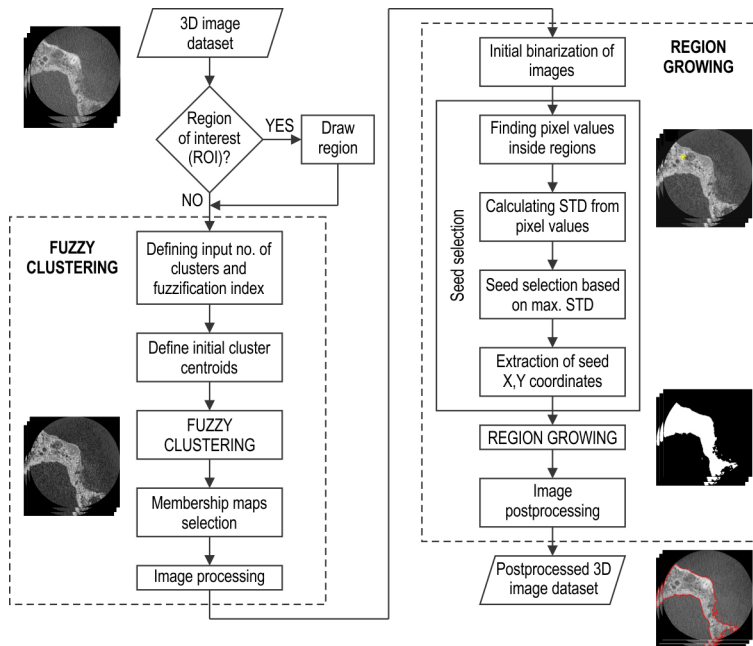


Fig. 1 Flowchart of the proposed methodology

we use the histogram of pixel intensities during the clustering process instead of the raw image data.

The working principle of the proposed FCM method for image enhancement consists of the following steps:

Step 1: Read the input set of images named im and define input parameters: c (no. of clusters) and q (fuzzification index).

Step 2: Calculate the maximum (I_{max}) and minimum intensity (I_{min}) of each image in image set im and arrange the overall intensity in ascending order as shown in Eq. (1):

$$I = (I_{min} \rightarrow I_{max}). \quad (1)$$

Step 3: Find the size of I and assign it to a variable named si . Calculate the histogram (H) of the image set im .

Step 4: Generate the initial cluster segmentation size or class gap (dl) using Eq. (2):

$$dl = \frac{(I_{max} - I_{min})}{c}. \quad (2)$$

Step 5: Generate the initial cluster's centroids $C(i)$ using Eq. (3). These centroids are equidistantly distributed along intensities present in the image:

$$C(i) = I_{min} + \frac{dl}{2} + \sum_{j=1}^i dl, \quad (3)$$

where Eq. (3) provides centroid points with: Start>>>>Class_gap>>>>End.

Step 6: Set the initial error $dC = \text{infinity}$.

Step 7: Repeat the Steps (8) to Step (14) until $dC < 0.000001$.

Step 8: Set initial centroid matrix $C0=[C(i)]$.

Step 9: Calculate the distance D between each centroid and each pixel's intensity of image using Eqs. (4) and (5):

$$D(j, i) = |I(j) - C(i)|, \quad (4)$$

$$D(j, i) = D(j, i)^{2/(q-1)}, \quad (5)$$

here $i = 1, 2, \dots, c$, and $j = 1, 2, \dots, si$.

Step 10: Calculate the fuzzy membership of each pixel's intensity to each cluster using Eq. (6):

$$U(j, i) = \frac{1}{D(j, i) \sum_{i=1}^c \frac{1}{D(j, i)}}. \quad (6)$$

Step 11: Calculate the membership-histogram matrix UH using Eq. (7):

$$UH(j, i) = U(j, i)^q \cdot H(j). \quad (7)$$

Step 12: Calculate new centroid location C of each cluster using Eq. (8):

$$C(i) = \frac{\sum_{j=1}^{si} UH(j, i) \cdot I(j)}{\sum_{j=1}^{si} UH(j, i)}, \quad (8)$$

here $i = 1, 2, \dots, c$.

Step 13: Calculate the maximum difference error (dC) between new and old clusters using Eq. (9).

$$dC = \max(|C_0 - C|), \quad (9)$$

here $i = 1, 2, \dots, c$.

Step 14: Go to Step (7).

Several stopping rules can be used. One is to terminate the algorithm when the relative change in the centroid values becomes small, or when the objective function can no longer be minimized. After that, defuzzification is performed by assigning the pixels to the clusters, for which those pixels have the maximum membership. A membership intensity map for each cluster is generated, and the most suitable cluster is selected for the next stage of the process: RG method implementation. The selection is carried out manually by a user who has to consider that the selected class membership should have the best contrast separation between the borders of the object and the background on the image. This will contribute to better segmentation using the RG method later.

Fig. 2 shows an example of the result of image enhancement. The input parameters for this example were number of clusters $c = 3$ and fuzzification index $q = 6$. From this example, cluster no. 3 was selected, as it represents the best contrast separation between the borders of the object and the background on the image (decision of operator based on visual impression).

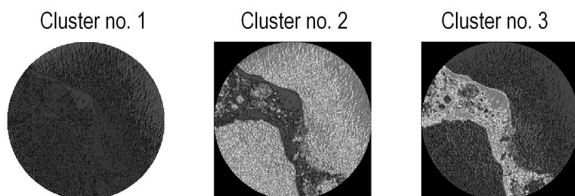


Fig. 2. Manual selection of membership intensity map for three clusters ($c = 3$); in this case the best contrast separation is shown in cluster no. 3

After images have been enhanced using FCM, their pixels' intensities vary between 0 and 1, and need to be normalized in the range [0, 255]. The median filtering was also performed on the enhanced images using the default 3-by-3 neighbourhood, i.e., each output pixel obtains the median value of its 3-by-3 neighbourhood. This nonlinear filtering technique was used to reduce any noise present on images; it is a widely used technique that is very effective in removing noise while preserving edges [28].

To verify the performances of the proposed enhancement of images using the FCM method, we have selected pixels along a 2D profile line that is arbitrarily drawn at the same location over an image before (Fig. 3a) and after enhancement (Fig. 3b). Intensities of pixels along these lines are compared to determine the differences between two images. The comparison from Fig. 3c shows that the enhancement procedure leads to the: 1) normalization of pixel intensities, 2) higher values of pixel intensities in the transition between low and high-intensity areas. The latter is a critical property since it will contribute to easier and better segmentation using the RG method that will follow.

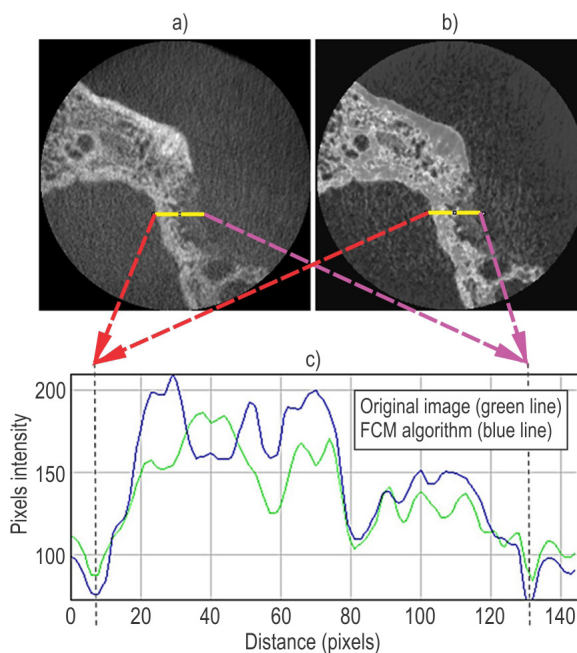


Fig. 3. 2D profile line measurement on a) original image, b) enhanced image, c) graph showing the intensity of pixels on original image (green line) and after the improvement using FCM (blue line)

1.2 Region Growing

Region growing (RG) is a method that has been widely used for image segmentation [29]. RG is a segmentation method where each region starts as a single seed element. At each iteration, the surrounding pixels are taken into account in order to determine whether the region should be expanded to include them or not, and this is controlled by a tolerance parameter t [29]. Various metrics can be used as a basis for region growing, and we have opted to employ pixel's intensity. The value of tolerance parameter t depends on the total range of pixels' intensity on an

image, it varies with each input image or 3D image dataset, and it is left for the user to define. However, the selection of initial seed for the segmentation also has a deep influence on the end results. How to assign initial seeds represents a major issue when it comes to application of the RG method [30]. To improve the accuracy of the RG method, we propose a method for seed selection that is based on the STD of pixels' intensities in the regions. Specifically, the seed is selected from the region with the highest standard deviation of pixels' intensities.

1.2.1 Initial Segmentation and Standard Deviation of Pixels' Intensities

Seed selection procedure starts from initial, coarse, segmentation of the enhanced image. Initially segmented regions in the enhanced image are acquired via global image thresholding, which was performed using Otsu's method [31] in which a global threshold T was computed from image and in which Otsu's method chooses a threshold that minimizes the intraclass variance of the thresholded black and

white pixels. As a result, an initially binarized image is obtained which contains segmented regions. These regions are then applied as a mask to the enhanced image, and the STD of pixels' intensities is calculated for each of them. In the subsequent steps, the seed will be selected from the region with the highest value of STD. This procedure is repetitive, and the initial seed is defined for each image separately.

The rationale behind this kind of selection of region where the seed will be placed is as follows. A large scattering of pixel intensities is typically encountered in the objects that need to be extracted from image, while the scattering of pixel intensities in surrounding tissue (which is, as a rule, homogeneous) is smaller. Since all pixels inside a region have different intensity values, the larger the deviations in pixel intensities are, the STD value will be larger.

For a random variable vector \mathbf{A} (in this case pixel intensity vector) made up of N scalar observations, the standard deviation is defined according to Eq. (10):

$$\sigma = \sqrt{\frac{1}{N-1} \sum_{i=1}^N (A_i - \mu)^2}, \quad (10)$$

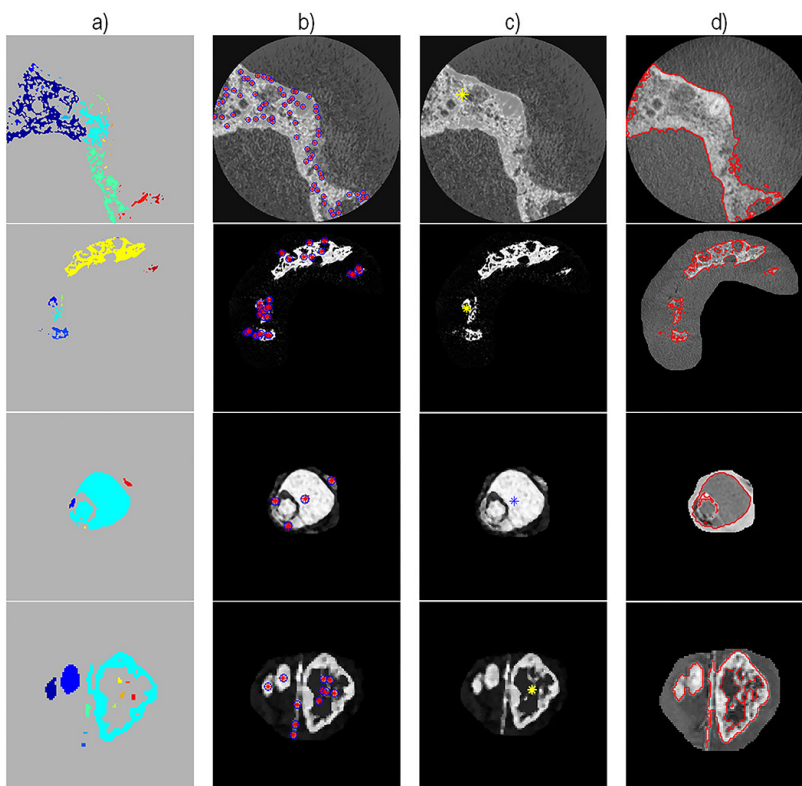


Fig. 4 The principle of proposed RG method for image no. 13 from CBCT 1, CBCT 2, MRI 1 and MRI 2 3D image dataset showing a) initial segmentation, b) location of all regions on an image, c) selected region with its initial seed for RG method, d) segmented image using proposed RG method outlined in red line

where μ is the average value of vector \mathbf{A} , as shown in Eq. (11):

$$\mu = \frac{1}{N} \sum_{i=1}^N A_i. \quad (11)$$

The proposed approach for coarse placement of seed has positive effect on the subsequent selection of initial seed and reduces the possibility for its mis-selection. Specifically, using the proposed procedure, the size of region does not affect the result. In addition, it is worth noting that regions within images that have been enhanced using FCM will have a larger value of STD due to scaled pixels' intensities inside them; this will be helpful for better selection of initial seed because values of STD inside those regions will be more distinct. Following the definition of the initial seed for each image, the tolerance parameter t which will enable segmentation using RG method must be defined.

The results of the application of the proposed procedure for region selection and initial seed extraction are presented using relevant examples in Fig. 4. The plots of STD of pixel intensities in initially segmented regions, using image no. 13 as an example from all four image datasets, are presented in Fig. 5.

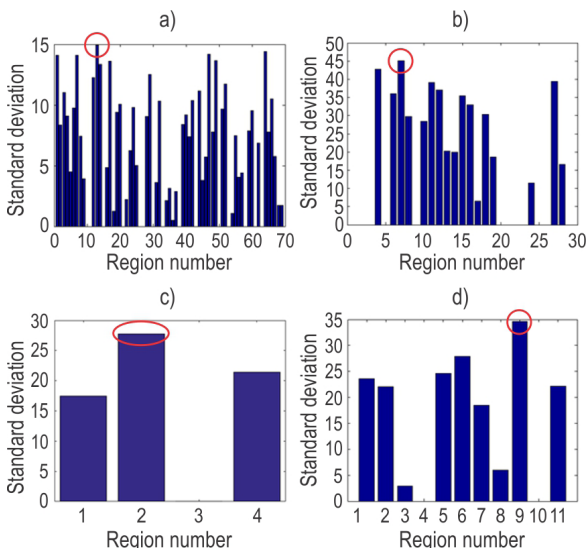


Fig. 5. STD plot of regions in image no. 13 from all image datasets (region with highest value of STD is marked red): a) CBCT 1 dataset (region no. 13), b) CBCT 2 dataset (region no. 7), c) MRI 1 dataset (region no.2), d) MRI 2 dataset (region no. 9)

Since the FCM method enhances the boundaries of objects very well, the automated RG method can successfully segment the objects of interest from the enhanced images in order to obtain more accurate binary 2D images needed for 3D reconstruction. The

results of the real-world image segmentation carried out by RG based on pixel intensities are presented in Fig. 4d. As a final step after the images have been segmented, some minor postprocessing is required in order to remove the small pixels surrounding the segmented object of interest with the use of morphological operations (dilation and erosion).

1.2.2 Seed Selection

When the region with the highest STD has been determined, it would be convenient to select its centre as the initial seed for the RG method. However, since regions can vary from simple shape to a very complex and irregular shape, the centre can be placed outside the region. To assure that the initial seed remains inside the region with the highest STD, we have developed a new method.

In this method, the basic principle is the skeletonization or thinning [32] of the region with the highest STD. As a result, the thinned skeleton (or lines) of the region is generated; it consists of many consecutive points with their (X,Y) coordinates. By extracting the middle pair of coordinates, the coordinates for the initial seed are determined. In this way, it is guaranteed that the selected seed remains inside the defined region with the maximum STD, which allows a proper segmentation using the RG method.

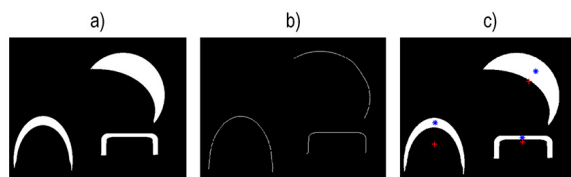


Fig. 6. Proposed method on seed selection showing a) original image, b) skeletonization of regions using the proposed approach for seed selection, c) locations of seeds of all regions present on image shown in red (centre of mass-based) and blue (proposed approach)

Fig. 6 shows the effect of the proposed method on seed selection using the proposed approach. The image shown in Fig. 6a is an artificially made image, and the results of skeletonization (or thinning) process of regions present in this image are given in Fig. 6b. Fig. 6c shows the initial seed selected using the proposed approach (marked with blue), versus the seed selected using method (marked with red) which calculates the seed position based on the centre of mass of the region.

From Fig. 6c it can be seen that the red shows incorrectly defined seeds that are outside of the regions. In some specific applications, centre of mass-based seed selection presents an acceptable solution but regarding more complex and irregular shapes, it will not provide acceptable results. When the proposed skeletonization based approach is employed, the complexity of shapes does not represent an issue (shown in blue), which additionally contributes to the overall accuracy and stability of the presented approach.

2 EXPERIMENTAL

Performance evaluation of the proposed method was carried on two CBCT 3D image datasets and two MRI 3D image datasets. Datasets used in this study were acquired anonymously, where all patient information was erased. The CBCT datasets are collected from the Department of Dentistry, Medical Faculty, University of Novi Sad, using a SCANORA™ 3D medical imaging device from Soredex, while MRI datasets were collected from the Department of Radiology, Medical Faculty, University of Novi Sad, using a Discovery™ MR750 medical imaging system from GE Healthcare. Acquisition parameters are shown in Table 1.

Table 1. Acquisition parameters used for the presented case studies on CBCT and MRI imaging scanners

	SCANORA™ 3D CBCT scanner	Discovery™ MR750 MRI scanner
X-ray energy [kV]	89	/
Current [mA]	8	/
Voxel size [mm]	0.133	1.2
Image resolution [pixel]	300×300	512×512
No. of images/slices	451	128
Field-of-view [mm]	/	553×240

CBCT and MRI imaging systems were selected for this study due to their availability at the radiology department at the local clinical centre. While MRI datasets have perhaps more trivial and relatively distinct boundaries, two CBCT image datasets have more generally weak and indistinct boundaries due to the porosity of the maxilla bone.

After sifting through all the images related to each patient, only corrupted images on CBCT 3D image datasets and images containing tumour on MRI 3D image datasets were used for experimental analysis. A radiologist with over ten years of experience and who is responsible for interpreting medical records at the local clinical centre performed manual segmentation

of all medical images using commercial medical image processing software 3D-DOCTOR v4.0 from Able Software Corp. Results of this manual segmentation provided binary segmented images that will be used as a foundation for evaluation. The proposed method was implemented in the R2018b version of MATLAB (Mathworks, Inc., Natick, MA, USA) on a PC (FUJITSU CELSIUS M470-2) with Intel(R) Xeon(R) CPU E5645, 2.40 GHz processor, and 16 GB RAM. The operating system used was Windows 7 (64-bit).

The segmented images obtained using the proposed method and other segmentation methods; fuzzy clustering method with level set method (FCMLSM) from [20], multi-region fuzzy thresholding method (MFT) from [22] and multiplicative intrinsic component optimization (MICO) from [21] were all individually compared against their corresponding manually segmented images obtained from the radiologist, in order to test the segmentation accuracy. As a result, performance measures, such as Dice coefficient, Jaccard index, sensitivity, and accuracy, are calculated. The proposed method and other methods were tested on all four 3D image datasets.

Fig. 7 shows the results of compared segmentation techniques, i.e. the final contours of the bone from CBCT 1 (Fig. 7a), CBCT 2 (Fig. 7b), MRI 1 (Fig. 7c) and MRI 2 (Fig. 7d) 3D image dataset on one image from each 3D image dataset. Two CBCT 3D image datasets were especially important for segmentation since the CBCT systems are prone to noise [33] and [34] and successful analysis of CBCT acquired images is of great importance. The two CBCT datasets contain the images of the upper maxilla, frequently used in the field of oral surgery and for other applications in dentistry, such as designing and fabrication of patient-specific bone grafts [35] where accurate segmentation and extraction of initial 3D models is extremely important. These two 3D image datasets were also important for the analysis since the bone structure of the maxilla is porous and is difficult to properly acquire its bone structure by CBCT systems.

Fig. 7 shows the results of compared segmentation techniques, i.e. the final contours of a tumour on brain MRI images. MRI 1 and MRI 2 3D image datasets were used and, for this purpose, an ROI tool was used to localize the tumour. All four segmentation methods, including the proposed method, were used to segment the two image datasets.

2.1 Performance Analysis of Seed Selection of RG Method

To test the accuracy of initial seed selection using our modified RG method, it was tested on all four 3D

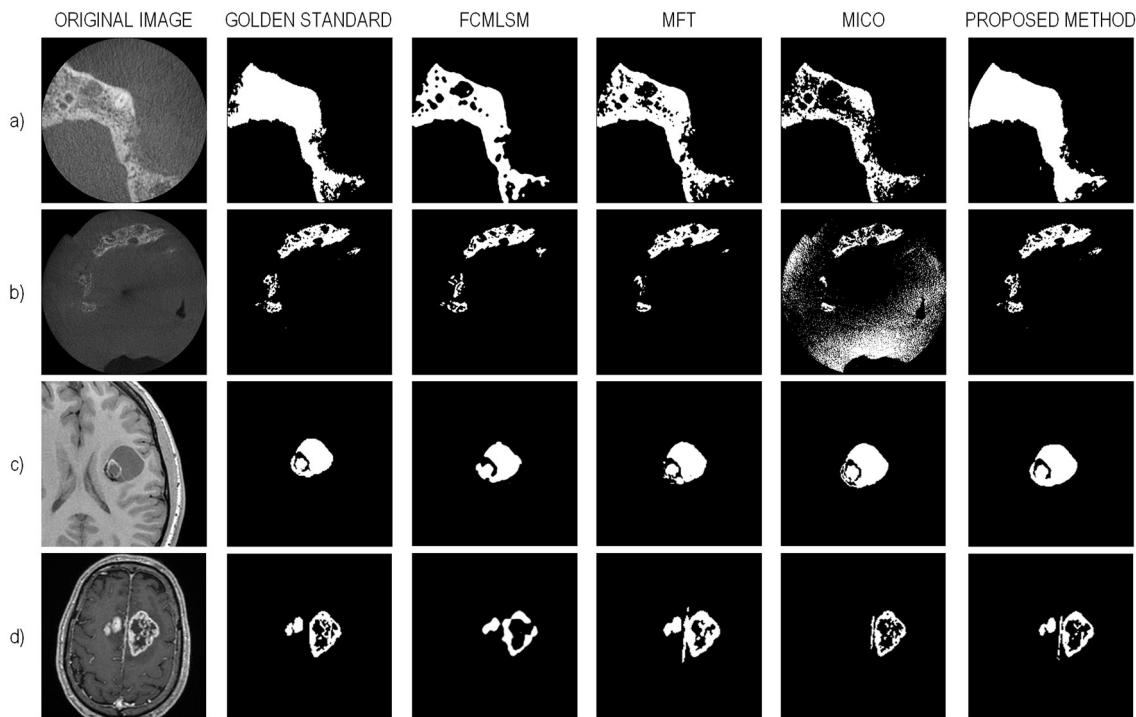


Fig. 7 Results of compared segmentation techniques for image no. 13 from a) CBCT 1, b) CBCT 2, c) MRI 1 and d) MRI 2 3D image dataset for FCMLSM [20], MFT [22], MICO [21], and proposed method (for CBCT 1: $C=3, q=6, t=25$, for CBCT 2: $C=3, q=2, t=40$, for MRI 1: $C=3, q=2, t=95$ and for MRI 2: $C=3, q=3, t=25$)

image datasets. A performance analysis of the seed selection method using CBCT and MRI 3D image datasets is presented in Table 2.

Table 2. Performance analysis for seed selection on all four 3D image datasets

Dataset	Total no. of images	Used images	Initial seed correctly detected	Accuracy [%]
CBCT 1	303	16	16	100
CBCT 2	57	57	52	91.22
MRI 1	49	30	29	96.67
MRI 2	47	47	40	85.11

In the CBCT 1 dataset, all initial seeds were accurately detected inside a bone structure for all images, while in the CBCT 2 dataset the initial seed for RG method was not properly defined for the first five images. For MRI 1 dataset the initial seed was not selected properly only for the first image. This was also the case for MRI 2 dataset where on the first seven images the beginning of the tumour and the region is too small compared to the surrounding tissue for method to accurately define the initial seed. However, this did not further influence the 3D reconstruction process, and it will be dealt with in future research to overcome this issue.

2.2 Classification Performance

The performance of the proposed method and other segmentation methods was evaluated using two metrics: sensitivity and accuracy.

The sensitivity (S) is defined as the percentage of pixels correctly classified with respect to the number of pixels in the foundation for evaluation. The accuracy (A) is defined as the ratio of the correctly classified pixels and incorrectly classified pixels to the total number of pixels, as shown in Eqs. (12) and (13):

$$S = \frac{TP}{TP + FN}, \tag{12}$$

$$A = \frac{TP + TN}{TP + FN + TN + FP}, \tag{13}$$

where TP (true positive) represents the number of pixels that were correctly detected and TN (true negative) represents the number of background pixels. FN (false negative) denotes the pixels belonging to the segmented region, but wrongly classified as the background pixels, and FP (false positive) is the number of pixels incorrectly classified as the segmented region.

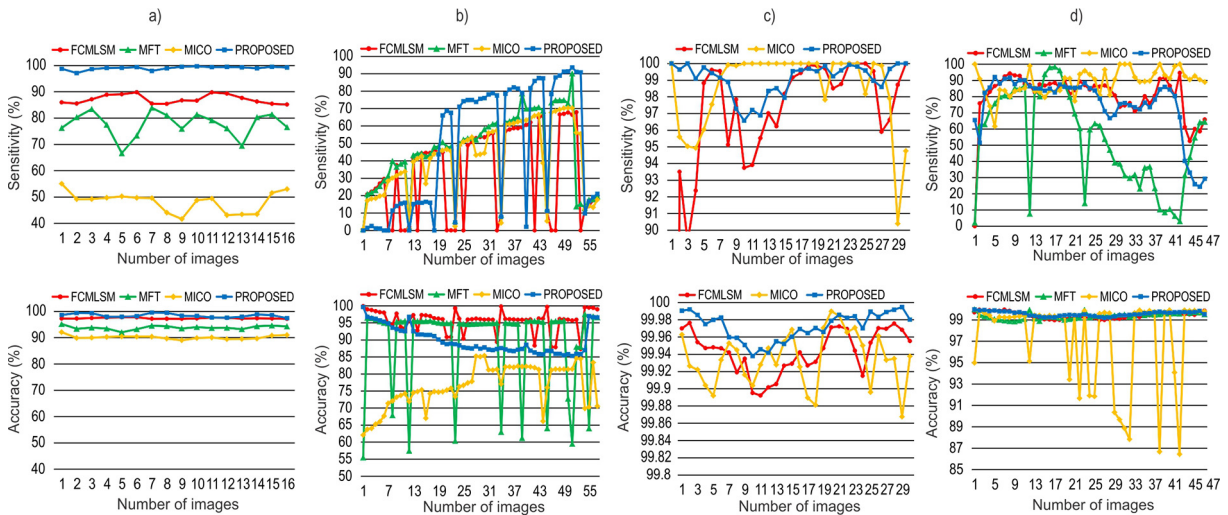


Fig. 8. Results of sensitivity and accuracy comparison between FCMLSM [20], MFT [22], MICO [21] and proposed method for a) CBCT 1, b) CBCT 2, c) MRI 1, d) MRI 2 3D image dataset

Fig. 8 presents the results of the comparative analysis of the proposed method, FCMLSM [20], MFT [22] and MICO [21] when compared to images from the foundation for evaluation. They were tested for sensitivity and accuracy performance. These two metrics were evaluated for all four 3D image datasets.

For the CBCT 1 image dataset (Fig. 8a), it can be noted that the proposed method outperforms all other methods in terms of sensitivity and accuracy. In the CBCT 2 image dataset (Fig. 8b), it can also be observed that the proposed method excels when compared with other methods for sensitivity. For accuracy performance, the FCMLSM method [20] performs better.

For analysis of the MRI 1 image dataset (Fig. 8c), the MFT [22] method was not taken into account due to its having the lowest performance results when compared to the other methods. The proposed method outperforms the FCMLSM [20] and MICO [21] segmentation methods for the MRI 1 image dataset, both for sensitivity and accuracy.

In the MRI 2 image dataset (Fig. 8d), it can be seen that FCMLSM [20] outperforms the proposed method in terms of sensitivity, while with regard to accuracy, the proposed method shows better results than other segmentation methods.

Table 3 summarizes the evaluation results of the proposed method and other segmentation methods. It can be observed that, overall, the proposed method shows better results regarding the accuracy performance in comparison to other methods, except for the CBCT 2 image dataset for which the FCMLSM method [20] excels with results of 95.69. Regarding

the sensitivity, the proposed method also shows good results, except for the MRI 2 image dataset for which the MICO method [21] obtained higher results of 88.93.

Table 3. The average value of the classification performance metrics using the FCMLSM [20], MFT [22], MICO [21] and the proposed method

Image set	FCMLSM [%]		MFT [%]		MICO [%]		Proposed method [%]	
	S	A	S	A	S	A	S	A
CBCT 1	87.1	97.4	93.8	77.7	48.2	90.1	99	98.4
CBCT 2	32.6	95.7	45.5	89.3	41.8	76.4	47.2	89.9
MRI 1	94.2	99.9	51.2	99.8	98.6	99.9	99.1	100
MRI 2	80.1	99.4	53.4	99.4	88.9	97.2	75.6	99.6

2.3 Segmentation Performance

To determine the segmentation accuracy and to measure the segmentation performance of the proposed method and three other methods against the foundational images, Dice coefficient and Jaccard index were used.

The mean values of Dice coefficient and Jaccard index for all four datasets and tested methods are listed in Table 4. The mean values of Dice and Jaccard for the CBCT 1 and CBCT 2 3D image dataset for the proposed method are 0.95, 0.88, and 0.60, 0.51, respectively, while for the MRI 1 and MRI 2 3D image dataset those values are 0.96, 0.93 and 0.81, 0.70, respectively. It can be seen from Table 4 that the proposed method significantly improves both

bone and soft tissue detection (brain tumour), based on all similarity indices, and it outperforms all other segmentation methods for all four image datasets. This indicates that the proposed method extracts the defined regions from both CBCT and MRI image datasets with higher accuracy.

Table 4. The average value of the segmentation performance metrics (Dice coefficient and Jaccard index) using the FCMLSM [20], MFT [22], MICO [21] and the proposed method

Image set	FCMLSM		MFT		MICO		Proposed method	
	DC	Ji	DC	Ji	DC	Ji	DC	Ji
CBCT 1	0.91	0.85	0.84	0.73	0.62	0.45	0.95	0.88
CBCT 2	0.58	0.48	0.59	0.46	0.30	0.19	0.60	0.51
MRI 1	0.90	0.85	0.77	0.69	0.91	0.85	0.96	0.93
MRI 2	0.77	0.65	0.80	0.69	0.80	0.69	0.81	0.70

2.4 CAD-Inspection

CAD-Inspection has shown to be a valuable tool in current applications with regard to the dimensional inspection of 3D models. Since the proposed method can segment the 3D image dataset, MATLAB was used for the reconstruction of 3D models of a tumour located in the MRI 1 and MRI 2 3D image datasets. Reconstructed 3D models were then exported in STL file format (Fig. 9a). A 3D model from ground truth images was generated using software 3D-DOCTOR. For CAD-Inspection, GOM Inspect v2016 software was used (Fig. 9b); the results of the inspection are presented in Table 5.

From the results presented in Fig. 9 and Table 5, it can be observed that the deviations for 3D model generated from the MRI 1 image dataset are distributed in the range from -0.15 mm up to +0.52 mm, and the majority of deviations are located around +0.05 mm. Small values of standard deviation of +0.23 and mean distance of +0.16 show good accuracy of the overlapped 3D model with the foundational 3D model with the distance of ±0.99 mm. For the MRI 2 image dataset, deviations are in the range from -0.75 mm to +0.45 mm, with the majority of deviations located at the -0.15 mm mark. Standard deviation and mean value have smaller values, and they are +0.44 mm and -0.22 mm, respectively. The minimum and maximum distance are in the range of ±1.30 mm. The dimensional analysis also showed some minor irregularities, which can be seen in certain areas on both inspections of the 3D models. This could be the result of surface shape, but also of the algorithm used for 3D reconstruction.

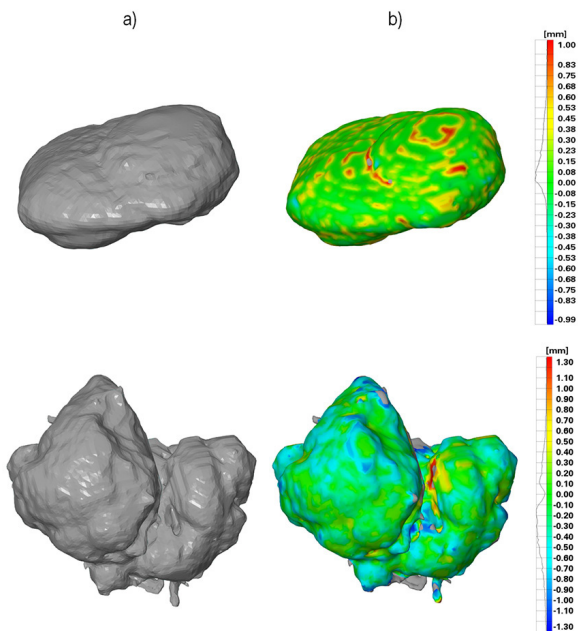


Fig. 9. a) 3D model generated from MRI 1 and MRI 2 3D image datasets using the proposed method in MATLAB software, and b) CAD inspection of 3D models generated using proposed method compared to the ground truth 3D models in software GOM Inspect v2016

Table 5. Results from CAD Inspection using the proposed method

3D image dataset	Deviation range [mm]	Min. dist. [mm]	Max. dist. [mm]	Distance STD [mm]	Mean distance [mm]
MRI 1	-0.15 +0.52	-0.99	+0.99	+0.23	+0.16
MRI 2	-0.75 +0.45	-1.30	+1.30	+0.44	-0.22

To test the influence of triangles count within reconstructed 3D models, sensitivity analysis was performed in which the triangles count were increased and decreased on the foundational 3D model that was used as a reference 3D model. The purpose of this analysis was to investigate the influence it might have on the accuracy of CAD-Inspection results. In this case, distance STD and mean distance were evaluated as two main parameters. Table 6 shows the sensitivity analysis of triangles count on CAD-Inspection results for the MRI 1 and MRI 2 datasets. By increasing and decreasing the triangles count as much as ±20 %, the change in mean distance and distance STD values remained very similar for the MRI 1 and MRI 2 datasets. For the MRI 1 and MRI 2 datasets, the mean distance equals 0.01 mm. Based on these observations, it can be concluded that the influence of

triangles count does not have a major impact on the accuracy results from CAD-Inspection.

Table 6. Sensitivity analysis of triangles count on CAD-Inspection results for MRI 1 and MRI 2 datasets

	Percentage [%]	-20	-10	0	+10	+20
	Triangles	23158	26053	28948	31842	34737
MRI 1	Distance STD [mm]	0.23	0.23	0.23	0.23	0.23
	Mean distance [mm]	0.17	0.17	0.16	0.17	0.17
	Percentage [%]	-20	-10	0	+10	+20
	Triangles	50416	56718	63020	69328	75624
MRI 2	Distance STD [mm]	0.47	0.46	0.44	0.48	0.47
	Mean distance [mm]	-0.23	-0.22	-0.22	-0.22	-0.22

3 DISCUSSION

Accurate segmentation is crucial for proper reconstruction of surface 3D models, due to the fact that it enables proper extraction of objects of interest. The results obtained in this paper confirm that the proposed method based on a combination of fuzzy C-means clustering and region growing shows good results when compared with other segmentation methods for segmentation accuracy and sensitivity. The new RG method for seed selection based on STD values shows good accuracy and robustness when tested on all four 3D image datasets. However, future improvements can be made to deal with the issue of the mis-selection of seed for the first few images of 3D image dataset (lowest percentage accuracy was 85.11 for MRI 2 image dataset).

Regarding the statistical evaluators, Dice coefficient and Jaccard index, the proposed method shows very good results, outperforming all other segmentation methods in [20] to [22] for all four 3D image datasets. When the 3D image datasets are evaluated for segmentation accuracy and sensitivity, it can be seen that the proposed method excels other methods on three 3D image datasets (CBCT 1, CBCT 2 and MRI 1) regarding both accuracy and sensitivity, but shows lower results for sensitivity in the MRI 2 image dataset with 75.6, compared with the method in [21] with an obtained value of 88.9. The reason for better performance of the proposed method for CBCT datasets definitely lies in the blurriness of the images and due to the presence of the artefacts on the

3D dataset. Accurate delineation of objects borders is superior for those datasets.

As a final step for the evaluation of 3D models obtained by the proposed method, CAD inspection was performed by using the MRI 1 and MRI 2 image datasets. This inspection confirms the high accuracy of the proposed method in comparison to the 3D model obtained from ground truth images.

4 CONCLUSIONS

FCM clustering enabled the adaptive enhancement of objects of interest in images, and therefore served as an effective preprocessing for RG segmentation. Future work will focus on further improvements. For example, an automated method will be implemented in terms of automatically determining the number of clusters in FCM clustering, such as that proposed in [36] to [38]. In this way, the goal is to eliminate operator assistance during the processing stage. Also, the proposed method will be put into a friendlier graphical user interface which will enable more interactive use. Although images obtained from only CBCT and MRI scanners were used for this study, it does not limit the use of the proposed method on images obtained from other imaging systems as well, and future research will also include this investigation.

5 ACKNOWLEDGEMENTS

This paper presents the results achieved in the framework of the project 114-451-2723/2016-03 funded by the Provincial Secretariat for Higher Education and Scientific Research, and within the project TR-35020, funded by the Ministry of Education, Science and Technological Development of the Republic of Serbia.

6 REFERENCES

- [1] Galeta, T., Pakši, I., Šišić, D., Knežević, M. (2017). Comparison of 3D scanned kidney stone model versus computer-generated models from medical images. *Advances in Production Engineering & Management*, vol. 12, no. 3, p. 254-264, DOI:10.14743/apem2017.3.256.
- [2] Budzik, G., Burek, J., Bazan, A., Turek, P. (2016). Analysis of the accuracy of reconstructed two teeth models manufactured using the 3DP and FDM technologies. *Strojniški vestnik - Journal of Mechanical Engineering*, vol. 62, no. 1, p. 11-20, DOI:10.5545/sv-jme.2015.2699.
- [3] Ameen, W., Al-Ahmari, A., Mohammed, M.K., Abdulhameed, O., Umer, U., Moiduddin, K., (2018). Design, finite element analysis (FEA), and fabrication of custom titanium alloy cranial implant using electron beam melting additive manufacturing.

- Advances in Production Engineering & Management*, vol. 13, no. 3, p. 267-278, DOI:10.14743/apem2018.3.289.
- [4] Van Eijnatten, M., Koivisto, J., Karhu, K., Forouzanfar, T., Wolff, J. (2017). The impact of manual threshold selection in medical additive manufacturing. *International Journal of Computer Assisted Radiology and Surgery*, vol. 12, no. 4, p. 607-615, DOI:10.1007/s11548-016-1490-4.
- [5] Zhang, J., Malcolm, D., Hislop-Jambrich, J., Thomas, C.D.L., Nielsen, P.M.F. (2014). An anatomical region-based statistical shape model of the human femur. *Computer Methods in Biomechanics and Biomedical Engineering: Imaging & Visualization*, vol. 2, no. 3, p. 176-185, DOI:10.1080/21681163.2013.878668.
- [6] Budzik, G., Turek, P. (2018). Improved accuracy of mandible geometry reconstruction at the stage of data processing and modeling. *Australasian Physical & Engineering Sciences in Medicine*, vol. 41, no. 3, p. 687-695, DOI:10.1007/s13246-018-0664-5.
- [7] Ford, J.M., Decker, S.J. (2016). Computed tomography slice thickness and its effects on three-dimensional reconstruction of anatomical structures. *Journal of Forensic Radiology and Imaging*, vol. 4, p. 43-46, DOI:10.1016/j.jofri.2015.10.004.
- [8] Makitie, A., Paloheimo, M., Björkstrand, R., Paloheimo, K., Tuomi, J., Salmi, M. (2009). Medical applications of rapid prototyping - from applications to classification. da Silva Bartolo, P.J., Jorge, M.A., da Conceicao Batista, F., Almeida, H.A., Matias, J.M., Vasco, J.C., Gaspar, J.B., Correia, M.A., Andre, N.C., Alves, N.F., Novo, P.P., Martinho, P.G., Carvalho, R.A. (Eds.), *Innovative Developments in Design and Manufacturing*. CRC Press, Boca Raton, p. 701-704, DOI:10.1201/9780203859476.ch109.
- [9] Huotilainen, E., Jaanimets, R., Valášek, J., Marcián, P., Salmi, M., Tuomi, J., Mäkitie, A., Wolff, J. (2014). Inaccuracies in additive manufactured medical skull models caused by the DICOM to STL conversion process. *Journal of Cranio - Maxillofacial Surgery*, vol. 42, no. 5, p. e259-e265. DOI:10.1016/j.jcms.2013.10.001.
- [10] Salmi, M., Tuomi, J., Paloheimo, K., Paloheimo, M., Björkstrand, R., Makitie, A.A., Mesimäki, K., Kontio, R. (2009). Digital design and rapid manufacturing in orbital wall reconstruction. da Silva Bartolo, P.J., Jorge, M.A., da Conceicao Batista, F., Almeida, H.A., Matias, J.M., Vasco, J.C., Gaspar, J.B., Correia, M.A., Andre, N.C., Alves, N.F., Novo, P.P., Martinho, P.G., Carvalho, R.A. (Eds.), *Innovative Developments in Design and Manufacturing*. CRC Press, Boca Raton, p. 339-342, DOI:10.1201/9780203859476.ch52.
- [11] Sonka, M., Hlavac V., Boyle, R. (1999). *Image Processing, Analysis, and Machine Vision*, PWS Publishing, Pacific Grove.
- [12] Chaira, T. (2014). An improved medical image enhancement scheme using Type II fuzzy set. *Applied Soft Computing*, vol. 25, p. 293-308, DOI:10.1016/j.asoc.2014.09.004.
- [13] Ooi, C.H., Kong, N.S.P., Ibrahim, H. (2009). Bi-histogram equalization with a plateau limit for digital image enhancement. *IEEE Transactions on Consumer Electronics*, vol. 55, no. 4, p. 2072-2080, DOI:10.1109/TCE.2009.5373771.
- [14] Guo, Y., Şengür, A., Ye, J. (2014). A novel image thresholding algorithm based on neutrosophic similarity score. *Measurement*, vol. 58, p. 175-186, DOI:10.1016/j.measurement.2014.08.039.
- [15] Finkšt, T., Tasič, J.F., Zorman Terčelj, M., Meža, M. (2017). Classification of malignancy in suspicious lesions using autofluorescence bronchoscopy. *Strojniški vestnik - Journal of Mechanical Engineering*, vol. 63, no. 12, p. 685-695, DOI:10.5545/sv-jme.2016.4019.
- [16] Finkšt, T., Tasič, J.F., Terčelj-Zorman, M., Zajc, M. (2012). Autofluorescence bronchoscopy image processing in the selected colour spaces. *Strojniški vestnik - Journal of Mechanical Engineering*, vol. 58, no. 9, p. 501-508, DOI:10.5545/sv-jme.2012.350.
- [17] Martinović, M., Stoić, A., Kiš, D. (2008). Segmentation of the CT image using self-organizing neural networks. *Tehnički vjesnik - Technical Gazette*, vol. 15, no. 4, p. 23-28.
- [18] Žagar, M., Kovač, M., Hofman, D. (2012). Framework for 4D medical data compression. *Tehnički vjesnik - Technical Gazette*, vol. 19, no. 1, p. 99-105.
- [19] Zhao, X., Wu, Y., Song, G., Li, Z., Zhang, Y., Fan, Y. (2018). A deep learning model integrating FCNNs and CRFs for brain tumour segmentation. *Medical Image Analysis*, vol. 43, p. 98-111, DOI:10.1016/j.media.2017.10.002.
- [20] Li, B.N., Chui, C.K., Chang, S., Ong, S.H. (2011). Integrating spatial fuzzy clustering with level set methods for automated medical image segmentation. *Computers in Biology and Medicine*, vol. 41, no. 1, p. 1-10, DOI:10.1016/j.combiomed.2010.10.007.
- [21] Li, C., Gore, J.C., Davatzikos, C. (2014). Multiplicative intrinsic component optimization (MICO) for MRI bias field estimation and tissue segmentation. *Magnetic Resonance Imaging*, vol. 32, no. 7, p. 913-923, DOI:10.1016/j.mri.2014.03.010.
- [22] Aja-Fernández, S., Curiale, A.H., Vegas-Sánchez-Ferrero, G. (2015). A local fuzzy thresholding methodology for multiregion image segmentation. *Knowledge-Based Systems*, vol. 83, no. 1, p. 1-12, DOI:10.1016/j.knsys.2015.02.029.
- [23] Gupta, D., Anand, R.S., Tyagi, B. (2015). A hybrid segmentation method based on Gaussian kernel fuzzy clustering and region based active contour model for ultrasound medical images. *Biomedical Signal Processing and Control*, vol. 16, p. 98-112, DOI:10.1016/j.bspc.2014.09.013.
- [24] Rastgarpour, M., Shanbehzadeh, J., Soltanian-Zadeh, H. (2014). A hybrid method based on fuzzy clustering and local region-based level set for segmentation of inhomogeneous medical images. *Journal of Medical Systems*, vol. 38, no. 8, p. 1-15, DOI:10.1007/s10916-014-0068-3.
- [25] Vishnuvarthanan, G., Pallikonda Rajasekaran, M., Subbaraj, P., Vishnuvarthanan, A. (2016). An unsupervised learning method with clustering approach for tumour identification and tissue segmentation in magnetic resonance brain. *Applied Soft Computing*, vol. 38, p. 190-212, DOI:10.4172/jceni.1000101.
- [26] Mousavi, M., Yap, H.J., Musa, S.N., Dawal, S.Z.M. (2017). A fuzzy hybrid GA-PSO algorithm for multi-objective AGV scheduling in FMS. *International Journal of Simulation Modelling*, vol. 16, no. 1, p. 58-71, DOI:10.2507/IJSIMM16(1)5.368.
- [27] Bezdek, J.C. (1983). Pattern recognition with fuzzy objective function algorithms. *SIAM Review*, vol. 25, no. 3. p. 442-442, DOI:10.1137/1025116.

- [28] Zhu, Y., Huang, C. (2012). An Improved median filtering algorithm for image noise reduction. *Physics Procedia*, vol. 25, p. 609-616, DOI:10.1016/j.phpro.2012.03.133.
- [29] Fan, J., Zeng, G., Body, M., Hacid, M.S. (2005). Seeded region growing: An extensive and comparative study. *Pattern Recognition Letters*, vol. 26, no. 8, p. 1139-1156, DOI:10.1016/j.patrec.2004.10.010.
- [30] Mehnert, A., Jackway, P. (1997). An improved seeded region growing algorithm. *Pattern Recognition Letters*, vol. 18, no. 10, p. 1065-1071, DOI:10.1016/S0167-8655(97)00131-1.
- [31] Otsu, N. (1979). A threshold selection method from gray-level histograms. *IEEE Transactions on Systems, Man, and Cybernetics*, vol. 9, no. 1, p. 62-66, DOI:10.1109/TSMC.1979.4310076.
- [32] Abu-Ain, W., Abdullah, S.N.H.S., Bataineh, B., Abu-Ain, T., Omar, K. (2013). Skeletonization algorithm for binary images. *Procedia Technology*, vol. 11, p. 704-709, DOI:10.1016/j.protcy.2013.12.248.
- [33] Schulze, R., Heil, U., Groß, D., Bruellmann, D.D., Dranischnikow, E., Schwanecke, U., Schoemer, E. (2011). Artefacts in CBCT: A review. *Dentomaxillofacial Radiology*, vol. 40, no. 5, p. 265-273, DOI:10.1259/dmfr/30642039.
- [34] Fox, A., Basrani, B., Kishen, A., Lam, E.W.N. (2018). A novel method for characterizing beam hardening artifacts in cone-beam computed tomographic images. *Journal of Endodontics*, vol. 44, no. 5, p. 869-874, DOI:10.1016/J.JOEN.2018.02.005.
- [35] Budak, I., Mirkovic, S., Sokac, M., Santosi, Z., Puskar, T., Vukelic, D. (2016). An approach to modelling of personalized bone grafts based on advanced technologies. *International Journal of Simulation Modelling*, vol. 15, no. 4, p. 637-648, DOI:10.2507/IJSIMM15(4)5.357.
- [36] Ghaffarian, S., Ghaffarian S. (2014). Automatic histogram-based fuzzy C-means clustering for remote sensing imagery. *ISPRS Journal of Photogrammetry and Remote Sensing*, vol. 97, p. 46-57, DOI:10.1016/j.isprsjprs.2014.08.006.
- [37] Zhang, Y., Mańdziuk, J., Quek, C.H., Goh, B.W. (2017). Curvature-based method for determining the number of clusters. *Information Sciences*, vol. 415-416, p. 414-428, DOI:10.1016/j.ins.2017.05.024.
- [38] Zhou, Y., Zhao, T., Wang, Y., Wu, J., Zhou, X. (2018). A linear fitting density peaks clustering algorithm for image segmentation. *Tehnički vjesnik - Technical Gazette*, vol. 25, no. 3, p. 808-812, DOI:10.17559/tv-20171125161944.

Selected Microstructural and Mechanical Properties of Open-Cell Metal Foams

Wojciech Depczyński*

Kielce University of Technology, Faculty of Mechatronics and Mechanical Engineering, Poland

The microstructure and mechanical properties of open-cell metal foams have long been studied from various angles. The materials discussed in this paper were fabricated using an unconventional sintering method and their properties are unique. An important part of the process is reduction of Fe(III) oxide, acting as a foaming agent and a space holder. Four powder mixtures were analysed: ASC100.29, ASC100.29 + C, DISTALLOY SE and DISTALLOY SE + C. The aim of the tests, performed with a specially developed setup, was to determine the impact energy absorption capacity of the Fe-based foams. From the results, it is clear that the metal foams can be used in many applications, including lightweight structures, filters, heat exchangers and energy-absorbing systems.

Keywords: open-cell metal foams, Fe-based foams, reduction of metal oxides, space holder technique, energy dissipation

Highlights

- The Fe-based metal foams were produced through sintering, which is an efficient and cost-effective process.
- The reduction of Fe (III) oxide by hydrogen and the addition of Cu were responsible for a uniform structure and open porosity. The average pore diameter did not exceed 100 μm ; the porosity ranged from 67.9 % to 80.3 %, depending on the powder mixture composition.
- The motion of the hammer striking the material was monitored using a time-lapse camera.
- The Fe-based foams seem suitable for lightweight structures, energy-dissipating and energy-absorbing systems, filters, catalytic converters, and heat exchangers.

0 INTRODUCTION

Iron has been used as a basic material for everyday tools and weapons since prehistoric times. After the 19th century, which saw the emergence of new technologies for the production of iron-based alloys, steel has become ubiquitous, especially in construction. Now, with dynamic changes in technology, there is a need for new classes of materials that exhibit new characteristics.

Looking for inspiration and solutions to difficult problems, engineers and scientists all over the world have often used nature, the best source of knowledge. For example, Ashby [1] wrote, “When modern man builds large load-bearing structures, he uses dense solids: steel, concrete, glass. When nature does the same, she generally uses cellular materials: wood, bone, coral”.

Numerous experiments have been carried out to verify concepts concerning the fabrication and application of structural sponge-like materials. Some of the first successful attempts to produce foam materials for structural purposes led to the creation of porous polymer membranes [2] and porous polymer electrolytes [3]. Much of the research in this area has focused on the fabrication of advanced metal foams [4]. Several technologies have been invented to produce metal foams with closed or open

porosity, with a crystalline or amorphous structure, and with pores ranging from a micrometre to several millimetres in size [5] and [6].

These efforts have resulted in many new applications, e.g. aluminium sound absorbers, copper heat exchangers, and nickel battery electrodes. However, Arwade et al. [7] complained, “Steel is one of the most widely used engineering materials, yet today no foam using steel as the base material is commercially available”. Further research is thus essential to develop efficient and cost-effective methods to produce Fe-based foam materials with desirable properties [8] and [9].

Sintering is one of the cheapest and most efficient methods to fabricate porous iron-based materials. It is not necessary to reach the melting point of iron to obtain a desired structure; porosity is achieved by using a space holder or a foaming agent. Bekoz and Oktay [10] fabricated sintered low-alloy steel foams using the space holder-water leaching technique. Their materials had porosity ranging from 47.8 % to 70.9 %, depending on the space holder size (500 μm to 1200 μm). Murakami et al. [11] produced iron foams using CO and CO₂ as foaming gases; their maximum porosity was 55 %, and an average pore was 500 μm in size. These processes, however, involved powder compaction, which had a negative effect on the material structure. The sintered porous

*Corr. Author's Address: Kielce University of Technology, Faculty of Mechatronics and Mechanical Engineering, 25-314 Kielce, Poland, wdep@tu.kielce.pl

iron-based material discussed in this article differs from conventionally produced iron foams in that no compaction of powders is applied [12].

The motivation for this project was that there are hardly any studies on the behaviour of open-cell Fe-based foams used as energy absorbers.

1 MATERIALS AND METHODS

The foams to be tested were produced using the sintering method described in Patent PL 199720 B1 [13]. The technology involves adding some oxide easy to reduce by hydrogen to act both as a foaming agent and a space holder. In this study, Fe (III) oxide was employed. Reacting with the atmosphere used during sintering, Fe (III) oxide was reduced to iron by hydrogen from dissociated ammonia to create hollow spaces inside the material.

Another important factor contributing to the production of a cellular structure is the presence of water vapour and CO and/or CO₂. These gases act as foaming agents. Released from the spaces occupied by

the sintered powder, they create open interconnected cells. This method has been successfully tested to produce copper foams (Cu + CuO + Cu₂O sintered in a reducing atmosphere of dissociated ammonia) to be used for enhanced heat transfer surfaces in heat exchangers operating in the nucleate boiling mode [14] and [15]. The copper-based foams, being 0.2 mm to 1 mm in thickness, had a porosity of 45 % to 70 %. The open pores ranged from about 50 μm to 100 μm in size. Since very good results were reported for the copper-based foams, research was undertaken to study the use of Fe and its oxides.

2 EXPERIMENT

The compositions of the metal precursors were designed using commercially available powders: Hoggas atomized iron powder ASC100.29, Hoggas diffusion-alloyed powder DISTALOY SE, Chempur iron(III) oxide powder, Poch Norit SX2 carbon powder and Amil copper powder. The four mixtures created were labelled as: ASC100.29, ASC100.29 + C,

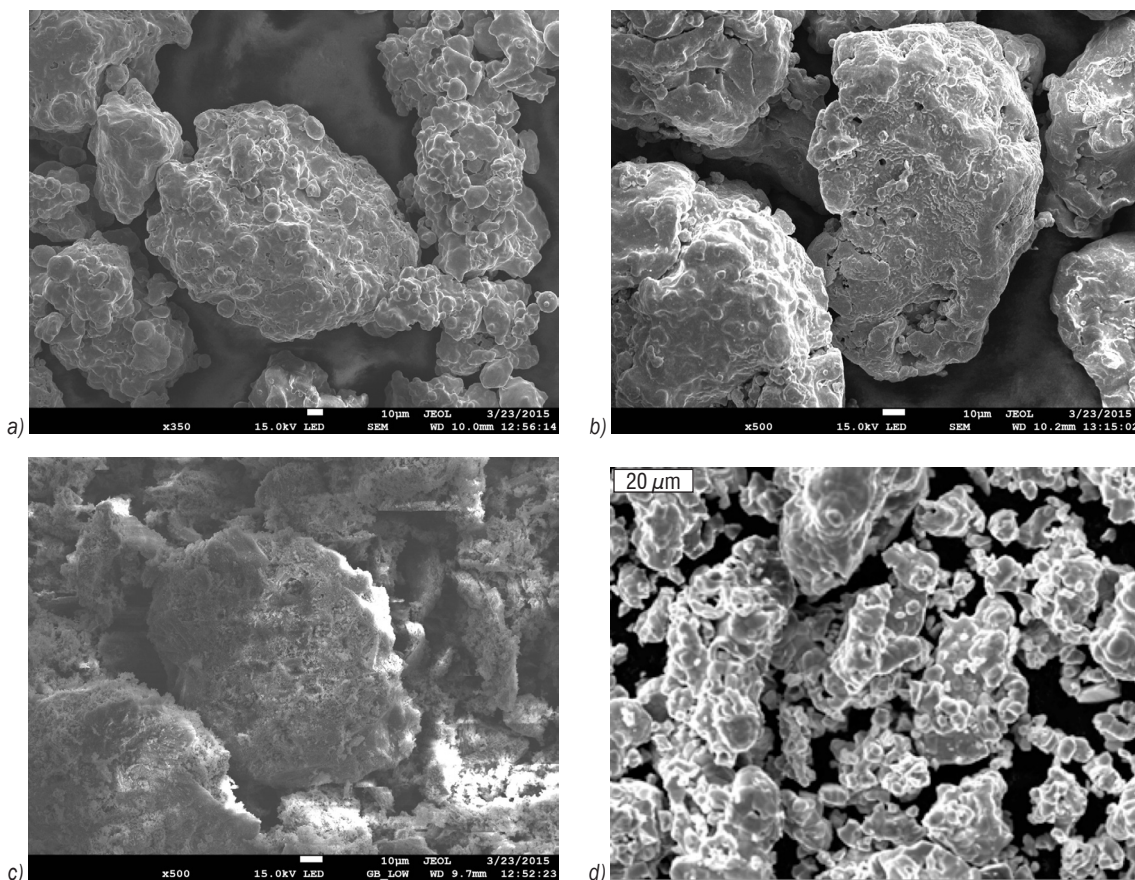


Fig. 1. SEM images of the constituent powders: a) ASC 100.29, b) DISTALOY SE, c) iron (III) oxide, and d) copper

DISTALOY SE, and DISTALOY SE + C. All of them had copper added, to act as a diffusion catalyst, and iron (III) oxide, to function as a foaming agent and a space holder. All the mixture constituents were in powder form. The chemical compositions of the iron powders are shown in Table 1. The powder mixtures were not compacted; the particles were only affected by gravity. The shape and dimensions of the dies (steel containers) determined the shape and dimensions of the sintered specimens. The containers measured 30 mm × 50 mm × 100 mm.

Table 1. Compositions of the iron powders

Powder	Chemical composition, [%]					
	C	Cu	Ni	Mo	O	Fe
ASC100.29	< 0.01	-	-	-	-	bal
DISTALOY SE	< 0.01	1.5	4	0.5	-	bal

Scanning electron microscopy (SEM) analysis was performed to have a closer look at the size and shape of particles within the constituent powders. Fig. 1 shows the SEM images taken using a JOEL JSM-7100F microscope.

Table 2 provides the percent compositions of the powder mixtures used. To simplify the names of the materials, ASC100.29 will be shortened to ASC, and DISTALOY SE to SE.

Table 2. Percent compositions of the powder mixtures to be sintered

Constituents	Powder mixture composition [%]			
	ASC	ASC + C	SE	SE + C
ASC100.29	85	85	-	-
DISTALOY SE	-	-	85	85
Cu	5	4.2	5	4.2
Iron (III) oxide	10	10	10	10
C	-	0.8	-	0.8

The specimens were fabricated by sintering at a temperature of 1130 °C in a tube furnace. Iron (III) oxide was reduced by hydrogen from dissociated ammonia.

After sintering for 50 minutes, the specimens were placed in the cooling chamber. High temperature and the presence of hydrogen contributed to the reduction of iron (III) oxide. Hollow spaces formed inside the solid structure. The iron (III) oxide reduction was the major factor in the porosity formation. Iron powder particles adhered to one another to form diffusion connections. At 1085 °C, the copper powder underwent a phase transition process (solid to liquid). The melted copper acted as a reaction catalyst.

3 RESULTS

3.1 Microstructural Characterisation

The foam materials fabricated through sintering in steel containers were tested as energy absorbers. Since Kujime et al. [16] reported spark erosion to be the most suitable for cutting porous carbon steel,

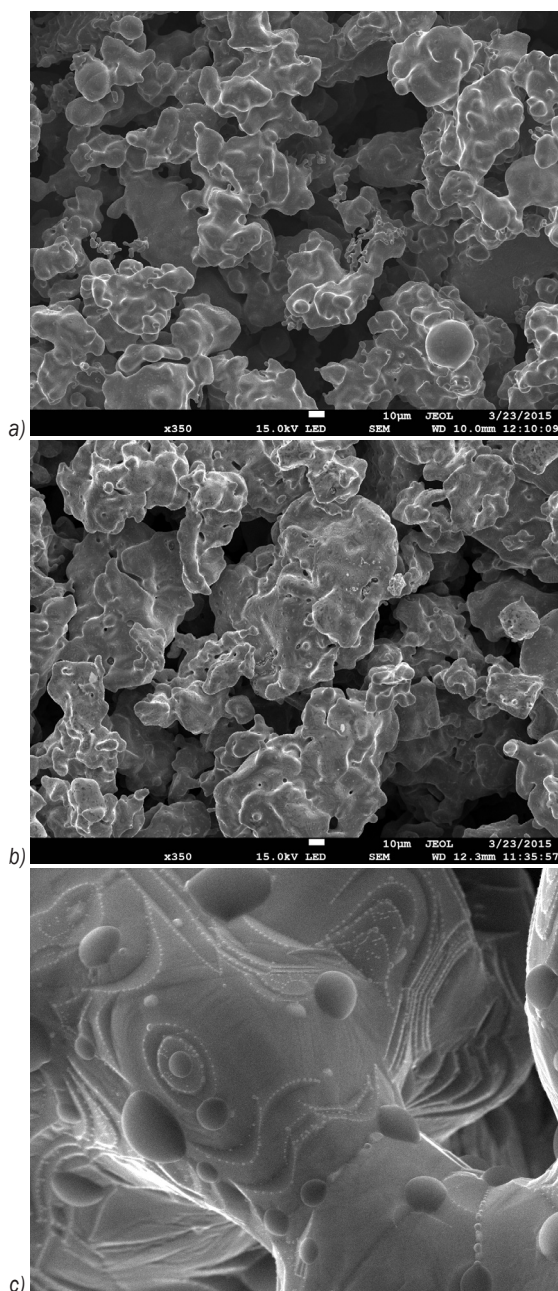


Fig. 2. SEM images of the sintered iron based powders: a) ASC (magnification 350x), b) SE (magnification 350x) and c) SE (magnification 5000x), a bridge between particles visible

this method was selected to prepare the specimens for metallographic examinations. The specimens, 14 mm in thickness and 16 mm in diameter, were geometrically symmetrical. Some of the cross-sectional specimens were etched using Nital to reveal the microstructure of the porous material. Optical (OM) and SEM examinations were used to characterize the foams. An interesting observation during the SEM analysis was that copper in the liquid state initiated formation of diffusion connections between the spherical iron particles. The results can be seen in Fig. 2.

The structure generated in the sintering process was of the open-cell type. Determining the average size of pores was not easy because of their random arrangement. The pore diameter, which was approximately 100 μm , was determined on the basis of OM measurements in longitudinal and cross-sectional planes using Nikon NIS-Element AR imaging software. The Cavalieri-Hacquet principle was employed for the pore size estimation. The reduction of Fe_2O_3 , acting as a space holder, greatly contributed to the formation of a network of interconnected open pores. Fig. 2c shows a bridge between two Fe particles being a result of diffusion.

The porosities of the foam materials were determined using optical microscopy. For ASC, ASC + C, SE and SE + C, they were: 67.9, 77.8, 75.7 and 80.3, respectively. Porosity was measured in the longitudinal and cross-sectional planes using NIKON NIS-Elements AR imaging software. Again, the Cavalieri-Hacquet principle was applied.

3.2 Impact Testing

An important mechanical property of porous metal materials is high impact energy absorption capacity. The impact tests were performed using a specially developed setup shown in Fig. 3.



Fig. 3. The setup for performing impact energy absorption tests

The experiments consisted in striking a foam-filled steel container using a special hammer with a

known mass. The motion of the hammer striking a specimen was monitored using a time-lapse camera (Fig. 4).

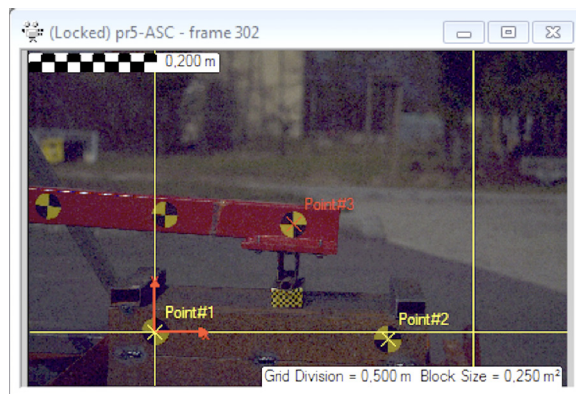


Fig. 4. Hammer motion analysis using TEMA Motion

TEMA Motion software was applied to analyse the motion of the moving hammer.

Six specimens were tested. They were all steel containers with different contents. Four were filled with sintered powders: ASC, ASC + C, SE and SE + C (Fig. 5). There were a further two containers tested, one empty and the other filled with sawdust.



Fig. 5. The steel containers filled with different iron-based porous materials before the impact tests

All the tests were conducted under approximately the same conditions. The hammer mass was $m = 2.3$ kg. Fig. 6 shows the maximum decelerations obtained using the TEMA Motion software.

The TEMA MOTION data were used to determine the hammer deceleration, which was approximately 8000 [m/s^2], i.e. 800 G. The speed of the striking hammer was 11 [m/s]. The impact lasted for about 25.5 milliseconds. Then, the hammer bounced off the specimen. The kinetic energy of the impact was 139.15 J. The deformation that the energy absorbers suffered can be seen in Figs. 7 and 8.

The empty container used for calibration was completely destroyed. The same effect was observed for the container with sawdust. The proper specimens, i.e. the containers filled with ASC, ASC + C, SE and SE + C powders were deformed to varying degrees.

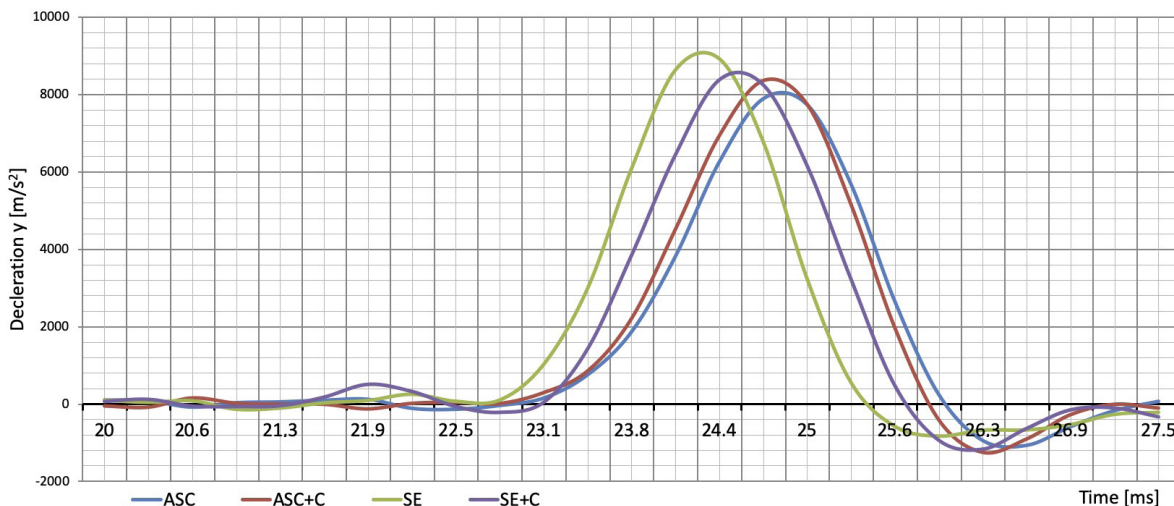


Fig. 6. Deceleration vs. time for the ASC, ASC + C, SE and SE + C specimens

Each specimen absorbed a different amount of the kinetic energy of the impact, depending on the filling properties of the foam.



Fig. 7. Front view of the deformed specimens; from left: four containers filled with foam materials, one filled with sawdust and one empty



Fig. 8. Cross sections of the deformed specimens

The first test was conducted for ASC. During the 25.5 millisecond impact, the hammer came into contact with the test piece for up to 37 milliseconds. This caused a displacement of 0.013 [m]. The displacements measured for the other materials, i.e. ASC + C, SE and SE + C are given in Table 3.

Table 3. Deformation of the steel containers filled with the porous materials tested

Absorber	Displacement [m]	Mass [g]
ASC	0.013	443.20
ASC + C	0.008	435.32
SE	0.007	450.84
SE + C	0.009	430.10

4 DISCUSSION

High porosity observed in all the four materials was a combined result of the properly designed powder mixture composition and the optimal sintering conditions. The sintering at 1130 °C for 50 minutes resulted in a uniform distribution of pores. If a shorter heating time and a lower heating temperature had been used, the reduction of iron (III) oxide would have been insufficient and pore formation retarded. There was no phase transition for iron particles, but they formed a network of interconnected cells. The change of solid copper powder particles into a liquid phase led to an increase in energy at the iron grain boundaries. Copper was also used as the foaming agent producing open interconnected cells.

The findings of Murakami et al. [11] on iron-based porous materials have contributed to a better understanding of the nature of the iron foam formation process involving the occurrence of a semi-liquid phase. The use of 1 % of hematite [Fe₂O₃] as a foaming agent helped produce a material with a maximum porosity of 55 %, where pores ranged from 500 μm to 800 μm in size. When the content of hematite exceeded 1 %, the porosity decreased. Murakami et al. observed, “While the increase in the hematite content increases the amount of foaming gas and consequently the porosity, the excess amount of gas generated by the addition of an excess amount of the foaming agent appears to decrease the porosity. However, the addition of an excess amount of hematite may yield pores with a high pressure in the melt, which may bubble out from the melt” [11]. It is interesting to note

that when hematite was relatively high, i.e. at 2 %, the pore diameters decreased with an increase in porosity. This finding corresponds to the results obtained in this study; the addition of 10 % Fe (III) oxide by volume led to the formation of pores approximately 100 μm in diameter.

The formation of porosity at the macro and micro scales was investigated by Bekoz and Oktay [10] for low-alloy steel foams. As they used carbamide as a space holder, macro pores were more than 1000 μm in diameter. The sintering of Hoganas Distaloy AB steel powder at 1200 °C for 60 minutes contributed to the formation of micropores with a diameter of less than 100 μm . The sintering conditions were very similar to those discussed in this article. It is possible, however, that the micro porosity obtained by Bekoz and Oktay [10] was a side effect of the application of carbamide as a space holder.

Internal porosity can be developed in a number of ways. Kujime et al. [16], for example, applied the gas entrapment method, which involved supplying pressurized hydrogen and helium to a melted metal to produce porous carbon steel with a porosity of 26 % to 44 % and a pore diameter of 500 μm to 700 μm . Compared with the materials described in this article, their lotus-type foams had a structure with larger pores and lower porosity. The gas blowing method they employed differed from the conventional techniques of porosity formation. It can thus be concluded that the porosity of the lotus-type steel foam increases with increasing partial pressure of hydrogen gas [16].

Another important factor that defines a porous structure is the gas pressure exerted on the material during the sintering process. Saadatfar et al. [17] studied the influence of air overpressure on the porosity level using X-ray micro-computed tomography (micro-CT) for non Fe-based metal foams. All the specimens analysed in this paper were prepared under a pressure of 1 bar. In his earlier paper [18], the author provides the micro-CT results obtained for similarly fabricated Cu-based foams, where the foaming agent is copper oxide.

The optical microscopy was very useful for determining the percent porosities and pore diameters, but it was not sufficiently accurate to characterize the foam microstructures and, accordingly, the pore formation process. SEM was a suitable method to analyse foam structures in more detail. Maire et al. [19] remark, "The complex 3D architecture of solid foams requires observation techniques permitting a high depth of field. Amongst the standard available techniques, only SEM shows enough depth of focus to apprehend the structure of these materials". The author

of this article successfully modelled the structures of similar foams and compared them with SEM images, as described in [20].

Uniform porosity observed in the foams described in this article was a result of two main factors: mechanical mixing of powders and reduction of iron (III) oxide at constant temperature during sintering. By contrast, Rabei et al. [21], who deal with iron-based porous structures applied pre-sintering vibration, which led to considerable differences in porosity between the powder matrix and the hollow spheres embedded in it. The vibration caused part of the powder to adhere to the sphere walls with the rest forming uncompact matrix.

Applications of metal foams include energy absorbers. Research in this area has involved experiments as well as modelling and simulation [22] to [24]. The empirical data concerning the impact energy absorption capacity of the four foams analyzed in this paper seem promising. The highest values were reported for the ASC foam, while the lowest for SE. Thus, the ASC specimen was the most deformed and the SE the least. Also, the SE foam had the lowest porosity because of the highest mass. The ASC+C and SE +C specimens exhibited similar energy absorption performance, worse than ASC and better than SE, respectively. In all the cases, deformation was directly dependent on the hammer deceleration. The presence of carbon in the powder mixtures resulted in higher porosity of the foams. When added to SE, it improved its energy dissipation efficiency. On the other hand, the addition of carbon to ASC caused a slight decrease in the material energy absorption performance, which was due to changes in the strength of diffusion connections between iron particles. As carburization occurred, an increase in the carbon content improved the strength properties of this material (ASC + C).

From the deformation behaviour of the materials tested, it is apparent that they had a potential to absorb more energy. As they were fabricated through powder metallurgy, their parameters, which are dependent on the powder mixture composition, are easy to control.

There are no standards for energy absorption measurement and then interpretation of results obtained for open-cell, closed-cell or syntactic metal foams, which makes the comparison of impact test data difficult. Results from static tests, such as quasi-static compression tests, are more comparable [25] to [27]. The results of the dynamic tests described in this paper were obtained at a relatively small energy impact of less than 140 J, which resulted from the test setup design. Drop-weight (Pellini) tests would have provided more accurate data.

5 CONCLUSIONS

This paper has dealt with a powder metallurgy method of preparing open-cell metal-foams. Sintering processes are much more energy-efficient and cheaper than other techniques used to produce porous metal materials. The Fe-based foams tested had structures that are controllable to some extent. Their porosity depended on the composition of the powder mixture, and thus indirectly on the size and shape of grains. The chemical compositions of the materials to be sintered were carefully designed to ensure proper filling of the steel die.

The metal foams were characterized using optical and SEM analysis. Both techniques are suitable to determine the differences in microstructure. Porosity was largely dependent on the powder mixture composition. The presence of alloying elements may have been the reason for higher porosity of the sintered materials. As the phenomenon is not easy to explain, there is a need for further research in this area.

The tests performed with a specially developed setup showed that the Fe-based metal foams had high impact energy absorption capacity because of their high porosity. The relationship between these two properties should be further investigated.

Materials with similar porosity, e.g. ones with a lotus-type structure have so far been fabricated through technologies involving a liquid-phase, which is far more expensive than the method described here.

Open-cell Fe-based foams produced in this way are likely to be used in applications including lightweight structures, energy-dissipating and energy-absorbing systems filters, catalytic converters and heat exchangers.

6 ACKNOWLEDGMENTS

Special thanks to dr hab. inż. Marek Jaśkiewicz and other staff members of the Department of Automotive Engineering and Transport at the Faculty of Mechatronics and Mechanical Engineering of the Kielce University of Technology, for access to their laboratory and their assistance during the tests.

7 REFERENCES

- [1] Ashby, M.F. (1983). The mechanical properties of cellular solids. *Metallurgical Transactions: A*, vol. 14, no. 9, p. 1755-1769, DOI:10.1007/BF02645546.
- [2] van de Witte, P., Dijkstra, P.J., van den Berg, J.W.A., Feijen, J. (1996). Phase separation processes in polymer solutions in relation to membrane formation. *Journal of Membrane Science*, vol. 117, no. 1-2, p. 1-31, DOI:10.1016/0376-7388(96)00088-9.
- [3] Cao, J.-H., Zhu, B.-K. Xu, Y.-Y. (2006). Structure and ionic conductivity of porous polymer electrolytes based on PVDF-HFP copolymer membranes. *Journal of Membrane Science*, vol. 281, no. 1-2, p. 446-453, DOI:10.1016/j.memsci.2006.04.013.
- [4] Banhart, J. (2013). Light-metal foams—History of innovation and technological challenges. *Advanced Engineering Materials*, vol. 15, no. 3, DOI:10.1002/adem.201200217.
- [5] Oriňáková, R., Andrej Oriňák, A., Markušová Bučková, L., Giretová, M., Medvecký, L., Evelína Labbanczová, E., Kupková, M., Monika Hrubovčáková, M., Koval, K. (2013). Iron based degradable foam structures for potential orthopedic applications. *International Journal of Electrochemical Science*, vol. 8, p. 12451-12465, DOI:10.1515/pmp-2016-0008.
- [6] Brothers, A.H., Scheunemann, R., DeFouw, J.D., Dunand, D.C. (2005). Processing and structure of open-celled amorphous metal foams. *Scripta Materialia*, vol. 52, no. 4, p. 335-339, DOI:10.1016/j.scriptamat.2004.10.002.
- [7] Arwade, R.S., & Hajjar, J., Schafer, B., Moradi, M., Smith, B., Szyniszewski, S. (2011). Steel foam material processing, properties, and potential structural applications. *Structural Materials and Mechanics, Proceedings of the NSF Engineering Research and Innovation Conference*, DOI:10.1016/j.jcsr.2011.10.028.
- [8] Mutulu, I., Oktay, E. (2011). Processing and properties of highly porous 17-4 PH stainless steel. *Powder Metallurgy and Metal Ceramics*, vol. 50, no. 1-2, p. 73-82, DOI:10.1007/s11106-011-9305-1.
- [9] Jee, C.S.Y., Guo, Z.X., Evans, J.R.G., Özgüven, N. (2000). Preparation of high porosity metal foams. *Metallurgical and Materials Transactions B*, vol. 31, no. 6, p. 1345-1352, DOI:10.1007/s11663-000-0021-3.
- [10] Bekoz, N., Oktay, E. (2013). Mechanical properties of low alloy steel foams: Dependency on porosity and pore size. *Materials Science and Engineering: A*, vol. 576, p. 82-90, DOI:10.1016/j.msea.2013.04.009.
- [11] Murakami, T., Ohara, K., Narushima, T., Ouchi, C. (2007). Development of a new method for manufacturing iron foam using gasses generated by reduction of iron oxide. *Materials Transactions*, vol. 48, no. 11, p. 2937-2944, DOI:10.2320/matertrans.MRA2007127.
- [12] Park, C., Nutt, S.R. (2001). Effects of process parameters on steel foam synthesis. *Materials Science and Engineering: A*, vol. 297, no. 1-2, p. 62-68, DOI:10.1016/S0921-5093(00)01265-X.
- [13] Żórawski, W., Chatys, R., Depczyński, W. (2008). *A Method for Producing Porous Structures, Patent PL 199720 B1*, Patent Office of the Republic of Poland, Warszawa. (in Polish)
- [14] Depczyński, W. (2014). Sintering of copper layers with a controlled porous structure. *METAL 23rd International Conference on Metallurgy and Materials*, p. 1219-1224.
- [15] Wójcik, T.M. (2012). Heat transfer enhancement and surface thermo stabilization for pool boiling on porous structures. *EPJ Web of Conferences, Experimental Fluid Mechanics*, vol. 25, art. no. 01100, DOI: 10.1051/epjconf/20122501100.

- [16] Kujime, T., Hyun, S.-K., Nakajima, H. (2006). Fabrication of lotus - type porous carbon steel by the continuous zone melting and its mechanical properties. *Metallurgical and Materials Transactions A*, vol. 37, no. 2, p. 393-398, DOI:10.1007/s11661-006-0009-y.
- [17] Saadatfar, M., Garcia-Moreno, F., Hutzler, S., Sheppard, A.P., Knackstedt, M.A., Banhart, J., Weaire, D. (2009). Imaging of metallic foams using X-ray micro-CT. *Colloids and Surfaces A: Physicochemical and Engineering Aspects*, vol. 344, no. 1-3, p. 107-012, DOI:10.1016/j.colsurfa.2009.01.008.
- [18] Depczyński, W. (2014). Investigating porosity of sintering porous copper structure with 3D micro-focus X-ray computed tomography (μ CT). *Journal of Achievements in Materials and Manufacturing Engineering*, vol. 66, no. 2, p. 67-72.
- [19] Maire, É, Adrien, J., Petit, C. (2014). Structural characterization of solid foams. *Comptes Rendus Physique*, vol. 15, no. 8-9, p. 674-682, DOI:10.1016/j.crhy.2014.09.001.
- [20] Depczyński, W., Kazała, R., Ludwinek, K., Jedynek, K. (2016). Modelling and Microstructural characterization of sintered metallic porous materials. *Materials*, vol. 9, no. 7, art. no. 567, DOI:10.3390/ma9070567.
- [21] Rabei, A., Vendra, L., Reese, N., Young, N., Neville, B.P. (2006). Processing and characterization of a new composite metal foam. *Materials Transactions*, vol. 47, no. 9, p. 2148-2153, DOI:10.2320/matertrans.47.2148.
- [22] Marx, J., Portanova, M., Rabiej, A. (2018). A study on blast and fragment resistance of composite metal foams through experimental and modeling approaches. *Composite Structures*, vol. 194, p. 652-661, DOI:10.1016/j.compstruct.2018.03.075.
- [23] Garcia-Avila, M., Portanova, M., Rabiej, A. (2014). Ballistic performance of a composite metal foam-ceramic armor system. *Procedia Materials Science*, vol. 4, p. 151-156, DOI:10.1016/j.mspro.2014.07.571.
- [24] Garcia-Avila, M., Portanova, M., Rabiej, A. (2015). Ballistic performance of a composite metal foam. *Composite Structures*, vol. 125, p. 202-211, DOI:10.1016/j.compstruct.2015.01.031.
- [25] Depczynski, W., Miłek, T., Nowakowski, Ł. (2017). Experimental comparison between upsetting characteristics of porous components prepared by Fe-based sintering technology. *IOP Conference Series-Materials Science and Engineering*, vol. 179, art. no. 012015, DOI:10.1088/1757-899X/179/1/012015.
- [26] Rabiej, A., Garcia-Avila, M. (2013). Effect of Various parameters on properties of composite steel foams under variety of loading rates. *Materials Science & Engineering: A*, vol. 564, p. 539-547, DOI:10.1016/j.msea.2012.11.108.
- [27] Alvandi-Tabrizi, Y., Whisler, D.A., Kim, H., Rabiej, A. (2015). High strain rate behavior of composite metal foams. *Materials Science and Engineering: A*, vol. 631, p. 248-257, DOI:10.1016/j.msea.2015.02.027.

Experimental Assessment of Turbulence Convective Heat Transfer and Pressure Drop in Annuli using Nanoporous Graphene Non-Newtonian Nanofluid

Shahin Ghanbari – Kourosh Javaherdeh*

University of Guilan, Faculty of Mechanical Engineering, Iran

In the current research work, turbulence convective heat transfer coefficient enhancement and pressure drop of nanoporous graphene non-Newtonian nanofluid were investigated in an annular tube in the developing region. The nanofluid was prepared by using nanoporous graphene in different concentrations of 0.05 wt.%, 0.1 wt.%, and 0.2 wt.% in an aqueous solution of carboxyl methyl cellulose (CMC). All thermophysical and rheological characteristics were evaluated, and pseudo-plastic (shear-thinning) rheological behaviour was observed for all samples. The results revealed that adding 0.2 wt.% nanoporous graphene to the base fluid leads to 12.4 % and 39.4 % enhancement of thermal conductivity and heat transfer coefficient, respectively. This enhancement trend was almost linear for the concentrations lower than 0.1 wt.% after which the enhancement rate was reduced significantly. Moreover, the results showed that when 0.05 and 0.1 wt.% nanoporous graphene was adopted, the thermal performance factor (TPF) was increased by 8.7 % and 16.7 %, respectively, and doubling the nanoparticle concentration from 0.1 wt.% to 0.2 wt.% could not augment the TPF; however, considering the assessed pressure drop, it also decreased it by 2.5 %. The increase of the Reynolds number led to an increase in heat transfer coefficient of all samples.

Keywords: nanoporous graphene; nanofluid; annular tube; thermal performance factor; pressure drop

Highlights

- Non-Newtonian flow and convective heat transfer characteristics were experimentally investigated through an annular tube.
- Thermal and hydrodynamic performances of turbulent flow in the annular tube were investigated for different concentrations of the non-Newtonian nanofluid.
- Results showed that the thermal and hydrodynamic performances were improved with an increase in the concentration of the non-Newtonian nanofluid.

0 INTRODUCTION

In designing equipment such as heat exchangers, heating and cooling systems, it is of great importance to provide higher convective heat transfer coefficients. Techniques aimed at enhancing heat transfer can increase the thermal efficiency of such industrial devices while minimizing the cost and size. One of the solutions specified for this problem is the utilization of nanomaterials. To prepare nanofluids, nanoparticles are dispersed in an appropriate base solution which forms a suspension [1] to [3].

The initial works on the formation of nanofluids were concentrated on using metal and metal oxide nanomaterials [4]. In this respect, Heris et al. [5] researched the effect of using Al_2O_3 /water nanofluid on convective heat transfer from which it was found that by adopting 2.5 vol.% to 3 vol.% nanoparticles, the maximum increment of heat transfer is acquired. In another research, Patel et al. [6] showed that when a mixture of 11 % Au and Ag nanoparticles are used, thermal conductivity is augmented by about 21 %. Moreover, as reported by Zarringhalam et al. [7], by using CuO/water nanofluid in forced turbulent convection in two uniaxial tubes, heat transfer is

increased by up to 57 % for the sample containing 2 vol.% nanoparticles. In addition, in some relative reviews [8] to [10], thermophysical properties of different nanofluids were compared and discussed, and the effect of each nanofluid on heat transfer capability of the industrial equipment was studied. In different studies, convective heat transfer of various nanofluids has been investigated in laminar [11] and [12] and turbulent [13] flow regimes.

After using the metal and metal oxides, researchers started to use carbonaceous nanomaterials, which possessed higher thermal conductivity [14] and [15]. Among these efforts, Amrollahi et al. assessed the effect of multiwall carbon nanotubes on the convective heat transfer coefficient in laminar and turbulent flows [16]. For 0.1 wt.% nanoporous graphene in a circular tube, 34 % increment of convective heat transfer was obtained by Naghash et al. [17] in which the laminar flow regime was considered. Moreover, Amiri et al. [18] studied the thermophysical properties of the nanofluid prepared with functionalized graphene. They showed that the ethylene glycol-functionalized graphene in the mixed solution of water and ethylene glycol, the thermal conductivity was enhanced by

*Corr. Author's Address: University of Guilan, Department of Mechanical Engineering, Rasht, Iran, javaherdeh@guilan.ac.ir

up to 0.2 W/(m·K) for the 0.2 wt.% nanoparticles in comparison to the base solution.

Additionally, Askari et al. [19] investigated two different carbon nanostructures, including multi-walled carbon nanotubes and nanoporous graphene to prepare water-based stable nanofluids. They used the carbonaceous nanofluids in the cooling tower and showed that 0.1 wt.% multi-walled carbon nanotubes (MWCNT) and nanoporous graphene increased the cooling range by up to 40 % and 67 %, respectively. Graphene oxide has also been utilized for this purpose by Ranjbarzadeh et al. [20]. In their study, different concentrations of graphene oxide were considered in a turbulent regime through an isothermal pipe. They have reported the maximum thermal performance coefficient of 1.148 for the sample possessing 0.1 vol.% graphene oxide.

A vast number of studies on nanofluids have supported the idea that the rheology of nanofluid is more probably to be non-Newtonian fluid for which simplified Newtonian model is suitable for some studies [21]. For instance, Newtonian and non-Newtonian approaches were compared by Behroyan et al. [22] to assess the numerical Nusselt number for the nanofluid, which was prepared by 1.6 vol.%. From this study, it was shown that the non-Newtonian model provides a more precise Nusselt number compared to that of the Newtonian model. Additionally, Hojjat et al. [23] investigated the properties of different metal oxides in a non-Newtonian shear thinning base fluid; they varied the nanoparticle concentration and temperature and used carboxyl methyl cellulose (CMC) as the pseudoplastic base fluid. By using highly pure graphene nanoparticles, Kole and Dey [24] studied the thermal conductivity, viscosity, and electrical conductivity of nanofluids, which were formed by using EG-distilled water as the base solution. In that research, for the prepared nanofluid and also the base solution, non-Newtonian behaviour was observed in which the nanofluid viscosity was increased by 100 % in comparison to the base fluid.

In addition, there have been studies on the application of nanofluids in the annular passage for better thermal performance due to uses of this geometry in different industries [25]. In this context, a numerical investigation on the fluid flow and convective heat transfer of non-Newtonian nanofluid was carried out by Bahiraei et al. [26] in annuli, for which, also a neural network was developed to anticipate the convective heat transfer coefficient. In addition, El-Kaddadi et al. [27] studied the heat storage by the nanofluid prepared by TiO₂ nanoparticles in an annular space, where the convective heat transfer was improved by

increasing the nanoparticle concentration. Arzani et al. numerically and experimentally investigated the thermal performance of the MWCNTs and functionalized graphene nanoplatelet in an annular heat exchanger. They showed that the carbon-based nanostructures can provide better performance in heat transfer in this geometry [28] and [29]

In the literature, researchers have carried out only a few studies on the properties of carbonaceous non-Newtonian nanofluids in annuli; however, in this paper, the convective heat transfer coefficient of nanofluids of nanoporous graphene at different concentrations is evaluated experimentally in an annular tube in turbulence flow regime. For this end, at first, the base fluid and nanofluids of nanoporous graphene were prepared with different concentrations, and in the following, all thermophysical and rheological properties were evaluated. Then, thermal performance enhancement considering the pressure drop in the system in comparison to the base fluid was assessed under constant heat flux and at different Reynolds numbers. In this regard, along with the preparation of highly efficient nanofluid for thermal applications, the optimum nanoporous graphene content was also determined.

1 MATERIALS AND METHODS

The nanoporous graphene was purchased from the Research Institute of the Petroleum Industry (RIPI, Tehran, Iran) which was synthesized via special chemical vapour deposition (CVD) technique and possessed high pore volume (2.11 cm³/g) and large specific surface area (814 m²/g) and narrow pore size distribution [17] and [30]. The scanning electron microscopy (SEM) and Transmission electron microscopy (TEM) images of the used nanoporous graphene are represented in Fig. 1 in which the highly porous nature of the graphene is evident.

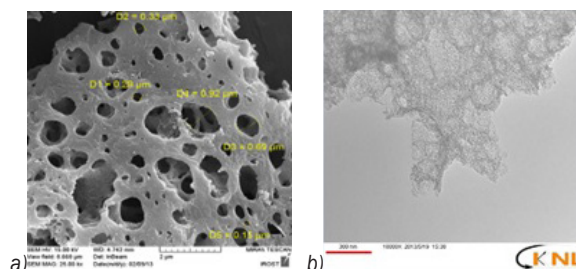


Fig. 1. a) SEM and b) TEM images of nanoporous graphene nanoparticles

In the procedure of forming the nanofluids, the nanoporous graphene nanoparticles were dispersed

in distilled water (DI) water and the CMC (with a nominal molecular weight of 900,000 g/mol and a degree of substitution (DS) of 0.8 to 0.95 by Dae-Jung company, South Korea) was utilized as the surfactant in 0.2 wt.%. Dispersion of the nanoparticles to prepare a uniform nanofluid was performed through the physical method by ultrasonic device for 4 h, and a low-speed magnetic stirrer was employed to ensure the homogeneity of the base fluid (DI water and 0.2 wt.% CMC) for 30 min. Although the addition of 0.2 wt.% CMC increases the duration of using an ultrasonic device compared to other surfactants, its bubbling effects are negligible, especially at high Reynolds numbers, and provides acceptable stability in the required experiments. To investigate the thermal performance of nanoporous graphene in annuli, suspensions with concentrations of 0.05 wt.%, 0.1 wt.% and 0.2 wt.% were prepared and labelled as NPG-0.05, NPG-0.1, and NPG-0.2, respectively. Fig. 2 shows the nanofluid which was prepared by using 0.2 wt.% nanoporous graphene. For minimizing the problems related to potential clustering and sedimentation of nanoparticles, a new nanofluid was formed and used immediately in each test.



Fig. 2. The nanofluid sample which was prepared by using 0.2 wt.% nanoporous graphene, 0.2 wt.% CMC and DI water labelled as NPG-0.2

Fig. 3 gives the apparent viscosity (η) of the base fluid and nanofluids which were prepared by different concentrations as a function of shear rate ($\dot{\gamma}$) at 25 °C. These have been measured by oscillatory and rotational rheometers (MCR 301 by Anton Par, Graz, Austria) with an accuracy of ± 2 %. As is clear from Fig. 3, by increasing the shear rate, apparent viscosity is decreased for all samples which indicate that all samples were of typical non-Newtonian fluids with shear thinning behaviour ($n < 1$) [31]. Moreover, the increase in the concentration of the nanoparticles has led to the enhancement of apparent viscosity.

The non-Newtonian behaviour of the samples can be explained by using the power law rheological model. The power law model is expressed in Eq. 1:

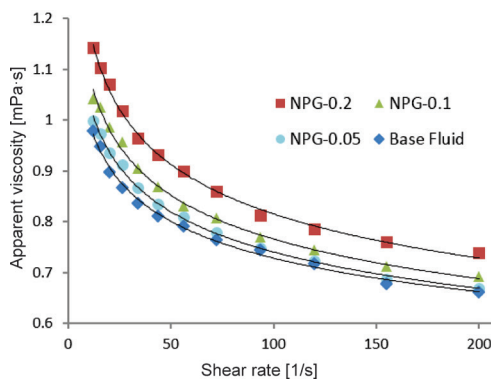


Fig. 3. Apparent viscosity of samples as a function of shear rate at 25 °C

$$\eta = m\dot{\gamma}^{n-1} \tag{1}$$

In Eq. (1), two parameters exist in terms of flow consistency index (m) and the flow behaviour index (n) which have been calculated considering the trend of apparent viscosity as a function of shear rate at 25 °C, which are given in Table 1. The heat capacity of the samples was measured by the calibrated differential scanning calorimeter (DSC-111, Setaram, France). Moreover, to calculate the density, a densitometer with an accuracy of ± 0.0001 g/cm³ was used, and the thermal conductivity was measured by employing KD2 Pro (Decagon Device, Inc., USA) with an accuracy of ± 5 %, which is tabulated in Table 1. Furthermore, to keep the temperature constant within the limit of ± 0.1 °C, all measurements were performed three times in a bath with constant temperature, and average values are reported.

Table 1. Specification of the samples at 25 °C

Sample	Flow consistency index, m	Flow behaviour index, n	Heat capacity, C_p [J/(kg·K)]	Density, ρ [kg/(m ³)]
Base fluid	0.001369	0.863	4181.2	997.1
NPG 1	0.001456	0.853	4104.8	997.3
NPG 2	0.001560	0.845	4043.4	997.6
NPG 3	0.001725	0.837	3955.0	998.7

Thermal conductivity is one of the most effective parameters that have a significant contribution to the enhancement of heat transfer coefficient [32]. Fig. 4 presents the thermal conductivity of samples in temperature ranges of 20 °C to 45 °C. As expected, the thermal conductivity of samples in all concentrations was increased by raising the temperature [33]. This is due to weakening of interparticle and intermolecular

adhesion forces at higher temperatures, which results in an increase of the Brownian motion of the particles. In addition, increasing the concentration of the nanoparticles could improve the thermal conductivity of the samples at all considered temperatures; for example, at 25 °C the increment of the thermal conductivity was 4.8 %, 9.3 %, and 12.4 % for the samples containing 0.05 wt.%, 0.1 wt.%, and 0.2 wt.% nanoparticles compared to that of the base fluid. However, this increment rate showed a decreasing trend at higher concentrations, which can be attributed to the saturation of the base fluid.

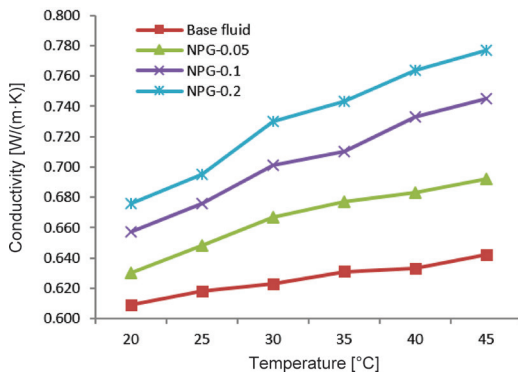
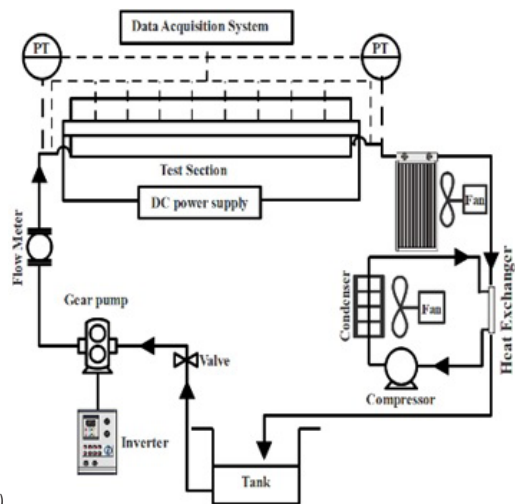


Fig. 4. The measured thermal conductivity of the prepared nanofluids and the base solution in the temperature range of 20 °C to 45 °C

2 EMPIRICAL SETUP AND METHODOLOGY

Fig. 5 shows the equipment that has been utilized in the experimental study of the annulus convective heat transfer. The apparatus is composed of a flow loop, which included an annular tube, a container of fluid, a gear pump, a cooling system, measurement systems, and control units. The annular tube part, which was 160 cm in length, comprised two tubes; the inner tube was made of Al, and the outer tube was of Plexiglas acrylic with circular cross-section ends; the inner diameter of the outer tube was 30 mm, and the outer diameter of the inner tube was 18 mm. Using Plexiglas with low thermal conductivity (approximately 0.19 W/(m·K)) in addition to decreasing the heat dissipation causes the flow regime to be observable in the test section. To provide inner uniform heat flux, an electrical element in length of 100 cm and a maximum power of 3 kW was placed inside the inner tube, and its DC power supply was controlled by a Variac. The first 55 cm of the tube without heat flux was assumed as the entrance length to create hydrodynamic fully developed conditions in the fluid.



a)



b)

Fig. 5. The experimental setup designed to measure the convective heat transfer; a) schematic illustration of the experimental setup, b) experimental setup

To measure the temperature, 10 K-type thermocouples with the accuracy of 0.1 °C were used; two were installed in entrance and outlet of the annular tube, and the remaining eight thermocouples were located over the outer surface of the inner tube in equal distances from each other. To minimize the thermal loss along the axial direction, the upstream and downstream parts of the setup were thermally insulated with thick Teflon buffers. Moreover, to indicate the decrease in thermal loss, the external surface of the tube was also thoroughly insulated. A vortex flow-meter (IFM, SV7204, Germany) was employed to measure the total fluid flow, and its value could be adjusted by changing the electromotor frequency of the pump with an inverter. The cooling system was composed of two parts: pre-cooling and cooling. The temperature of the output flow of the annular tube was reduced by a fan in pre-cooling part to reach ambient temperature, and in the cooling

part by using a plate heat exchanger and through controlling the temperature of the cold container, the temperature was reduced to the required level. In the current experiments, the temperature of the cold container is adjusted to keep the temperature of the inlet flow to the annular tube constant at 25 °C. The pressure of the outlet and inlet flows of the test section was recorded by two pressure transmitter. The experiments were performed in a steady state, and all measurements were carried out, recorded, and shown using a programmable logic controller (PLC).

2.1 Data Analysis and Validation

As the fluid flow is in the developing region, it can be stated that the heat transfer coefficient is a function of the axial position along the length of the test section (z) and, according to Eq. (2), it can be written in terms of the ratio of heat flux density (q'') and temperature gradient between the outside wall temperature of the inner tube (T_{wi}) and the fluid temperature (T_f) at each section (z).

$$h_z = \frac{q''}{T_{wi}(z) - T_f(z)}. \quad (2)$$

The inner wall heat flux (q'') is defined as in which the heat transfer rate (q) is equal to power the of the element and can be measured as $q = V \cdot I$. Through experimental measurements, while considering uniform heat flux in the wall of the inner tube, we could measure the temperature of the inner tube (T_{wi}) at each section (z), and the fluid temperature (T_f) at each section is calculated from Eq. (3):

$$T_f(z) = T_{fi} + (T_{fo} - T_{fi}) \frac{z}{L}, \quad (3)$$

where T_{fi} and T_{fo} are the fluid temperatures at the entrance and exit of the test section, which have been recorded by the installed thermocouples. In this research, as the surface temperature was measured at eight equidistant points, the average heat transfer coefficient was calculated as $h = (\sum_{j=1}^8 h_{z_j}) / 8$ [34]. Furthermore, considering the non-Newtonian effects of the samples, the Reynolds number for the power law fluids can be expressed as Eq. (4) [35]:

$$Re = \rho U^{2-n} D_h / m. \quad (4)$$

In this equation, the hydraulic diameter of the annulus tube is defined as $D_h = d_o - d_i$, and U refers to flow velocity and was measured by Eq. (5) in which

the volume flow rate is denoted by \dot{V} and measured by the flow meter. In this equation, A_{ann} refers to annulus cross section area.

$$U = \frac{\dot{V}}{A_{ann}} = \frac{4}{\pi} \cdot \frac{\dot{V}}{d_o^2 - d_i^2}. \quad (5)$$

For validation of experimental results, some experiments were initially executed for DI water, the and results were compared with the Gnielinski correlation, as follows [36]:

$$Nu = \frac{\left(\frac{f_{ann}}{8}\right) Re Pr}{k_1 + 12.7 \sqrt{\frac{f_{ann}}{8}} \left(Pr^{\frac{2}{3}} - 1\right)} \left[1 + \left(\frac{D_h}{L}\right)^{\frac{2}{3}}\right] F_{ann} K, \quad (6)$$

in which $k_1 = 1.07 + 900/Re - 0.63/(1+10 \cdot Pr)$ and for range of $0.1 \leq Pr \leq 1000$, $(D_h/L) \leq 1$ and $Re > 4000$. The friction factor of the annulus (f_{ann}) depends on the annular diameter ratio $a = (d_i/d_o)$ and is calculated from Eq. (7) [37].

$$f_{ann} = (1.8 \log Re^* - 1.5)^{-2}, \quad (7)$$

$$\text{where } Re^* = Re \frac{(1+a^2) \ln a + (1-a)^2}{(1-a^2) \ln a}.$$

The factor F_{ann} represents the different boundary conditions and for the boundary condition of heat transfer at the inner wall with the insulated outer wall can be written as $F_{ann} = (0.9 - 0.15a^{0.6})$. For liquids, the variation of fluid properties with temperature can be taken into account by using $K = (Pr_b/Pr_w)^{0.11}$, where Pr_b and Pr_w exhibit the Prandtl numbers of fluid at bulk temperature and at wall temperature, respectively [37].

Table 2 gives the experimental results and values calculated from Eqs. (6) and (7) at six different Reynolds numbers for DI water. In this calculation, the power of the element was kept constant as 2500 W, and the fluid temperature in the entrance to the test section was maintained at 25 °C. In addition, the Nusselt number is defined as Eq. (8):

$$Nu = \frac{h D_h}{k}, \quad (8)$$

All thermophysical properties of DI water at mean fluid temperature, $T_{mf} = (T_{fi} + T_{fo})/2$ have been derived from standard references [38]. The values of relative deviation in this table show that the results are acceptable by considering error limits less than 7 % and 11 % for the Nusselt number and friction factor,

respectively, and this setup can be used for measuring the heat transfer coefficients of nanoporous graphene nanofluids.

Table 2. Comparison of experimental results and Gnielinski correlation for DI water

Reynolds Number	4085	5529	7010	8415	10119	11410
Nusselt by Eq. (6)	37	46	55	64	74	81
Nusselt in present study	39	49	57	68	77	86
Relative deviation [%]	5.41	6.52	3.64	6.25	4.05	6.17
Friction factor by Eq. (7)	0.045	0.041	0.038	0.036	0.034	0.033
Friction factor in present study	0.049	0.045	0.041	0.039	0.037	0.036
Relative deviation [%]	7.65	9.75	8.04	9.83	10.16	9.73

3 RESULTS AND DISCUSSION

The local heat transfer coefficient of the base fluid and the nanofluids prepared with nanoporous graphene with three different concentrations at Re of 4000 and at a constant heat transfer rate of 2500 W were compared, and the results are displayed in Fig. 6a. Considering the location of the sensors, the local heat transfer coefficient could be recorded at eight sections. The local heat transfer coefficients of all samples, by developing the thermal boundary layer along the annular tube, was reduced to a constant value. With the decrease in heat transfer coefficient and the augment of the fluid temperature at the constant heat flux, the heat transfer to fluid was reduced, and the wall temperature increased (Fig. 6b). The wall temperature

values in Fig. 6b indicate high-temperature gradients at the beginning of the thermal region, the intensity of which was reduced by decreasing the local heat transfer coefficient along the length of the tube.

The results revealed that by using the nanoporous graphene in concentrations of 0.05 wt.%, 0.1 wt.%, and 0.2 wt.%, the average heat transfer coefficient was enhanced by 16.3 %, 30.8 %, and 39.8 %, respectively, compared to that of the base fluid which in turn led to 5.7 %, 9.8 %, and 16 % decrease in average wall temperature. In Fig. 7, the improvement percentage of heat transfer coefficient in comparison to that of thermal conductivity is plotted in terms of nanoparticle concentration. This curve implies that the improvement of heat transfer coefficient observed for the samples was higher than the mere contribution of thermal conductivity. So it is deduced that other factors influence the convective heat transfer of the nanofluids. The base solution and also the nanofluids prepared by employing nanoporous graphene displayed pseudo-plastic behaviour which means that by increasing the shear rate, apparent viscosity is decreased. Because the shear rate is higher in the vicinity of the tube wall, the apparent viscosity is lower at those regions. This leads to a decrease in thickness of the boundary layer and increment of the heat transfer rate. Furthermore, the nanoparticles dispersed in the fluid are moved from the region with a high shear rate to regions with a low shear rate. Consequently, near the wall, nanoparticle concentration is decreased, leading to lower apparent viscosity and, as a result, a thinner boundary layer is obtained [39] and [40].

Additionally, thermal dispersion as a result of random motion of the nanoparticles can also affect this enhancement and thus flatten the temperature profile. Altogether, a steeper temperature gradient

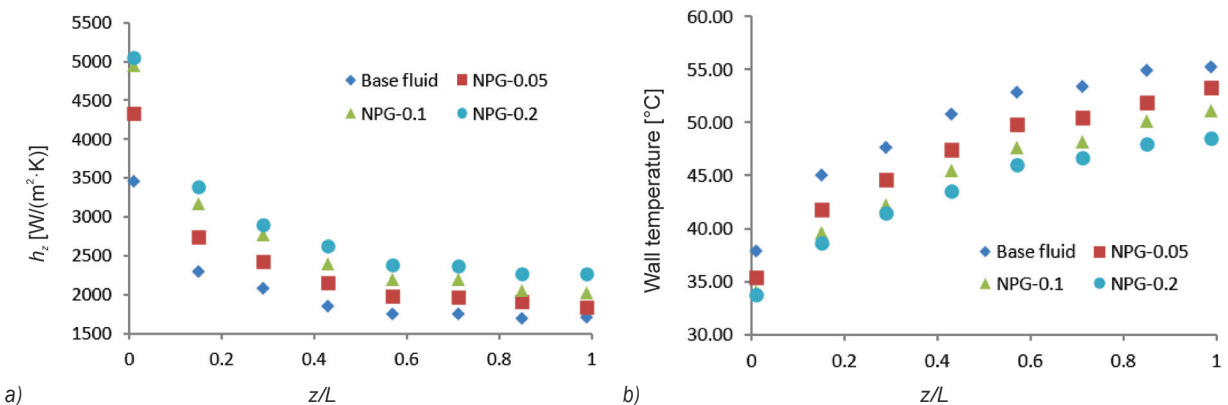


Fig. 6. a) The local heat transfer coefficient; b) wall temperature for different samples at Reynolds 4000

is observed at the wall, and the heat transfer rate is augmented there. There are also other factors including the collision of nanoparticles and probable slip velocity at boundaries, which may be the reason for the improvement of the heat transfer coefficient [41].

In contrast, as it is clear in Fig. 7, up to a concentration of 0.1 wt.%, this enhancement showed an almost a linear trend; however, after that, the rate of these changes with concentration was decreased. As the conductivity of the nanofluids is highly dependent on the stability of the particles in the base fluid, it seems that the decrease in the rate of enhancement is due to the deterioration of stability and reaches the threshold of nanoporous graphene deposition in the base fluid at higher concentrations [42].

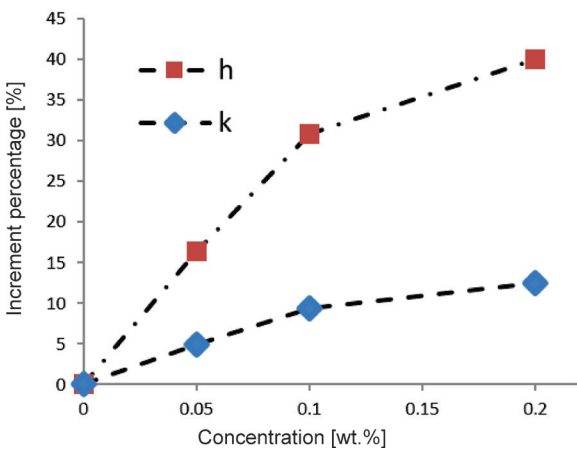


Fig. 7. Heat transfer coefficient and thermal conductivity increment with a concentration of nanoporous graphene

By maintaining the inlet temperature and wall heat flux constant, the above experiments were repeated for all samples at different Reynolds numbers. The

changes of local heat transfer coefficient and wall temperature in terms of dimensionless length for nanofluid with a concentration of 0.2 wt.% at different Reynolds numbers in the range of 4,000 to 11,500 are plotted in Fig. 8a. As expected, by increasing the Reynolds number, the local heat transfer coefficient was increased, and the relative wall temperature was decreased (Fig. 8b). The results indicate a 119 % increase of the average heat transfer coefficient and a 20.4 % decrease in average wall temperature while increasing the Reynolds number from 4,000 to 11,500.

The average heat transfer coefficient as a function of the Reynolds number for base fluid and different nanoparticle concentrations is presented in Fig. 9. It was also observed that using nanoporous graphene could lead to a significant increase in heat transfer coefficient in all Reynolds number ranges. This increase was almost independent of Reynolds number and on average was obtained to be 16.1 %, 30.3 %, and 39.4 % for the NPG-0.05, NPG-0.1, and NPG-0.2 samples, respectively. However, as explained previously, this rate of increase was reduced by increasing the concentration to higher levels. By increasing the Reynolds number, the heat transfer coefficients of all samples were increased roughly linearly.

Regarding the Nusselt number of the samples, a similar trend was again observed, the results of which are exhibited in Fig. 10. Using nanoporous graphene in concentration of 0.2 wt.%, augmented the Nusselt number by 19.2 % on average compared to that of the base solution. Most of this increase was up to concentration of 0.1 wt.% and, by doubling the nanoparticles content from 0.1 wt.% to 0.2 wt.%, only a negligible increase in Nusselt number was seen (less than 4 %).

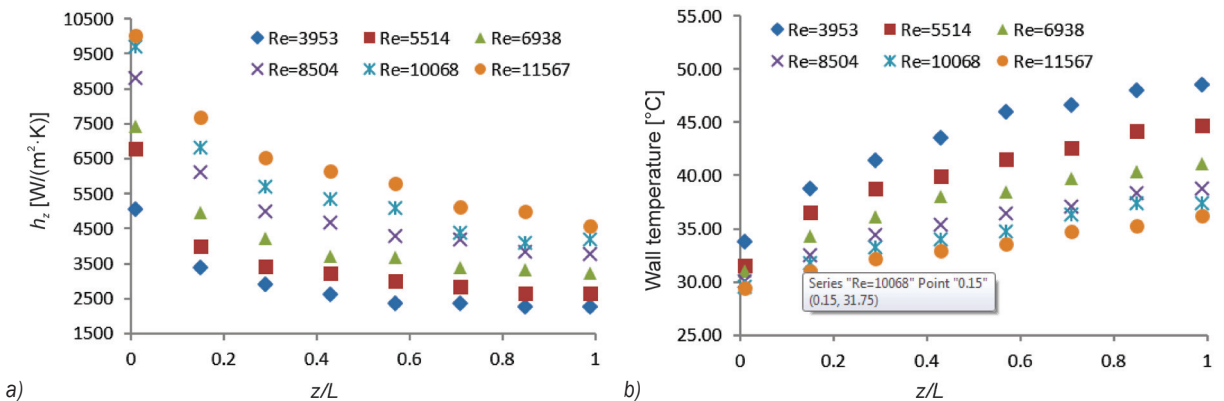


Fig. 8. a) The local heat transfer coefficient; b) wall temperature at different Reynolds numbers for NPG-0.2

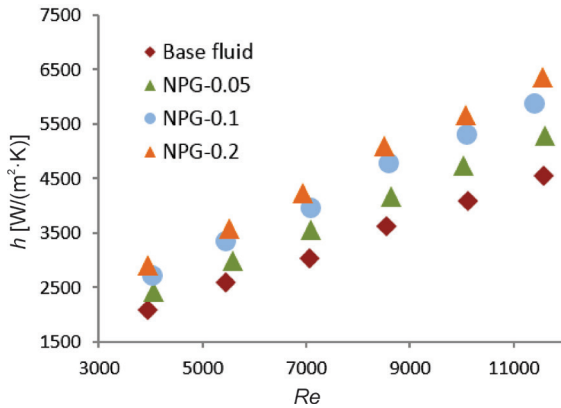


Fig. 9. Heat transfer coefficient of the samples at different Reynolds numbers

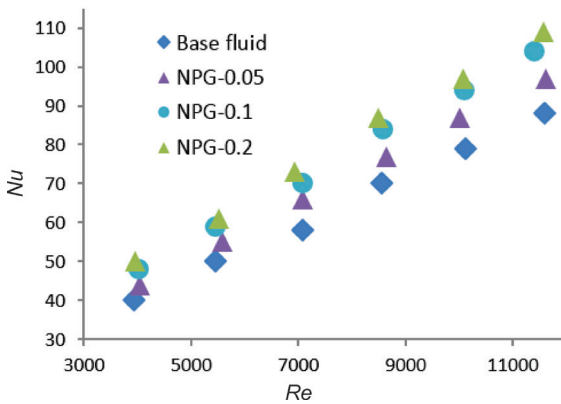


Fig. 10. Nusselt number of the samples at different Reynolds numbers

The pressure drop (ΔP) along the length of the test section for the base solution and the nanofluids was also investigated at all Reynolds numbers, and their results are presented in Table 3. As the measurements indicate, by increasing the Reynolds number and the nanoparticle concentration in the base solution, the pressure drop was increased.

Table 3. The pressure drop values of the samples in kPa at different Reynolds number

Reynolds number	4000	5500	7000	8500	10000	11500
Base fluid	0.52	0.83	1.20	1.63	2.13	2.70
NPG-0.05	0.62	0.93	1.41	1.80	2.27	2.87
NPG-0.1	0.67	1.00	1.46	1.97	2.49	2.94
NPG-0.2	0.91	1.35	1.93	2.66	3.23	4.02

By taking into account both heat transfer performance and flow resistance characteristics, to assess the performance of the heat exchanger, the thermal performance factor (TPF) can be employed, which is obtained through Eq. (9) [43]:

$$TPF = \frac{Nu_{nf}}{Nu_{bf}} \cdot \left(\frac{f_{nf}}{f_{bf}} \right)^{-1/3}, \tag{9}$$

where, “*nf*” and “*bf*” refer to the nanofluid and base fluid, respectively. Moreover, considering flow velocity (U) and the pressure drop (ΔP), the friction factor (f) can be calculated through Eq. (10):

$$f = \frac{\Delta P}{\frac{1}{2} \rho U^2 \left(\frac{L}{D_h} \right)}. \tag{10}$$

It can be stated that the TPF values that are higher than 1 contribute to improved integrative performance of the nanofluid compared to the base fluid; so, higher values of TPF are preferable. Fig. 11 depicts the variation trend of TPF values as a function of the Reynolds number. From this figure, it is clear that the TPF values of all the nanofluid samples with different concentrations of nanoparticles were higher than 1.

In comparison to the base fluid, the overall performance of all samples including *NPG-0.05*, *NPG-0.1*, and *NPG-0.2*, on average was enhanced by about 8.7 %, 16.7 %, and 14.2 %, respectively. It should be noted that increasing the concentration of nanoporous graphene nanoparticles from 0.1 wt.% to 0.2 wt.% did not increase the overall thermal performance; furthermore, regarding the induced pressure drop in the system, this increase in concentration decreased the overall thermal performance. Consequently, in the preparation of nanoporous graphene nanofluids, the optimum concentration is 0.1 wt.%, which can be employed in further studies.

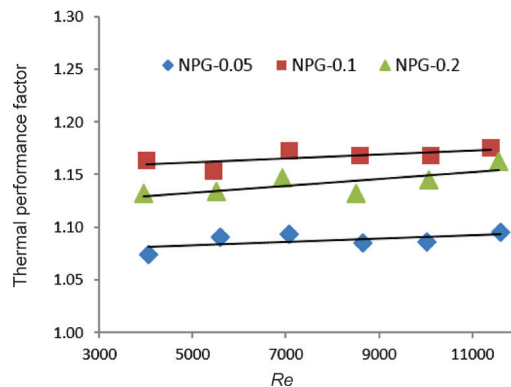


Fig. 11. Thermal performance factor vs Reynolds number for the prepared nanofluids

4 CONCLUSION

In this research work, nanoporous graphene nanoparticles were used to prepare nanofluids with enhanced thermal performance. The results obtained from using these non-Newtonian nanofluids flowing through a horizontal annular tube are presented. The boundary condition was set as “constant heat flux at the inner wall with the outer wall insulated”. To prepare the nanofluids, different concentrations of nanoporous graphene including 0.05 wt.%, 0.1 wt.%, and 0.2 wt.% were dispersed in aqueous solution of CMC. The nanofluids which were formed by using 0.2 wt.% CMC as surfactant and using ultrasonic system for 4 h, were of a good stability. The results revealed that addition of 0.05 wt.%, 0.1 wt.%, and 0.2 wt.% nanoporous graphene to the base solution increased the heat transfer coefficient by 16.1 %, 30.3 %, and 39.4 %, respectively, this improvement up to concentration of 0.1 wt.% was almost linear, after which rate of increase was appreciably lowered. Decrease in increase rate of the heat transfer coefficient at higher concentrations and also the effects of saturation, sedimentation, and increase in pressure drop of the non-Newtonian fluid led to the fact that doubling the concentration from 0.1 wt.% to 0.2 wt.% not only did not enhance the thermal performance but also decreased it by about 2.5 %. These measurements showed that in an annular tube, although at a given Reynolds number the heat transfer coefficient of the nanofluid with 0.2 wt.% nanoparticles in average is 9.1 % higher than that of the sample with 0.1 wt.% nanoparticles, considering the pressure drop and energy consumption, using the nanofluid of 0.1 wt.% is more preferable, which is the optimum content of nanoporous graphene in preparation of the nanofluid.

5 NOMENCLATURE

a	annular diameter ratio d_i/d_o ,
A	area, [m ²]
c_p	heat capacity, [J/(kg·K)]
d	diameter, [m]
D_h	hydraulic diameter, [m]
f	friction factor, [-]
F	a factor to take into account the dependence on d_i/d_o ,
h	heat transfer coefficient, [W/(m ² ·K)]
I	electrical current, [A]
k	thermal conductivity, [W/(m·K)]
K	a factor to take into account the temperature dependence of fluid properties, [-]
k_1	a factor, [-]

L	length of annular tube, [m]
m	flow consistency index, [-]
n	flow behavior index, [-]
Nu	Nusselt number, [-]
P	pressure, [Pa]
Pr	Prandtl number, [-]
q	heat transfer rate, [W]
q''	heat flux, [W/m ²]
Re	Reynolds number, [-]
Re^*	modified Reynolds number, [-]
T	temperature, [°C]
TPF	thermal performance factor, [-]
U	flow velocity, [m/s]
V	voltage, [V]
\dot{V}	volume flow rate, [m ³ /s]
X	each measured value,
z	z -axis,

Greek symbols:

ρ	density, [kg/m ³]
η	apparent viscosity, [Pa·s]
σ	uncertainty of measurement, [%]
Δ	difference, [-]
γ	shear rate, [1/s]

Subscripts:

ann	annulus
b	bulk
bf	base fluid
f	fluid
fi	fluid at entrance of test section
fo	fluid at exit of the test section
i	inner tube
mf	mean fluid
nf	nanofluid
i, o	inner tube, outer tube
w	wall
wi	wall of inner tube
z	axial position along the length of annular tube [m]

6 APPENDIX: UNCERTAINTY ANALYSIS

All values (X) which have been measured include uncertainty of measurement (δX) which can be given as follows:

$$X = X_{measured} \pm \delta X, \quad (11)$$

The accuracy of the instruments used for measuring in this study is given in Table 4.

Table 4. The accuracy of the instruments

Instrument	Variable	Accuracy
Calipers	d_p, d_o, D_h	± 0.0001 m
Densitometer	ρ	± 0.1 [kg/m ³]
KD2 Pro	k	± 5 %
K-type Thermocouples	T_{wi}, T_f	± 0.1 °C
Meter	L	± 0.001 m
Pressure transmitter	ΔP	± 2 %
Variac	V	± 1 V
Variac	I	± 0.1 A
Vortex flow meter	\dot{V}	± 2 %

To calculate the uncertainty of a dependent parameter $\varphi = f(X_1, \dots, X_j)$, the Kline and McClintock model through the root sum square method has been employed [21]:

$$\delta\varphi = \sqrt{\sum_{i=1}^j \left(\frac{\partial\varphi}{\partial X_i} \delta X_i \right)^2} \quad (12)$$

In this regard, for the Nusselt number we have:

$$\frac{\delta Nu}{Nu} = \left[\left(\frac{\delta h}{h} \right)^2 + \left(\frac{\delta D_h}{D_h} \right)^2 + \left(\frac{\delta k}{k} \right)^2 \right]^{\frac{1}{2}} \quad (13)$$

where:

$$\frac{\delta h}{h} = \left[\left(\frac{\delta V}{V} \right)^2 + \left(\frac{\delta I}{I} \right)^2 + \left(\frac{\delta d_i}{d_i} \right)^2 + \left(\frac{\delta L}{L} \right)^2 + \left(\frac{\delta T_{wi}}{T_{wi} - T_f} \right)^2 + \left(\frac{\delta T_f}{T_{wi} - T_f} \right)^2 \right]^{\frac{1}{2}} \quad (14)$$

and for the friction factor is as follows:

$$\frac{\delta f}{f} = \left[\left(\frac{\delta \Delta p}{\Delta p} \right)^2 + \left(\frac{\delta D_h}{D_h} \right)^2 + \left(\frac{\delta \rho}{\rho} \right)^2 + \left(\frac{\delta L}{L} \right)^2 + \left(\frac{2\delta U}{U} \right)^2 \right]^{\frac{1}{2}} \quad (15)$$

where:

$$\frac{\delta U}{U} = \left[\left(\frac{\delta \dot{V}}{\dot{V}} \right)^2 + \left(\frac{2d_o \delta d_o}{d_o^2 - d_i^2} \right)^2 + \left(\frac{2d_i \delta d_i}{d_o^2 - d_i^2} \right)^2 \right]^{\frac{1}{2}} \quad (16)$$

The maximum uncertainties of heat transfer coefficient (h), Nusselt number (Nu) and friction factor (f) were calculated as 2.3 %, 5.5 % and 3.1 %, respectively.

7 REFERENCES

[1] Moreira, T.A., Moreira, D.C., Ribatski, G. (2018). Nanofluids for heat transfer applications: a review. *Journal of the Brazilian Society of Mechanical Sciences and Engineering*, vol. 40, no. 303, DOI:10.1007/s40430-018-1225-2.

[2] Pinto, R.V., Fiorelli, F.A.S. (2016). Review of the mechanisms responsible for heat transfer enhancement using nanofluids. *Applied Thermal Engineering*, vol. 108, p. 720-739, DOI:10.1016/j.applthermaleng.2016.07.147.

[3] Öztürk, A., Kahveci, K. (2016). Slip flow of nanofluids between parallel plates heated with a constant heat flux. *Strojniški vestnik - Journal of Mechanical Engineering*, vol. 62, no. 9, p. 511-520, DOI:10.5545/sv-jme.2016.3188.

[4] Keblinski, P., Eastman, J.A., Cahill, D.G. (2005). Nanofluids for thermal transport. *Materials today*, vol. 8, no. 6, p. 36-44, DOI:10.1016/S1369-7021(05)70936-6.

[5] Heris, S.Z., Esfahany, M.N., Etemad, S.G. (2007). Experimental investigation of convective heat transfer of Al₂O₃/water nanofluid in circular tube. *International Journal of Heat and Fluid Flow*, vol. 28, no. 2, p. 203-210, DOI:10.1016/j.ijheatfluidflow.2006.05.001.

[6] Patel, H.E., Das, S.K., Sundararajan, T., Sreekumaran Nair, A., George, B., Pradeep, T. (2003). Thermal conductivities of naked and monolayer protected metal nanoparticle based nanofluids: Manifestation of anomalous enhancement and chemical effects. *Applied Physics Letters*, vol. 83, no. 14, p. 2931-2933, DOI:10.1063/1.1602578.

[7] Zarringhalam, M., Karimipour, A., Toghraie, D. (2016). Experimental study of the effect of solid volume fraction and Reynolds number on heat transfer coefficient and pressure drop of CuO-water nanofluid. *Experimental Thermal and Fluid Science*, vol. 76, p. 342-351, DOI:10.1016/j.expthermflusci.2016.03.026.

[8] Kakaç, S., Pramuanjaroenkij, A. (2009). Review of convective heat transfer enhancement with nanofluids. *International Journal of Heat and Mass Transfer*, vol. 52, no. 13-14, p. 3187-3196, DOI:10.1016/j.ijheatmasstransfer.2009.02.006.

[9] Sidik, N.A.C., Mohammed, H.A., Alawi, O.A., Samion, S. (2014). A review on preparation methods and challenges of nanofluids. *International Communications in Heat and Mass Transfer*, vol. 54, p. 115-125, DOI:10.1016/j.icheatmasstransfer.2014.03.002.

[10] Raja, M., Vijayan, R., Dineshkumar, P., Venkatesan, M. (2016). Review on nanofluids characterization, heat transfer characteristics and applications. *Renewable and Sustainable Energy Reviews*, vol. 64, p. 163-173, DOI:10.1016/j.rser.2016.05.079.

[11] Taamneh, Y., Bataineh, K. (2017). Mixed convection heat transfer in a square lid-driven cavity filled with Al₂O₃-water nanofluid. *Strojniški vestnik - Journal of Mechanical Engineering*, vol. 63, no. 6, p. 383-393, DOI:10.5545/sv-jme.2017.4449.

[12] Al-Kouz, W.G., Kiwan, S., Alkhalidi, A., Sari, M., Alshare, A. (2018). Numerical study of heat transfer enhancement for low-pressure flows in a square cavity with two fins attached to the hot wall using Al₂O₃-air nanofluid. *Strojniški vestnik -*

- Journal of Mechanical Engineering*, vol. 64, no. 1, p. 26-36, DOI:10.5545/sv-jme.2017.4989.
- [13] Vahidinia, F., Miri, M. (2015). Numerical study of the effect of the Reynolds numbers on thermal and hydrodynamic parameters of turbulent flow mixed convection heat transfer in an inclined tube. *Strojniški vestnik - Journal of Mechanical Engineering*, vol. 61, no. 11, p. 669-679, DOI:10.5545/sv-jme.2015.2818.
- [14] Mishra, R., Miliaty, J. (2019). Carbon-based nanomaterials. *Nanotechnology in Textiles*, vol. 2019, p. 163-179, DOI:10.1016/B978-0-08-102609-0.00003-1.
- [15] Teng, T.-P., Hsiao, T.-C., Chung, C.-C. (2019). Characteristics of carbon-based nanofluids and their application in a brazed plate heat exchanger under laminar flow. *Applied Thermal Engineering*, vol. 146, p. 160-168, DOI:10.1016/j.applthermaleng.2018.09.125.
- [16] Amrollahi, A., Rashidi, A.M., Lotfi, R., Meibodi, M.E., Kashefi, K. (2010). Convection heat transfer of functionalized MWNT in aqueous fluids in laminar and turbulent flow at the entrance region. *International Communications in Heat and Mass Transfer*, vol. 37, no. 6, p. 717-723, DOI:10.1016/j.icheatmasstransfer.2010.03.003.
- [17] Naghash, A., Sattari, S., Rashidi, A. (2016). Experimental assessment of convective heat transfer coefficient enhancement of nanofluids prepared from high surface area nanoporous graphene. *International Communications in Heat and Mass Transfer*, vol. 78, p. 127-134, DOI:10.1016/j.icheatmasstransfer.2016.09.004.
- [18] Amiri, A., Arzani, H.K., Kazi, S.N., Chew, B.T., Badarudin, A. (2016). Backward-facing step heat transfer of the turbulent regime for functionalized graphene nanoplatelets based water-ethylene glycol nanofluids. *International Journal of Heat and Mass Transfer*, vol. 97, p. 538-546, DOI:10.1016/j.ijheatmasstransfer.2016.02.042.
- [19] Askari, S., Lotfi, R., Seifkordi, A., Rashidi, A. M., Koolivand, H. (2016). A novel approach for energy and water conservation in wet cooling towers by using MWNTs and nanoporous graphene nanofluids. *Energy Conversion and Management*, vol. 109, p. 10-18, DOI:10.1016/j.enconman.2015.11.053.
- [20] Ranjbarzadeh, R., Karimipour, A., Afrand, M., Isfahani, A.H.M., Shirmeshan, A. (2017). Empirical analysis of heat transfer and friction factor of water/graphene oxide nanofluid flow in turbulent regime through an isothermal pipe. *Applied Thermal Engineering*, vol. 126, p. 538-547, DOI:10.1016/j.applthermaleng.2017.07.189.
- [21] Taheran, E., Javaherdeh, K. (2019). Experimental investigation on the effect of inlet swirl generator on heat transfer and pressure drop of non-Newtonian nanofluid. *Applied Thermal Engineering*, vol. 147, p. 551-561, DOI:10.1016/j.applthermaleng.2018.07.12.
- [22] Behroyan, I., Vanaki, Sh. M., Ganesan, P., Saidur, R. (2016). A comprehensive comparison of various CFD models for convective heat transfer of Al₂O₃ nanofluid inside a heated tube. *International Communications in Heat and Mass Transfer*, vol. 70, p. 27-37, DOI:10.1016/j.icheatmasstransfer.2015.11.001.
- [23] Hojjat, M., Etemad, S.Gh., Bagheri, R., Thibault, J. (2011). Rheological characteristics of non-Newtonian nanofluids: experimental investigation. *International Communications in Heat and Mass Transfer*, vol. 38, no. 2, p. 144-148, DOI:10.1016/j.icheatmasstransfer.2010.11.019.
- [24] Kole, M., Dey, T.K. (2011). Effect of aggregation on the viscosity of copper oxide-gear oil nanofluids. *International Journal of Thermal Sciences*, vol. 50, no. 9, p. 1741-1747, DOI:10.1016/j.ijthermalsci.2011.03.027.
- [25] Togun, H., Abdulrazzaq, T., Kazi, S.N., Badarudin, A., Kadhum, A.A.H., Sadeghinezhad, E. (2014). A review of studies on forced, natural and mixed heat transfer to fluid and nanofluid flow in an annular passage. *Renewable and Sustainable Energy Reviews*, vol. 39, p. 835-856, DOI:10.1016/j.rser.2014.07.008.
- [26] Bahiraei, M., Khosravi, R., Heshmatian, S. (2017). Assessment and optimization of hydrothermal characteristics for a non-Newtonian nanofluid flow within miniaturized concentric-tube heat exchanger considering designer's viewpoint. *Applied Thermal Engineering*, vol. 123, p. 266-276, DOI:10.1016/j.applthermaleng.2017.05.090.
- [27] Latifa, E.-K., Asbik, M., Zari, N., Zeghamati, B. (2017). Experimental study of the sensible heat storage in the water/TiO₂ nanofluid enclosed in an annular space. *Applied Thermal Engineering*, vol. 122, p. 673-684, DOI:10.1016/j.applthermaleng.2017.05.054.
- [28] Arzani, H.K., Amiri, A., Kazi, S.N., Chew, B.T., Badarudin, A. (2016). Experimental investigation of thermophysical properties and heat transfer rate of covalently functionalized MWCNT in an annular heat exchanger. *International Communications in Heat and Mass Transfer*, vol. 75, no. 67-77, DOI:10.1016/j.icheatmasstransfer.2016.03.015.
- [29] Arzani, H.K., Amiri, A., Kazi, S.N., Chew, B.T., Badarudin, A. (2015). Experimental and numerical investigation of thermophysical properties, heat transfer and pressure drop of covalent and noncovalent functionalized graphene nanoplatelet-based water nanofluids in an annular heat exchanger. *International Communications in Heat and Mass Transfer*, vol. 68, p. 267-275, DOI:10.1016/j.icheatmasstransfer.2015.09.007.
- [30] Pourmand, S., Abdouss, M., Rashidi, A. (2015). Fabrication of nanoporous graphene by chemical vapor deposition (CVD) and its application in oil spill removal as a recyclable nanosorbent. *Journal of Industrial and Engineering Chemistry*, vol. 22, p. 8-18, DOI:10.1016/j.jiec.2014.06.018.
- [31] Hojjat, M., Etemad, S.G., Bagheri, R., Thibault, J. (2009). Rheological behavior of non-Newtonian nanofluids. *The 6th International Chemical Engineering Congress & Exhibition*.
- [32] Li, M. (2013). A nano-graphite/paraffin phase change material with high thermal conductivity. *Applied Energy*, vol. 106, p. 25-30, DOI:10.1016/j.apenergy.2013.01.031.
- [33] Estellé, P., Halelfadl, S., Maré, T. (2015). Thermal conductivity of CNT water based nanofluids: *Experimental trends and models overview*. *Journal of Thermal Engineering*, vol. 1, no. 2, p. 381-390, DOI:10.13140/2.1.2173.9843.
- [34] Kutz, M. (2006). *Heat Transfer Calculations*. McGraw-Hill, New York.
- [35] Crespí-Llorens, D., Vicente, P., Viedma, A. (2015). Generalized Reynolds number and viscosity definitions for non-Newtonian fluid flow in ducts of non-uniform cross-section.

- Experimental Thermal and Fluid Science*, vol. 64, p. 125-133, DOI:10.1016/j.expthermflusci.2015.02.005.
- [36] Gnielinski, V. (2009). Heat transfer coefficients for turbulent flow in concentric annular ducts. *Heat Transfer Engineering*, vol. 30, p. 6, no. 431-436, DOI:10.1080/01457630802528661.
- [37] Gnielinski, V. (2015). Turbulent heat transfer in annular spaces—a new comprehensive correlation. *Heat Transfer Engineering*, vol. 36, no. 9, p. 787-789, DOI:10.1080/01457632.2015.962953.
- [38] Bergman, T.L, Lavine, A.S., Incropera, F.P., Dewitt, D.P. (2011). *Fundamentals of Heat and Mass Transfer*, 7th ed. *Thermophysical Properties of Matter*, Appendix A, p. 1003, John Wiley & Sons, Hoboken.
- [39] Anoop, K.B., Sundararajan, T., Das, S.K. (2009). Effect of particle size on the convective heat transfer in nanofluid in the developing region. *International Journal of Heat and Mass Transfer*, vol. 52, no. 9-10, p. 2189-2195, DOI:10.1016/j.ijheatmasstransfer.2007.11.063.
- [40] Xuan, Y., Li, Q. (2003). Investigation on convective heat transfer and flow features of nanofluids. *Journal of Heat Transfer*, vol. 125, no. 1, p. 151-155, DOI:10.1115/1.1532008.
- [41] Hojjat, M., Etemad, S.G., Bagheri, R., Thibault, J. (2011). Convective heat transfer of non-Newtonian nanofluids through a uniformly heated circular tube. *International Journal of Thermal Sciences*, vol. 50, no. 4, p. 525-531, DOI:10.1016/j.ijthermalsci.2010.11.006.
- [42] Ghoozatloo, A., Rashidi, A., Shariaty-Niassar, M. (2014). Convective heat transfer enhancement of graphene nanofluids in shell and tube heat exchanger. *Experimental Thermal and Fluid Science*, vol. 53, p. 136-141, DOI:10.1016/j.expthermflusci.2013.11.018.
- [43] Maradiya, C., Vadher, J., Agarwal, R. (2018). The heat transfer enhancement techniques and their thermal performance factor. *Beni-Suef University Journal of Basic and Applied Sciences*, vol. 7, no. 1, p. 1-21, DOI:10.1016/j.bjbas.2017.10.001.

Double-layer Control of an Automatic Mechanical Transmission Clutch during Commercial Vehicle Start-up

Min Song¹ – Hongliang Wang^{1,*} – Haiou Liu² – Pai Peng¹ –
Xianhui Wang¹ – Dawei Pi¹ – Chen Yang¹ – Gang He¹

¹ Nanjing University of Science & Technology, Department of Mechanical Engineering, China

² School of Mechanical and Vehicular Engineering, Beijing Institute of Technology, China

Engagement control of an automatic mechanical transmission clutch during vehicle start-up has important influences on the safety, comfort, service life, energy consumption, and emissions of the vehicle. However, all existing control strategies use single-layer control, which leads to poor temperature adaptability. This paper develops a double-layer control strategy based on an automatic actuator to improve vehicle start-up performance. The governing characteristics of a diesel engine with a variable-speed governor are studied. The working principles and a model of the automatic actuator are described. A simulation of vehicle start-up is constructed and tested. Finally, the double-layer control strategy is verified in an experimental vehicle. The experimental and simulation results show that the double-layer control strategy provides shorter start times, less jerking, and lower friction, thereby demonstrating its effectiveness and practicability.

Keywords: automatic mechanical transmission, start-up process, clutch engagement control, double-layer control

Highlights

- A double-layer control strategy is designed based on an automatic clutch actuator and controller.
- Temperature changes affect clutch engagement performance during the vehicle start-up process.
- Comparative outcomes verify the benefits of our scheme in terms of start time, jerking and friction work.
- Experiments with an actual vehicle further validate the proposed control strategy.

0 INTRODUCTION

An automatic mechanical transmission (AMT) is a type of automatic shifting control mechanism based on the original dried frictional flake's clutch and fixed-shaft geared manual transmission to realize the automatic operation of transmission selection and shifting [1]. An AMT has the advantages of both an automatic transmission (AT) and a manual transmission (MT) in terms of efficiency, cost, simplicity and ease of manufacture [2]. Moreover, AMTs also do not have the shortcomings of dual-clutch transmissions (DCTs), which have high failure rates and are unsuitable for use with small-displacement engines that produce insufficient torque at low speeds [3]. AMTs are considered inexpensive add-on solutions for conventional MTs. Therefore, in recent years, AMTs have been widely used in the automotive field, especially in commercial vehicles [4].

Because AMTs are modifications of fixed-shaft geared manual transmissions, they have disadvantages, such as poor smoothness, easy power interruption, etc. [5]. By optimizing the control of clutch engagement, it is possible to reduce clutch wear and energy loss, shorten the clutch engagement process, and reduce jerking and friction [6]. Control of the clutch engagement process in AMTs has a significant

impact on various performance characteristics of a vehicle, such as its start-up [7], fuel consumption [8], dynamics [9] and security [10]. This paper focuses on optimization of the clutch engagement control strategy during vehicle start-up.

Research on clutch modelling and control strategies in the start-up of AMT vehicles has been extensively studied [11]. During the vehicle start-up process, the single-layer clutch engagement control proposed in [12] is an optimal control approach that uses weighting factors for the slipping speed and control inputs to analyse clutch engagement. Huang et al. [13] used the acceleration pedal displacement and rate of change, the relative slip rates of the driving and driven plates, and changes in engine speed to represent the driving intention, clutch engagement state, and engine running state, respectively, in a dry DCT vehicle start-up fuzzy intelligent control algorithm. A combination of optimal control and an open-loop lookup table aiming to reduce slipping time and ensure engagement comfort was introduced in [14]. Bemporad et al. [15] proposed a novel piecewise linear feedback control strategy for an automotive dry clutch engagement process. Based on a dynamic model of the powertrain system, the controller was designed by minimizing a quadratic performance index subject to constraints on the inputs and on the states. Wang et al. [16] and [17] analysed the motion

*Corr. Author's Address: Department of Mechanical Engineering, Nanjing University of Science & Technology, Nanjing, Jiangsu, China, whl343@163.com

relationships between various parts of the vehicle driveline, designed a clutch automatic actuator based on a flow solenoid valve, studied the start-up process of the vehicle, and controlled it with reference to the model's method. Amari et al. [18] proposed a real-time model predictive control (MPC) for controlling the behaviour of an AMT. Van et al. [19] deduced the optimal engagement strategy under different driver intentions based on a linear quadratic regulator. Researchers [20] proposed a fuzzy logic controller for the smooth and rapid engagement of an automatic clutch. The described controller uses both fuzzy logic and slip control algorithms to enable automatic clutch engagement. van Berkel et al. [21] proposed a new controller design that segments the clutch engagement process and distinguishes the control laws at each stage.

Although there are many studies concerning AMT clutch control, they fail to take into account deviations between the actual clutch engagement speed and the target value of the control strategy due to changes in environmental temperature.

The primary objective of this article is to develop a double-layer control strategy for a commercial vehicle AMT clutch based on a gas-assisted automatic actuator during vehicle start-up. There are three crucial novel contributions of our study.

1. First, on the basis of a first-layer reference model control strategy, a second-layer control strategy is added to improve temperature adaptability.
2. Second, a co-simulation platform is established involving Matlab/Simulink and Trucksim to verify the effectiveness of the control strategy under different temperatures.
3. Finally, an experiment of actual vehicle start-up is carried out at different temperatures.

1 SYSTEM MODELLING

1.1 Modelling a Diesel Engine with a Variable-Speed Governor

The torque curves of diesel engines are relatively flat, and a small change in the external resistance moment will lead to a large rotation speed fluctuation [22]. The resistance moment of the vehicle changes greatly, which requires the driver to adjust the throttle frequently, which may lead to driver fatigue. A variable-speed governor can allow a diesel engine to make larger torque changes under small speed changes. This can handle changes in the resistance moment and reduce driver fatigue. This study used a test vehicle with a diesel engine, and variable-speed

governor, whose characteristic curves under different throttle openings are shown in Fig. 1 [23].

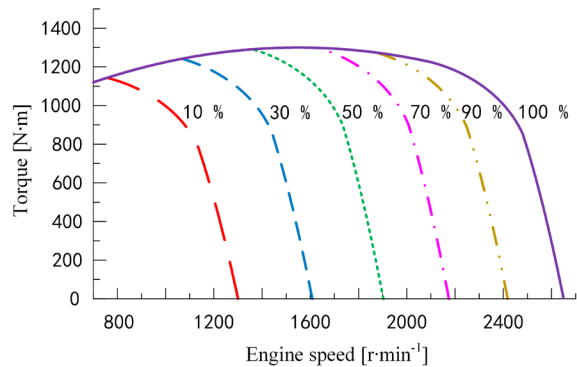


Fig. 1. Fixed throttle characteristics of a diesel engine with variable-speed governor

The variable-speed governor can maintain the engine speed within a certain range to prevent stalling or racing. Fig. 2 shows a characteristic torque curve of the diesel engine with the variable-speed governor at 30% throttle opening.

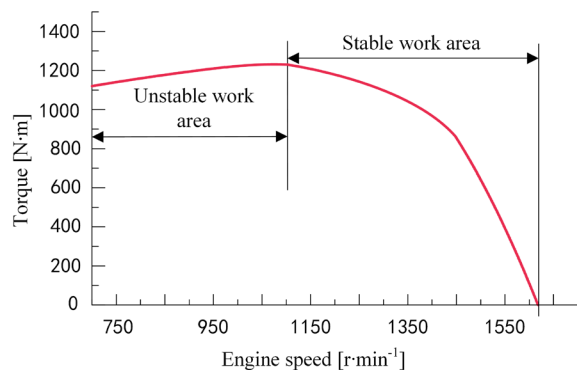


Fig. 2. Diesel engine speed-torque curve with 30% throttle opening

1.2 Vehicle Driveline Modelling

A simplified diagram of the test vehicle's powertrain is shown in Fig. 3 [24]. Without considering their torsional and transverse vibrations, each part is considered to be a rigid body. The clearance between kinematic pairs is ignored. Non-damped parts can be considered as the mass is concentrated on the centre of mass; except for the clutch, tire and synchronizer, the other kinematic pairs do not consider the influence of friction.

According to the characteristics and dynamic formula of the vehicle start-up process, the clutch engagement process can be roughly divided into three

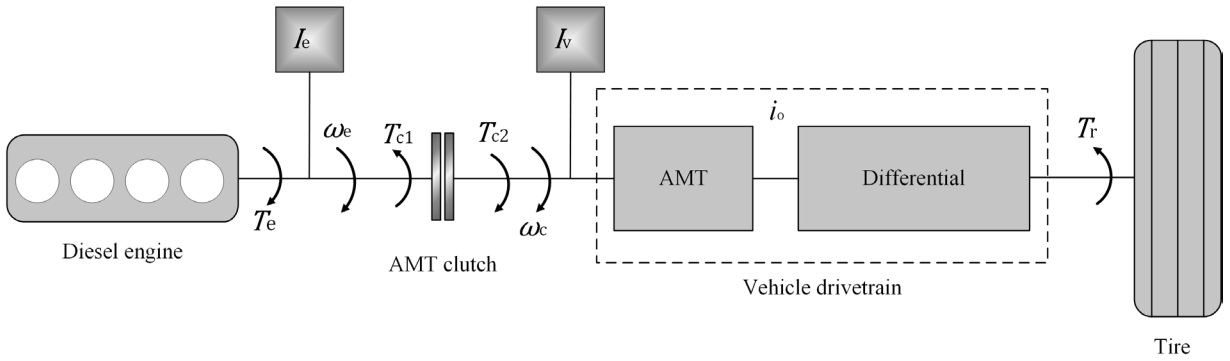


Fig. 3. Simplified model of the test vehicle's driveline

stages: clearance elimination, slip and friction, and synchronization [25].

The quantities equations of I_e and I_v are as follows:

$$\left. \begin{aligned} I_e &= I_1 + I_{c1} \\ I_v &= I_{c2} + I_t + I_d \end{aligned} \right\} \quad (1)$$

- (1) In the clearance elimination stage, at this time, the clutch-driven plate, transmission and tires are stationary, and the torque calculation formula of each part is as follows:

$$\left. \begin{aligned} T_e &= I_e \dot{\omega}_e \\ T_{c1} &= T_{c2} = 0 \\ T_r &= 0 \end{aligned} \right\} \quad (2)$$

- (2) In the slip and friction stage, the torques of each part are calculated by the formulas:

$$\left. \begin{aligned} T_e &= I_e \dot{\omega}_e + T_{c1} \\ T_{c1} &= \mu k_c F_c \\ T_{c2} &= I_v \dot{\omega}_c + i_o T_r \\ T_{c1} &= T_{c2} \end{aligned} \right\} \quad (3)$$

- (3) In the clutch synchronisation phase, the clutch driving plate speed and driven plate speed are the same. At this point, $\dot{\omega}_e$ and $\dot{\omega}_c$ are equal.

$$\left. \begin{aligned} T_e &= I_e \dot{\omega}_e + T_{c1} \\ \dot{\omega}_e &= \dot{\omega}_c \\ \omega_e &= \omega_c \end{aligned} \right\} \quad (4)$$

It can be obtained from Eq. (4) that:

$$\left. \begin{aligned} T_{c1} &= T_{c2} \\ T_{c2} &= I_v \dot{\omega}_c + i_o T_r \\ T_{c1} &= I_v \dot{\omega}_e + i_o T_r \end{aligned} \right\} \quad (5)$$

1.3 Clutch Modelling

A dry clutch relies on friction to transfer torque. The formula for calculating the transfer torque of a dry clutch [26] is:

$$T_c = \mu(T, \Delta\omega) F_c Z \times \frac{2}{3} \left(\frac{R_1^3 - R_0^3}{R_1^2 - R_0^2} \right) \quad (6)$$

The dynamic friction factor $\mu(T, \Delta\omega)$ is affected by the clutch plate temperature T and $\Delta\omega$. A simplified representation of the relationship between the clutch's engagement position and its output torque is shown in Fig. 4, ignoring changes in temperature, clutch friction plate wear and dynamic friction factors.

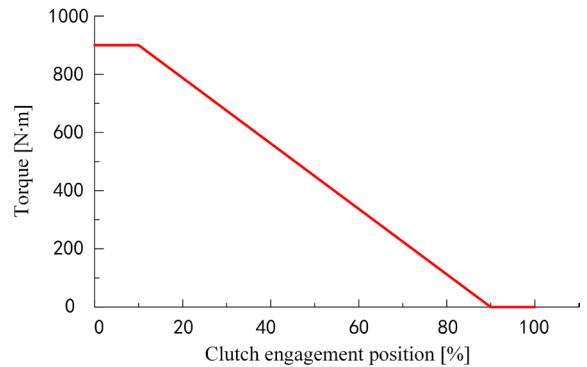


Fig. 4. Relationship between clutch output torque and clutch engagement position

1.4 Automatic Actuator Modelling

A gas-assisted hydraulic clutch actuator [27] is shown in Fig. 5. A hydraulic control cylinder is connected to the clutch pedal to control the hydraulic master cylinder [28]. Fig. 6 is a schematic diagram of the

gas-assisted hydraulic automatic clutch actuator. The relationship between the motions of the parts of the automatic clutch actuator can be simplified, as shown in Fig. 7.

The formula for calculating the gas-assisted hydraulic working cylinder piston movement speed v_3 is:

$$v_3 = \frac{S_2 k}{S_1 S_3} q_1 \quad (7)$$

The formula for the clutch displacement L is:

$$L = \int v_3 dt = \int \frac{S_2 k}{S_1 S_3} q_1 dt = \frac{S_2 k}{S_1 S_3} V_1 \quad (8)$$

Therefore, the flow and volume of oil in the hydraulic control cylinder can be controlled via the proportional flow valve, so as to control the speed and displacement of the clutch [29].

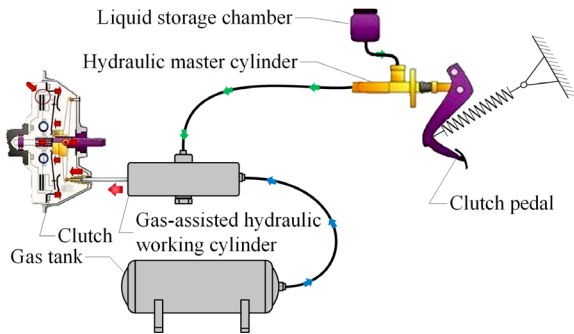


Fig. 5. Gas-assisted hydraulic clutch actuator

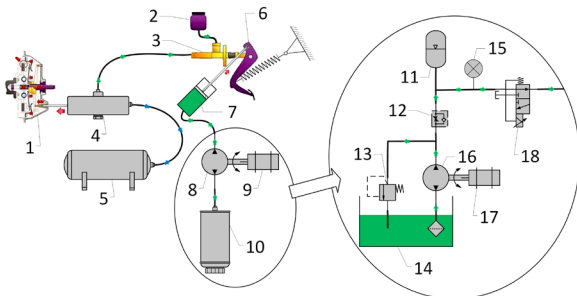


Fig. 6. Gas-assisted hydraulic automatic clutch actuator: 1) clutch, 2) liquid storage chamber, 3) hydraulic master cylinder, 4) gas-assisted hydraulic working cylinder, 5) gas tank, 6) clutch pedal, 7) hydraulic control cylinder, 8) oil pump, 9) electric motor, 10) oil tank, 11) accumulator, 12) one-way throttle, 13) overflow valve, 14) oil tank, 15) pressure gauge, 16) oil pump, 17) electric motor, and 18) proportional flow valve

When the proportional flow valve works, its resistance can be considered constant, so the current can be controlled by adjusting the voltage [30]. The voltage of the proportional flow valve is controlled by

the duty ratio of pulse width modulation (PWM). The basic working characteristics of the proportional flow valve at a normal temperature of 25 °C are shown in Fig. 8.

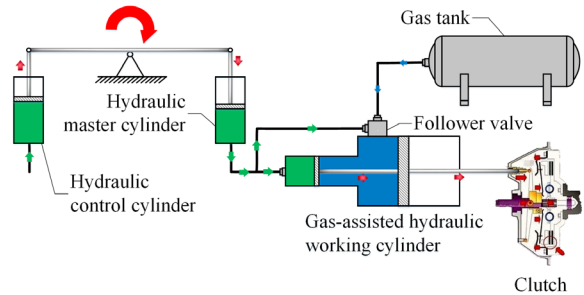


Fig. 7. Action of the automatic clutch actuator

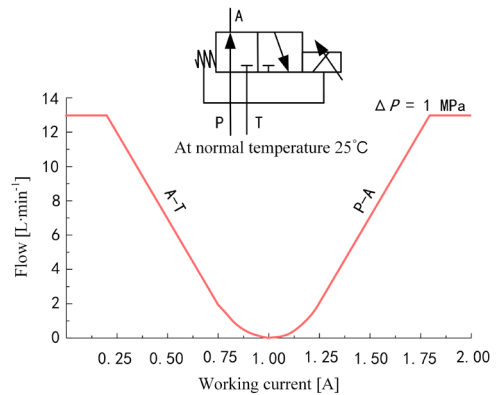


Fig. 8. Basic working characteristics of the proportional flow valve

The clutch engagement process under different duty ratios is shown in Fig. 9.

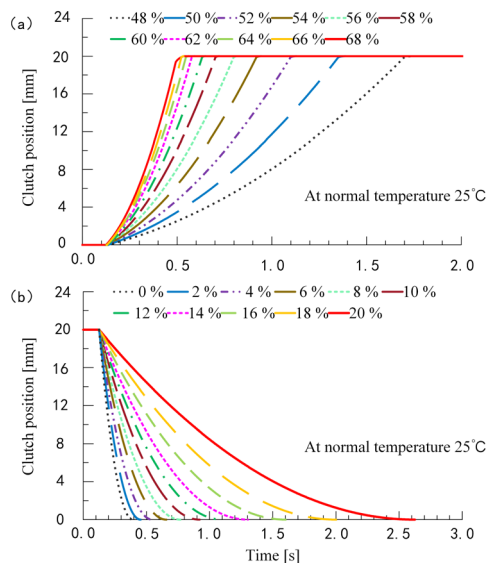


Fig. 9. Curves of a) clutch separation, and b) clutch engagement

2 EVALUATION INDEX

At present, the start time, jerking, and friction work are generally used as evaluation indexes for the quantitative evaluation of the vehicle start-up process [31]. Jerking is the first derivative of the longitudinal acceleration of a vehicle in the start-up process, which is used as a quantitative index to reflect the comfort level of passengers and drivers [32].

$$j = \frac{da}{dt} = \frac{d^2u}{dt^2}, \quad (9)$$

$$F_t = F_j + F_f + F_i + F_w, \quad (10)$$

$$F_t = \frac{T_{c2} i_g i_0 \eta}{r}, \quad (11)$$

$$F_j = \delta M \frac{du}{dt}. \quad (12)$$

The formula for jerking can be expressed as:

$$j = \frac{da}{dt} = \frac{d^2u}{dt^2} = \frac{1}{\delta M} \frac{i_g i_0 \eta}{r} \frac{dT_c}{dt}. \quad (13)$$

It can be seen from Eq. (13) that jerking is proportional to the rate of change of the friction torque of the clutch. Decreasing the rate of change reduces jerking.

Friction work refers to the amount of work done by friction torque in the process of clutch engagement. The amount of friction work will affect the transmission efficiency of the vehicle driveline and the temperature of the clutch friction plate. It also reflects clutch friction plate wear and affects service life [33].

$$W = \int_{t_1}^{t_2} T_{c2}(t) \omega_e(t) dt + \int_{t_2}^{t_3} T_{c2}(t) [\omega_e(t) - \omega_c(t)] dt. \quad (14)$$

It can be concluded that control of the duty ratio of the flow solenoid valve is used to control the speed of clutch engagement, the clutch output torque and, ultimately, the friction work and jerking.

3 CONTROL STRATEGY

3.1 Process Analysis

In all of the control stages of a vehicle start-up process, clutch engagement control is crucial [34]. According to Section 1.2, the start-up process is subdivided into five parts [35], as shown in Fig. 10.

Phase 1: the clutch driving and driven plates are not in contact. Phase 2: there is contact friction as the driving plate is rotating, but the driven plate is

still. Phase 3: the clutch driven plate starts to rotate. Phase 4: the clutch driving and driven plate speeds differ between the critical value and 0. Phase 5: the rotating speeds are consistent until the end of clutch engagement.

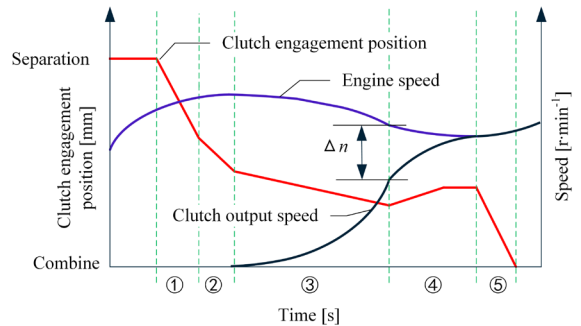


Fig. 10. Control curve of a vehicle start-up process

3.2 Double-Layer Control Strategy

In order to improve the control accuracy, reliability and robustness of the control system, a double-layer control method is proposed. The first layer uses a reference model control [25]. However, due to changes in ambient temperature and other factors, there is a deviation between the actual clutch engagement speed and the target clutch engagement speed. Therefore, proportion integration differentiation (PID) control is adopted as the second layer of control to improve the control accuracy, reliability and robustness of the system. Its schematic diagram is shown in Fig. 11.

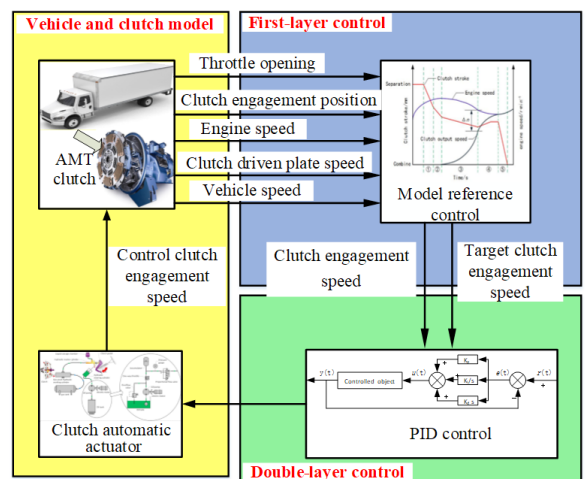


Fig. 11. Double-layer clutch control strategy

Some key signals are transmitted to the first-layer control via the vehicle and clutch model, including the amount of throttle opening, clutch engagement

position, engine speed, clutch driven plate speed and vehicle speed. The clutch engagement position is obtained by a displacement sensor installed on the clutch. After the signals are calculated in the first layer, the target clutch engagement speed and the derivative of the clutch engagement position (clutch engagement speed) are transmitted to the second-layer control (PID control). Here, the target clutch engagement speed serves as a given value and the clutch engagement speed serves as feedback, with the clutch and its automatic actuator being the controlled objects. The PID control parameters are set as $K_p = 0.05$, $K_{ip} = 27.6$ and $K_{dp} = 0.01$.

4 SIMULATION ANALYSIS

Trucksim and the Matlab/Simulink co-simulation platform were used to establish a model of the vehicle start-up process in order to evaluate the effects of the double-layer control strategy. The parameters of the experimental vehicle adopted in the simulation model are shown in Table 1.

Table 1. Main parameters of the experimental vehicle

Parameter	Value
m	8190 kg
r	397 mm
i_0	30.786
η	0.99

In this paper, only a typical 30 % throttle opening vehicle start-up process is considered, because it is representative. The simulation results are shown in Figs. 12 and 13. The start time, the root mean square (RMS) of jerking, and the friction work of the single-layer control strategy at low temperature are 28.3 % longer, 19.8 % lower and 8.0 % greater, respectively, than at normal temperature. This demonstrates that temperature changes have a great effect on the performance of single-layer controlled clutch engagement during the vehicle start-up process.

Compared with the simulation results for the double-layer control strategy at normal and low temperatures, the start time, RMS jerking and friction work of the single-layer control strategy at low temperature are 5.7 % longer, 7.4 % lower and 6.6 % more, respectively, than at normal temperature. This demonstrates that the double-layer control strategy can increase the performance degradation caused by temperature reduction.

As can be seen from Fig. 13, compared with the single-layer control strategy, the start time with the

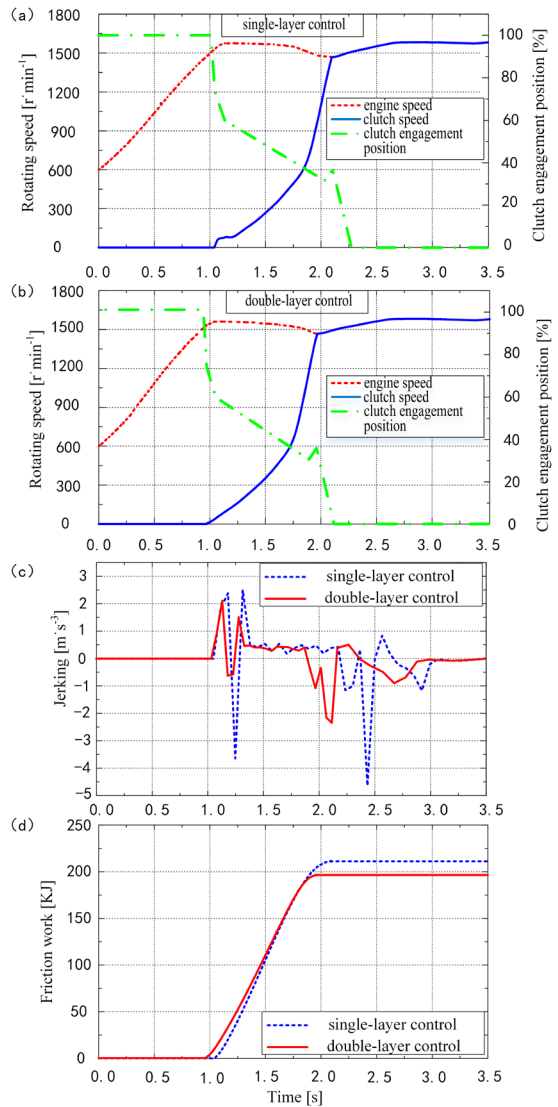


Fig. 12. Simulation results at normal temperature (25 °C), a) single-layer control, b) double-layer control, c) jerking contrast, and d) friction work contrast

Table 2. Comparison of simulation results (*RMS value)

Temperature	Control strategy	Start time [s]	*Start-up jerking [-]	Friction work [kJ]
Normal (25 °C)	Single layer	1.27	1.06	212
	Double layer	1.20	0.73	196
Low (-10 °C)	Single layer	1.63	0.85	229
	Double layer	1.29	0.68	209

double-layer control strategy is 5.8 % shorter, the RMS of jerking is 31.1 % lower, and the friction work is reduced by 7.5 %. As shown in Fig. 14, the start time, the RMS of jerking and the friction work of the

double-layer control strategy are reduced by 20.8 %, 20.0 % and 8.7 %, respectively. Compared with the single-layer control strategy, the double-layer control strategy reduces the start time, friction work and start-up jerking. The performance of the vehicle's start-up process has been significantly improved.

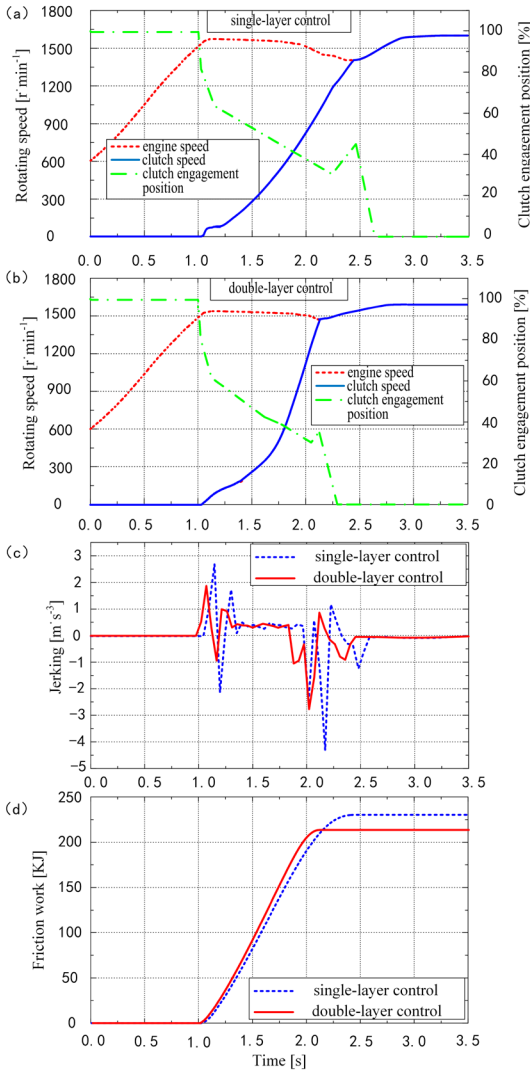


Fig. 13. Simulation results at low temperature (-10 °C), a) single-layer control, b) double-layer control, c) jerking contrast, and d) friction work contrast

5 EXPERIMENTAL RESEARCH

On the basis of an automatic clutch actuator, a double-layer clutch control strategy for a vehicle start-up process was designed. The controller and control strategy were verified on a test vehicle. Fig. 14 shows the experimental vehicle and relevant components. Under normal temperature (25 °C; Fig. 15) and low-

temperature conditions (-10 °C; Fig. 16), a constant 30 % throttle opening was adopted for a test vehicle driven on a flat, horizontal road surface.

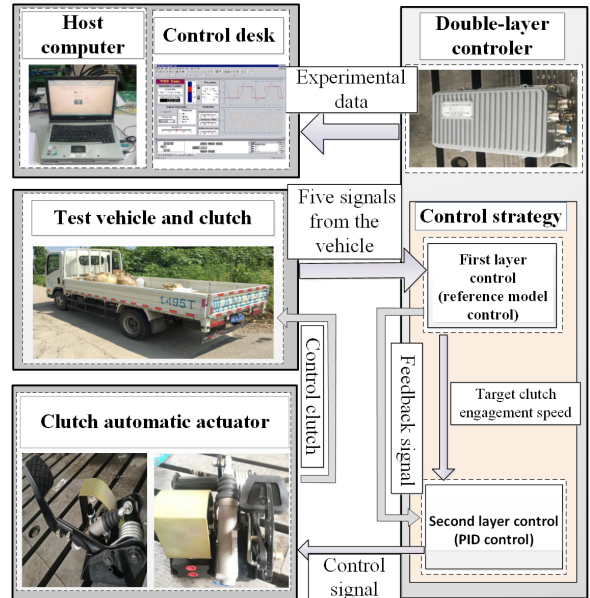


Fig. 14. Experimental setup

As can be seen from Fig. 15, at normal temperature, compared with the single-layer control strategy, the double-layer control strategy can shorten the start time by 19.5 %, reduce the RMS of vehicle jerking by 28.6 %, and reduce the friction work by 13.8 %.

The same conclusion can also be drawn from the low-temperature experiment (Fig. 16). At low temperature, compared with the single-layer control strategy, the double-layer control strategy can shorten the start time by 34.9 %, reduce the RMS of vehicle jerking by 35.4 %, and reduce the friction work by 30.3 %. By adopting a double-layer control strategy, the performance of the vehicle start-up process is significantly improved.

For better comparison, the values for start time, jerking RMS and friction work for the two groups are presented in Table 3.

Table 3. Comparison of the experimental results (*RMS value)

Temperature	Control strategy	Start time [s]	*Start-up jerking [-]	Friction work [kJ]
Normal (25 °C)	Single layer	2.81	2.62	509
	Double layer	2.26	1.87	436
Low (-10 °C)	Single layer	3.61	2.06	614
	Double layer	2.35	1.33	428

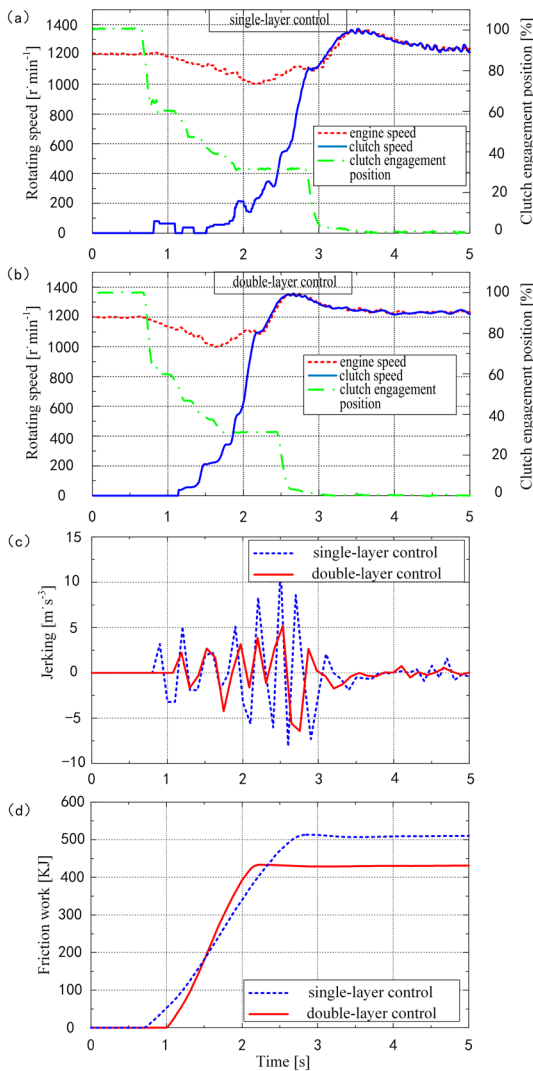


Fig. 15. Experimental results at normal temperature (25 °C), a) single-layer control, b) double-layer control, c) jerking contrast, and d) friction work contrast

6 CONCLUSIONS

In this paper, a double-layer control strategy based on an automatic clutch actuator was designed to achieve better vehicle start-up performance. Due to environmental factors such as temperature changes, the actual and target clutch engagement speeds will have a certain amount of deviation.

Simulations and experimental results show that the adoption of a double-layer control strategy reduces the influence of temperature changes on start-up performance.

The simulation and experimental results further show that compared with a single-layer control

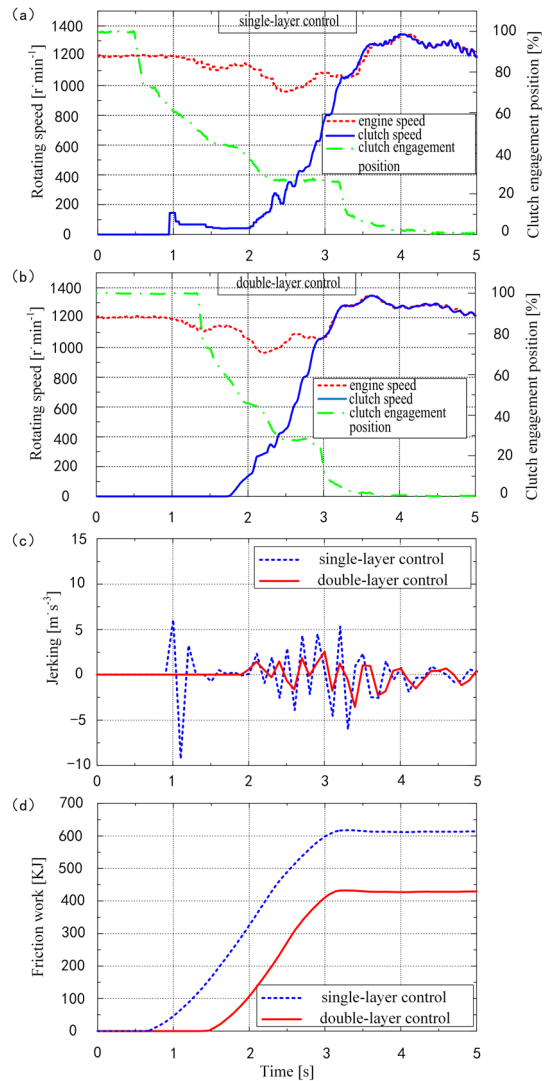


Fig. 16. Experimental results at low temperature (-10 °C), a) single-layer control, b) double-layer control, c) jerking contrast, and d) friction work contrast

strategy, the double-layer control strategy improves start-up performance.

A possible direction for future work could be to develop a neural network-based self-learning control method to improve the double-layer control strategy. It could consider changes in clutch friction plate wear and friction plate temperature to further improve vehicle start-up performance.

7 ACKNOWLEDGEMENTS

This work was supported by the Project of Jiangsu Provincial Six Talent Peaks (Grant No. 2016-JXQC-020), the Fundamental Research Funds for the Central

Universities (Grant No.309171B8811), the National Natural Science Fund of China (Grant No. 51205209 and 51205204 and 51675039), the China Scholarship Council Funds (Grant No. 201606845008) and CALT Universities Joint Innovation Funds of China (Grant No. CALT201805). Thanks for their support, this paper is possible to publish.

8 NOMENCLATURE

I_1	engine rotational inertia, [kg·m ²]
I_{c1}	clutch driving plate rotational inertia, [kg·m ²]
I_{c2}	clutch driven plate rotational inertia, [kg·m ²]
I_t	transmission, main reducer, driveshaft, etc. rotational inertia, [kg·m ²]
I_d	differential, half-shaft, etc. rotational inertia, [kg·m ²]
T_e	engine output torque, [N·m]
ω_e	engine crankshaft angular velocity, [rad·s ⁻¹]
I_e	engine and clutch driving plate rotational inertia, [kg·m ²]
T_{c1}	torque transferred by the clutch, [N·m]
T_{c2}	torque input of the transmission, [N·m]
ω_c	transmission shaft angular velocity, [rad·s ⁻¹]
I_v	vehicle equivalent rotational inertia, [kg·m ²]
i_o	powertrain system transmission ratio, [-]
T_r	ground resistance moment, [N·m]
μ	clutch plate friction coefficient, [-]
F_c	(clutch) pressing force, [N]
k_c	coefficient, [-]
T	clutch friction plate temperature, [°C]
$\Delta\omega$	clutch angular velocity difference, [rad·s ⁻¹]
Z	Number of clutch friction pairs, [-]
R_0	clutch friction plate internal radius, [mm]
R_1	clutch friction plate external radius, [mm]
q_1	liquid in/out hydraulic control cylinder, [m ³ ·s ⁻¹]
V_1	hydraulic control cylinder volume, [m ³]
S_1	hydraulic control cylinder section area, [m ²]
S_2	hydraulic master cylinder section area, [m ²]
S_3	gas-assisted hydraulic working cylinder section area, [m ²]
k	piston displacement proportional coefficient, [-]
v_3	piston movement speed, [m·s ⁻¹]
j	start-up jerking, [m·s ⁻³]
a	vehicle longitudinal acceleration, [m·s ⁻²]
u	vehicle speed, [m·s ⁻¹]
t	time, [s]
F_t	driving force, [N]
F_j	acceleration resistance, [N]
F_f	rolling resistance, [N]
F_i	gradient resistance, [N]
F_w	air resistance, [N]
η	drive train mechanical efficiency, [-]

r	wheel radius, [mm]
δ	rotational mass conversion coefficient, [-]
M	vehicle mass, [kg]
W	friction work, [J]
t_1	point at which the driving and driven plates initiate friction torque, [s]
t_2	point at which the clutch driven plate starts to rotate, [s]
t_3	point at which the driving and driven plates attain the same speed, [s]

9 REFERENCES

- [1] Amari, R., Tona, P., Alamir, M. (2009). Experimental evaluation of a hybrid MPC strategy for vehicle start-up with an automated manual transmission. *European Control Conference*, p. 4271-4277, DOI:10.23919/ECC.2009.7075071.
- [2] Van Der Heijden, A.C., Serrarens, A.F.A., Camlibel, M.K., Nijmeijer, H. (2007). Hybrid optimal control of dry clutch engagement. *International Journal of Control*, vol. 80, no. 11, p. 1717-1728, DOI:10.1080/00207170701473995.
- [3] Tripathi, K. (2014). Engagement control of automotive clutch by mechatronic system using pre-determined force trajectories. *Journal of the Institution of Engineers (India): Series C*, vol. 95, no. 2, p. 109-117, DOI:10.1007/s40032-014-0113-5.
- [4] Bryson, A. E. (2018). *Applied Optimal Control: Optimization, Estimation and Control*, Routledge.
- [5] Pisaturo, M., Senatore, A. (2016). Simulation of engagement control in automotive dry-clutch and temperature field analysis through finite element model. *Applied Thermal Engineering*, vol. 93, p. 958-966, DOI:10.1016/j.applthermaleng.2015.10.068.
- [6] Huang, Y., Wang, H., Khajepour, A., He, H., Ji, J. (2017). Model predictive control power management strategies for HEVs: A review. *Journal of Power Sources*, vol. 341, p. 91-106, DOI:10.1016/j.jpowsour.2016.11.106.
- [7] Montanari, M., Ronchi, F., Rossi, C., Tilli, A., Tonielli, A. (2004). Control and performance evaluation of a clutch servo system with hydraulic actuation. *Control Engineering Practice*, vol. 12, no. 11, p. 1369-1379, DOI:10.1016/j.conengprac.2003.09.004.
- [8] Kulkarni, M., Shim, T., Zhang, Y. (2007). Shift dynamics and control of dual-clutch transmissions. *Mechanism and Machine Theory*, vol. 42, no. 2, p. 168-182, DOI:10.1016/j.mechmachtheory.2006.03.002.
- [9] Peng, P., Wang, H., Wang, X., Wang, W., Pi, D., Jia, T. (2019). Research on the hill start assist of commercial vehicles based on electronic parking brake system. *Strojniški vestnik - Journal of Mechanical Engineering*, vol. 65, no. 1, p. 50-60, DOI:10.5545/sv-jme.2018.5422.
- [10] Park, J., Choi, S., Oh, J., Eo, J. (2019). Adaptive torque tracking control during slip engagement of a dry clutch in vehicle powertrain. *Mechanism and Machine Theory*, vol. 134, p. 249-266, DOI:10.1016/j.mechmachtheory.2018.12.033.

- [11] Lucente, G., Montanari, M., Rossi, C. (2007). Modelling of an automated manual transmission system. *Mechatronics*, vol. 17, p. 73-91, DOI:10.1016/j.mechatronics.2006.11.002.
- [12] Glielmo, L., Vasca, F. (2000). Optimal control of dry clutch engagement. *SAE Technical Paper*, paper ID: 2000-01-0837, DOI:10.4271/2000-01-0837.
- [13] Huang, Y., Wang, H., Khajepour, A., Li, B., Ji, J., Zhao, K., Hu, C. (2018). A review of power management strategies and component sizing methods for hybrid vehicles. *Renewable and Sustainable Energy Reviews*, vol. 96, p. 132-144, DOI:10.1016/j.rser.2018.07.020.
- [14] Dolcini, P., De Wit, C.C., Béchart, H. (2008). Lurch avoidance strategy and its implementation in AMT vehicles. *Mechatronics*, vol. 18, no. 5-6, p. 289-300, DOI:10.1016/j.mechatronics.2008.02.001.
- [15] Bemporad, A., Borrelli, F., Glielmo, L., Vasca, F. (2001). Hybrid control of dry clutch engagement. *European Control Conference*, p. 635-639, DOI:10.23919/ECC.2001.7075980.
- [16] Wang, H. L., Liu, H. O. (2009). The start-up control strategy of heavy-duty commercial vehicle whole-course speed regulating diesel engine. *Automotive Engineering*, vol. 31, no. 8, p. 756-760, DOI:10.19562/j.chinasae.qcgc.2009.08.016.
- [17] Wang, H. L., Liu, H. O., Zhao, J. X. (2011). Study on modification of AMT clutch based on automatic operating mechanism of flow valve. *Automotive Engineering*, vol. 33, no. 1, p. 47-51, DOI:10.19562/j.chinasae.qcgc.2011.01.012.
- [18] Amari, R., Alamir, M., Tona, P. (2008). Unified MPC strategy for idle-speed control, vehicle start-up and gearing applied to an automated manual transmission. *IFAC Proceedings Volumes*, vol. 41, no. 2, p. 7079-7085, DOI:10.3182/20080706-5-KR-1001.01200.
- [19] Van Berkel K., Hofman, T., Vroemen, B., Steinbuch, M. (2011). Optimal control of a mechanical hybrid powertrain. *IEEE Transactions on Vehicular Technology*, vol. 61, no. 2, p. 485-497, DOI:10.1109/TVT.2011.2178869.
- [20] Minh, V.T., Rashid, A.A. (2012). Automatic control of clutches and simulations for parallel hybrid vehicles. *International Journal of Automotive Technology*, vol. 13, no. 4, p. 645-651, DOI:10.1007/s12239-012-0063-y.
- [21] Van Berkel, K., Hofman, T., Serrarens, A., Steinbuch, M. (2014). Fast and smooth clutch engagement control for dual-clutch transmissions. *Control Engineering Practice*, vol. 22, p. 57-68, DOI:10.1016/j.conengprac.2013.09.010.
- [22] Wang, H.L., Liu, H.O. (2013). Optimization of automatic control strategy for AMT vehicle clutch. *Journal of Nanjing University of Science and Technology*, vol. 37, no. 5, p. 729-734, DOI:10.14177/j.cnki.32-1397n.2013.05.020.
- [23] Kim, J., Choi, S.B. (2010). Design and modeling of a clutch actuator system with self-energizing mechanism. *IEEE/ASME Transactions on Mechatronics*, vol. 16, no. 5, p. 953-966, DOI:10.1109/TMECH.2010.2059034.
- [24] Walker, P.D., Fang, Y., Zhang, N. (2017). Dynamics and control of clutchless automated manual transmissions for electric vehicles. *Journal of Vibration and Acoustics*, vol. 139, no. 6, p. 61-73, DOI:10.1115/1.4036928.
- [25] Tao, G., Wu, M., Meng, F. (2016). Online performance evaluation of a heavy-duty automatic transmission launching process. *Mechatronics*, vol. 38, p. 143-150, DOI:10.1016/j.mechatronics.2015.12.008.
- [26] Kakinuma, Y., Aoyama, T., Anzai, H. (2007). Development of the variable friction clutch applying the functional medium. *Strojniški vestnik - Journal of Mechanical Engineering*, vol. 53, no. 11, p. 755-770.
- [27] Wang, X., Li, L., He, K., Liu, C. (2018). Dual-loop self-learning fuzzy control for AMT gear engagement: Design and experiment. *IEEE Transactions on Fuzzy Systems*, vol. 26, no. 4, p. 1813-1822, DOI:10.1109/TFUZZ.2017.2779102.
- [28] Tang, X., Hu, X., Yang, W., Yu, H. (2018). Novel torsional vibration modeling and assessment of a power-split hybrid electric vehicle equipped with a dual-mass flywheel. *IEEE Transactions on Vehicular Technology*, vol. 67, no. 3, p. 1990-2000, DOI:10.1109/TVT.2017.2769084.
- [29] Minh, V.T., Rashid, A.A. (2012). Automatic control of clutches and simulations for parallel hybrid vehicles. *International Journal of Automotive Technology*, vol. 13, no. 4, p. 645-651, DOI:10.1007/s12239-012-0063-y.
- [30] Petrun, T., Flašker, J., Kegl, M. (2013). A theoretical and numerical study of an additional viscosity term in a modified elasto-plastic friction model for wet friction clutch simulations. *Strojniški vestnik - Journal of Mechanical Engineering*, vol. 59, no. 6, p. 358-366, DOI:10.5545/sv-jme.2012.920.
- [31] Yang, C., Song, J., Li, L., Li, S., Cao, D. (2016). Economical launching and accelerating control strategy for a single-shaft parallel hybrid electric bus. *Mechanical Systems and Signal Processing*, vol. 76-77, p. 649-664, DOI:10.1016/j.ymsp.2016.02.051.
- [32] Tang, X., Zhang, D., Liu, T., Khajepour, A., Yu, H., Wang, H. (2019). Research on the energy control of a dual-motor hybrid vehicle during engine start-stop process. *Energy*, vol. 166, p. 1181-1193, DOI:10.1016/j.energy.2018.10.130.
- [33] Pisaturo, M., Cirrincione, M., Senatore, A. (2014). Multiple constrained MPC design for automotive dry clutch engagement. *IEEE/ASME Transactions on Mechatronics*, vol. 20, no. 1, p. 469-480, DOI:10.1109/TMECH.2014.2335894.
- [34] Sun, S., Lei, Y., Fu, Y., Yang, C., Li, S. (2013). Analysis of thermal load for dry clutch under the frequent launching condition. *SAE Technical Paper*, paper ID: 2013-01-0814, DOI:10.4271/2013-01-0814.
- [35] Senatore, A., D'Auria, C., Pisaturo, M. (2017). Frictional behaviour and engagement control in dry clutch based automotive transmissions. *Vehicle Engineering*, vol. 4, p. 1-12, DOI:10.14355/ve.2017.04.001.

Fatigue of Cellular Structures – a Review

Branko Nečemer* – Matej Vesenjak – Srečko Glodež

University of Maribor, Faculty of Mechanical Engineering, Slovenia

A review of the fatigue and fracture behaviour of cellular structures with consideration of their fabrication and characterization is presented in this paper. The review is focused on some typical and often used cellular structures, which are divided into three main groups: (1) pre designed regular cellular structures, (2) irregular cellular structures, (3) composites with cellular cores. For each group, the current manufacturing technique is presented for producing the particular cellular structure belonging this group. Furthermore, the state-of-the-art of the fatigue behaviour is explained for the analysed cellular structures. Based on the findings in this review, it can be concluded that cellular structures show a huge potential to become important light-weight structural materials of the future with further development of additive manufacturing technologies, or with introduction of some new, more cost effective manufacturing techniques. However, the knowledge of the fatigue behaviour of these structures is poor, and should be the subject of the further investigations.

Keywords: cellular structures, porous materials, foam, fatigue behaviour, dynamic strength, crack growth

Highlights

- General characteristics of cellular structures are explained.
- Fatigue and fracture behaviour of different cellular structures is presented.
- Fabrication techniques of different cellular structures are briefly introduced.
- The guideline's for the further work are exposed.

0 INTRODUCTION

Cellular structures are a relatively new class of materials in modern engineering. They represent a unique opportunity for adoption in lightweight structures, which are useful in advanced structural and thermal applications. Therefore, the research of their behavior under quasi-static and dynamic loading is of extreme importance for various engineering applications. Although cellular structures have a favourable combination of physical properties, mainly the mechanical and thermal properties have been the subject of thorough research so far. In general, the most important structural feature of the cellular structure is the relatively high stiffness in respect to the high porosity (low density) of the structure [1] and [2]. Besides their light weight, cellular structures offer additional advantages, such as sound insulation and damping, mechanical energy absorption, floatability, durability at dynamic load, and recycling [3]. Often, several advantageous properties can be extracted simultaneously, making cellular structures important as multifunctional materials in modern engineering applications.

The main parameters that define the mechanical and thermal properties of a cellular structure are the relative density (porosity), base material, morphology and topology. The relative density is defined as the ratio of the density of the cellular structure (ρ^*) and the density of the solid base material (ρ_s), while the porosity (p) is defined as the ratio between the total

pore volume (V_p) and the total volume of the solid base material including pores ($V_s + V_p$) [1] and [4]. The cellular structures show a specific compressive response, which is different from the conventional solid materials. Fig. 1 shows the characteristic mechanical response during compression loading of a cellular structure, which can be divided into four main areas: I.) Elastic part ($0 - \varepsilon_a$), where the structure deforms quasi-linearly; II.) The transition in the plastic region ($\varepsilon_a - \varepsilon_b$), where the base material starts to yield, thus, the intercellular walls and connections in local areas are subjected to plastic deformation; III.) Plateau stress (σ_{pl}) ($\varepsilon_b - \varepsilon_c$), where the cellular material reaches almost a constant stress level in a very wide range of

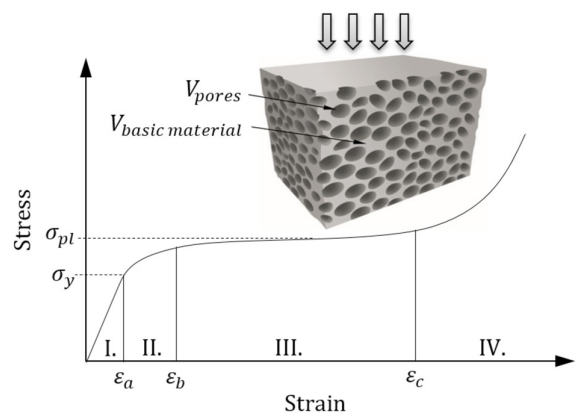


Fig. 1. Characteristic response of the cellular structure under compression loading [5]

specific deformations (massive plastic deformation of the cell walls and struts), and IV.) Densification ($>\epsilon_c$), where the intercellular walls and struts collapse, resulting in a decrease of the global porosity and an increase in the global stiffness [1] and [4].

So far, extensive research has been performed in terms of characterization of the mechanical properties of various types of cellular structures, in order to study the compression [6] and [7], tension, torsion and shear under uniaxial and multiaxial loading conditions at quasi-static and dynamic loading rates, using experimental methods [8] and numerical simulations [9] and [10]. The response of cellular structures can be adopted by a combination of production processes and production parameters. In the last few decades, a number of distinct process-routes have been developed to fabricate metal and ceramic cellular structures, in order to decrease the manufacturing costs and increase the production capabilities. Thus, extensive research has been performed regarding the optimal manufacturing methods for cellular metals. These methods can be classified according to the state the metal is processed in [11]. Generally, we can define several groups of manufacturing methods, which are summarised in Fig. 2.

From Fig. 2 it can be observed that there are several ways to fabricate cellular structures, which are specially designed by taking advantage of the

characteristic properties of the base materials [11]. Current manufacturing methods, especially additive manufacturing technologies, enable the creation of various cellular structures, either open-cell or closed-cell foams, with a varying regularity, isotropy and density. The most common methods for producing the three-dimensional (3D) cellular structures is by sintering of dusts, foaming and casting [2], [3] and [10]. The most common method for production of two-dimensional (2D) cellular structures is by laser or water jet cutting. Further details on fabrication of different types of cellular structures are given in [10].

To date, a lot of researches regarding static and crash performance of cellular structures have been performed and then published in the professional literature. However, a very few researches were focused on the fatigue problems of the cellular structures. In that respect, this paper provides a review of the fatigue behaviour of cellular structures, according to the different production methods and type of cellular structure. In general, the cellular structures can be classified by the cell connectivity (morphology: Closed- and open-cell structures, [1]) or by the cell regularity (topology: Regular and irregular structures [12]). Herein, the cellular structures presented are classified and discussed in two groups: i) regular (ordered) and ii) irregular (stochastic) cellular structures.

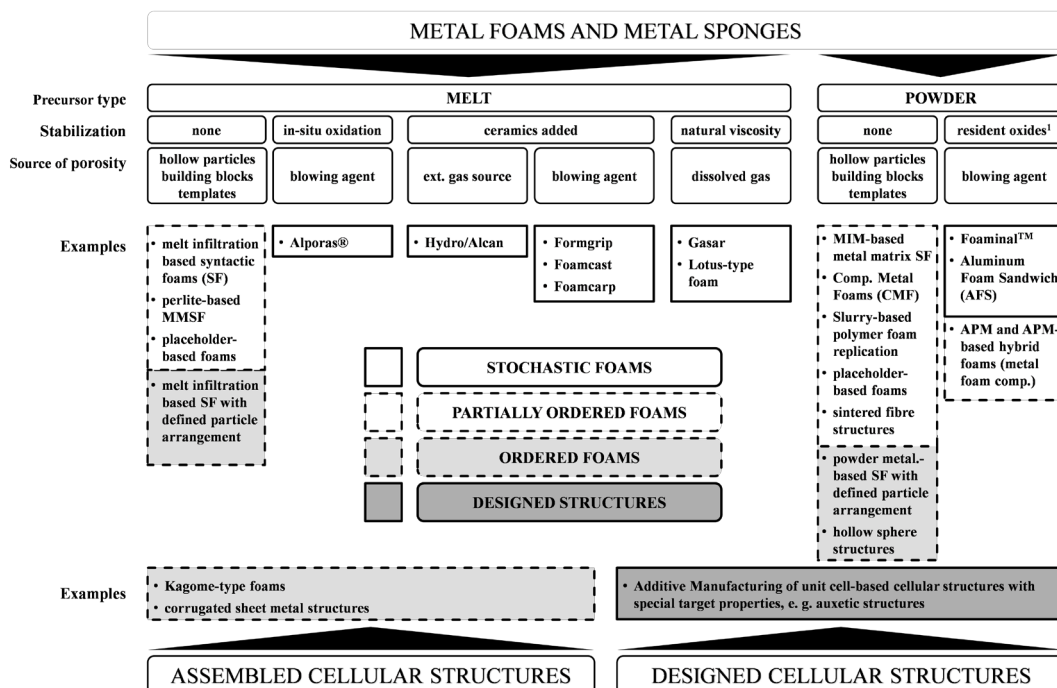


Fig. 2. Overview of manufacturing processes and cellular metals [12]

1 PRE DESIGNED REGULAR CELL STRUCTURES

The additive manufacturing technique is the most common method for production pre-design of cellular structures by using metal powder and an energy source to build up the geometry. Additive manufacturing techniques can be, according to the applied energy, divided roughly into two groups: i) selective laser melting (SLM) method, and ii) electron beam melting (EBM) method. Both can be used for the manufacturing of complex and customised 3D geometries of open-cell structures [13]. In general engineering praxis, titanium alloy powders are used most often. Therefore, porous titanium alloys have also been studied extensively for biomedical applications, e.g. bone implants [14] to [16]. Porous titanium implants, in addition to preserving the excellent biocompatible mechanical properties of titanium, have very low stiffness values, which are

comparable to those of natural bones [17]. Some typical regular cellular structures are shown in Fig. 3.

Most of the research works in this field have been focused on experimental testing [15], [16], [19] to [24] or numerical simulations [25] and [26]. In [20], [27] and [28], the authors investigated the influence of the cell's shape (see Fig. 4) on the fatigue and mechanical properties of several pre designed cellular structures. In articles [15] to [17] and [20] to [24], the authors continued this work with the additional investigation of the influence of the material types which were used for experimental testing.

Table 1 shows the static mechanical properties of some typical regular cellular structures which were tested under quasi-static compressive loading. It is evident that both the fabrication method and the shape of the base cell have a significant influence on the observed mechanical properties, i.e. yield stress (σ_y),

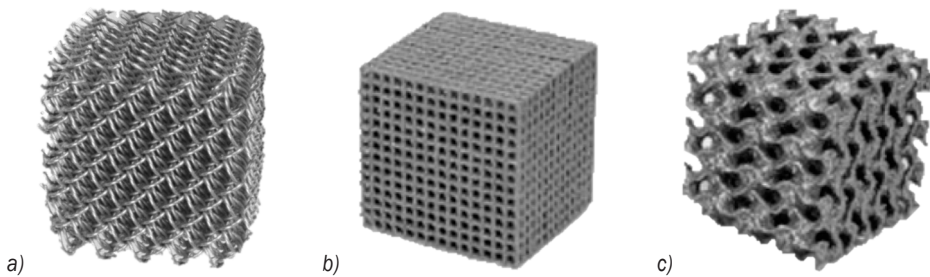


Fig. 3. Regular cellular structures; a) Kagome wire structure [12], b) Cube cellular structure and c) Gyroid cellular structure [18]

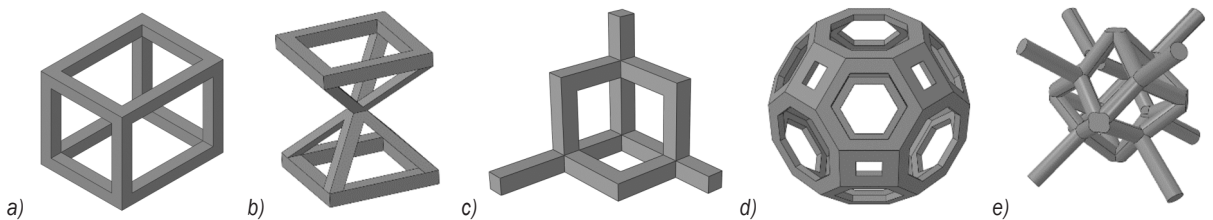


Fig. 4. Shapes of the basic cells of regular cellular structures; a) cube, b) G7, c) diamond, d) truncated cuboctahedron and e) rhombic dodecahedron

Table 1. Mechanical properties of typical regular cellular structures by quasi-static compressive loading

Fabrication method	Shape of the base cell	Material	Porosity [%]	σ_y [MPa]	σ_{max} [MPa]	σ_{pl} [MPa]	E [GPa]	Ref.
SLM	Cubic	Ti6Al4V ELI	77	67.9	100.5	59.4	/	[16]
EBM	Cubic	Ti6Al4V	63.2	/	196.0	155.9	14.9	[20]
EBM	G7	Ti6Al4V	64.5	/	61.0	59.6	2.4	[20]
SLM	Diamond	Ti6Al4V ELI	77.3 to 80.1	34.5 to 43	55.6 to 57.9	35.3 to 36.5	1.36	[16] and [22]
EBM	Diamond	Ti6Al4V	70	62.87	/	/	/	[29]
SLM	Truncated cuboctahedron	Ti6Al4V ELI	74.5	66.9	89.9	59.6	/	[16]
SLM	Rhombic dodecahedron	Ti6Al4V ELI	≈ 75	≈ 46	64.5	52.6	/	[16], [24] and [30]
EBM	Rhombic dodecahedron	Ti6Al4V	62.1	/	112.0	77.2	6.3	[20]
EBM	Rhombic dodecahedron	Ti-24Nb-4Zr-8Sn	72.5 to 77.4	29.8 to 45.5	/	28.5 to 42	≈ 1.44	[15] and [30]

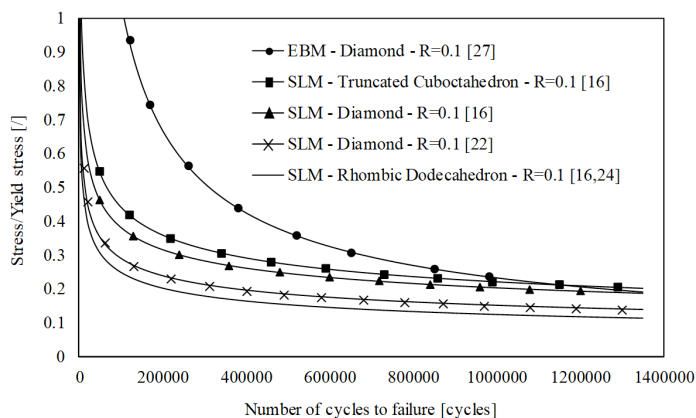


Fig. 5. S-N curves of typical regular cellular structures

maximum compressive stress (σ_{\max}), the plateau stress (σ_{pl}) and modulus of elasticity (E).

Fig. 5 shows the fatigue behaviour (S-N curves) of typical regular cellular structures by dynamic loading. Here, the experimental tests were performed at the load ratio $R = \sigma_{\min} / \sigma_{\max} = 0.1$ (in compression) and frequency of 10 Hz to 15 Hz. The maximum loading σ_{\max} within the loading cycle was determined based on the previous static tests, and varied between $0.2\sigma_y$ and $0.8\sigma_y$. It follows that all experiments corresponded to the elastic area of stress-strain relationship, and the stress-life approach was used to determine the material fatigue properties. The fatigue limit was established by plotting the normalised values of stress (σ_{\max} / σ_y) versus the number of cycles to failure N . It is evident from Fig. 5, that the EBM-cellular structure with diamond basic cells has the highest fatigue strength, while the lowest fatigue strength corresponds to the SLM-cellular structure with Rhombic dodecahedron basic cells.

2 IREGULAR CELL STRUCTURES

2.1 Closed- and Open-Cell Foams

Closed- and open-cell cellular structures (see Fig. 6) exhibit a stochastic pore distribution with a highly irregularity, which is a consequence of the production methods [1]. Production of open-cell structure is usually based on the method of replicating the polymer foam structure, which can serve as a core in the case of the investment casting, or be coated by electrolysis with metals steam [2]. The final product is an open-cell cellular structure of struts and interconnected cell architecture (high connectivity between the adjoining cells). The production of closed-cell foams is based

mainly on powder metallurgy (using precursors), or gas injection, resulting in cellular structures with cells that are almost completely separated from each other with intercellular wall surfaces. These types of foams are used in applications mostly as energy absorbers or structural parts [3]. Different metals (e.g. aluminium) can be used for fabrication of open- and closed cellular structures, achieving porosities above 90 %.

Numerous studies have been performed for the characterization of the mechanical properties of the metal foams, but the available information on fracture and fatigue is rather limited. Some work on the standard fatigue properties of closed-cell aluminium alloy foams was performed by Zettl et al. [33] and [34]. They used an ultrasonic test method to investigate the tension-compression fatigue properties. Their work was continued by Zettl et al. [34] and McCullough et al. [35], who investigated the tension/tension and compression/compression fatigue behaviour of closed-cell aluminium alloy foam experimentally. Kashef et al. [36] performed the experimental and numerical investigation to observe the fracture toughness and fatigue crack growth in open-cell stainless steel foam, while a similar procedure for titanium foam at two different load ratios ($R = K_{\min} / K_{\max} = 0.5$ and $R = 0.1$) was performed by Kashef et al. [37]. Zhao et al. [38] investigated the damage evolution and damage mechanism in closed-cell aluminium alloy foam under tension/tension fatigue loading experimentally, while the failure mechanisms of closed-cell aluminium foam under monotonic and cyclic loading was investigated by Amsterdam et al. [39]. Fatigue crack propagation in closed-cell aluminium alloy foam was investigated experimentally by Fan et al. [40] and Taherishargh et al. [41]. In [42], the authors performed an experimental investigation of the low cycle fatigue behaviour of

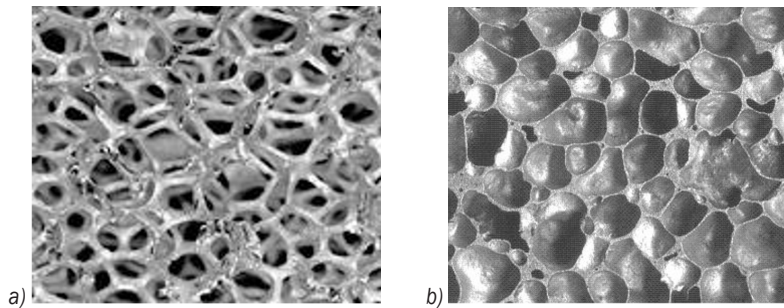


Fig. 6. Stochastic cellular structures: a) open-cell foam [31], b) closed-cell foam [32]

closed-cell aluminium foam with consideration of the multiple strain amplitude. Their results confirmed fatigue behaviour which corresponds to the Coffin–Manson relationship. Similar investigation was performed by Linul et al. [43], where researchers investigated the low-cycle fatigue behaviour of ductile closed-cell aluminium alloy foam. The fatigue tests were performed in uniaxial compression with a stress ratio of $R=0.1$ at a loading frequency of 10 Hz. Furthermore, the effect of the structure irregularity, number and the size of the cell were investigated. The experimental results have shown the significant influence of structural irregularities on the fatigue behaviour of the analysed aluminium foam. Based on the experimental results, researchers concluded that the scatter of fatigue life increases as the higher irregularity of cell structure and that the fatigue life decreases as the number and the size of large cells increases [43]. Motz et al. [44] investigated the fatigue crack propagation of two types of cellular materials: (i) closed-cell aluminium foam with two different densities, and (ii) hollow sphere structures made of stainless steel (316L). Based on the fatigue tests and the microstructural analysis of the fracture surface, a significant difference was observed in the fatigue crack propagation mechanisms between these two types of cellular metals. A similar investigation was performed by Olurin et al. [45], where the influence was investigated of the relative density of the porous structure (Alporas and Alulight aluminium alloy foams) on the fatigue crack growth. Here, the influence was also considered of the mean stress effect and the single peak overload on the fatigue crack propagation. The authors concluded that the Paris exponent m increases more than twice with an increase of load ratio R from 0.1 to 0.5. The comprehensive study of the fatigue crack propagation of closed- and open-cell foams made of different materials was presented by Kashef et al. [36] and [37], Fan et al. [40], Motz et al. [44] and Olurin et al. [45]. Their experimental results

were presented by the crack propagation curves as shown in Fig. 7, which correspond to the Paris equation:

$$\frac{da}{dN} = C \cdot \Delta K^m, \quad (1)$$

where da/dN is the fatigue crack growth rate, C and m are the experimentally determined material parameters and ΔK is the stress intensity factor range. It is evident that the shape of a cell and the microstructure of the base material of treated foam, have a significant influence on the crack growth rate. Here, the open-cell foams made of titanium and stainless steel have a higher Paris exponent than the foams made of aluminium alloys. The authors explained this fact as a consequence of the crack closure effect and crack bridging, which reduce the crack growth rate and, consequently, extend the fatigue life.

In everyday engineering praxis, open- and closed-cell foams made of several polymers are often used for different engineering applications [46]. The polymer foams have excellent characteristics, such as strength to weight ratio, superior acoustic absorption, and manufacturing possibilities to produce different shapes of final products. In [47], the researchers analysed tension, compression and shear fatigue behaviour of closed-cell polymer foams. They concluded that foam porosity is an important factor influencing the fatigue behaviour of polymer foams.

2.2 Unidirectional Porous Structures

Lotus or Gasar porous structures can be recognised by their elongated cylindrical pores (Fig. 8) and, therefore, exhibit closed-cell morphology with the uni-directional elongated parallel pores. They are fabricated by unidirectional solidification in a pressurised gas atmosphere [48]. Further details on the fabrication method are given in [49]. The fabrication procedure results in metal structures (e.g. copper, steel), etc. with a high level of anisotropy, which

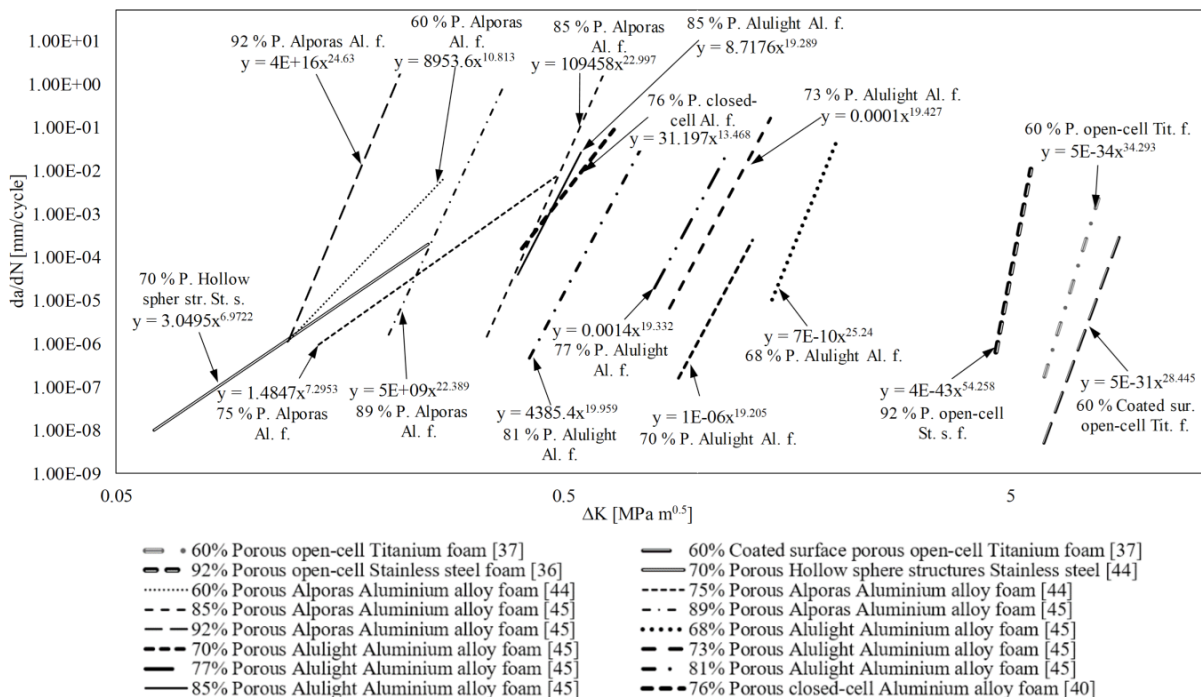


Fig. 7. Log (da/dN – log ΔK) curves of different porous materials

depends on the distribution of pores. The porosity is usually lower than 70 % [50], which is lower in comparison to the conventional open- and closed cell cellular metals. The pore size and distance between the pores affect the mechanical properties strongly, which are presented in [51] and [52]. They can be applied in structural and thermal applications.

There are some studies where researchers investigated the fatigue behaviour of lotus porous material experimentally and numerically. Seki et al. [54] investigated experimentally the effects of anisotropic pore structure and fibre texture on the fatigue properties of lotus-type porous magnesium. The experimental results showed that the fatigue strength in the direction parallel to the longitudinal axis of pores (z-axis) is higher than the fatigue

strength in the perpendicular direction (x-axis and y-axis). Based on the experimental results, they concluded that the fatigue strength at the finite life of a magnesium lotus structure is closely related and proportional to the ultimate tensile strength for both loading directions (parallel and perpendicular to the pores). The experimental investigation of the fatigue crack initiation and propagation in lotus-type porous copper was performed in [55]. In this research work, the authors used two types of specimen: (i) a specimen with a notch, and (ii) a specimen without a notch. Based on the experimental results, the authors concluded that the high stress is concentrated around large pores which affect the direction of the crack propagation. In the case of parallel loading, the fatigue crack was propagated along a straight line, while, for

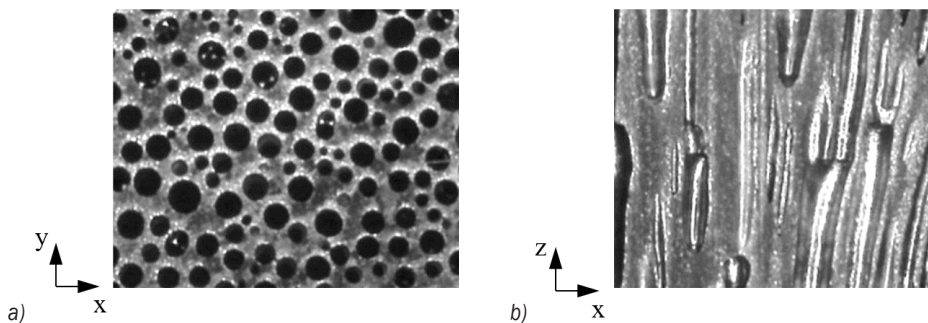


Fig. 8. Cross-section of the unidirectional (Lotus) porous structure [53]; a) transversal cross-section b) longitudinal cross direction

the perpendicular loading, the crack was propagated along a path in which stress was highly concentrated.

Numerical investigation of the fatigue crack initiation and propagation in a lotus-type porous nodular cast iron was performed by Glodež et al. [56]. In this article, the fatigue behaviour of the lotus structure was investigated under tensile loading in transversal and longitudinal directions. Kramberger et al. [57] and [58] investigated the low-cycle fatigue behaviour of lotus-type porous materials, where the fatigue life was modelled by using the damage initiation and evolution law, based on the inelastic strain energy approach. This method generally offers a capability for modelling the progressive fatigue damage and failure of different porous materials. More about this method is described in [57], where the numerical simulations were performed through simplified 2D computational models with regular and more realistic irregular pore topologies. The computational results showed that the distribution of pores has a significant influence on the low-cycle fatigue behaviour of the lotus-type porous materials. The fatigue damage first appeared around the large pores, and damage was further propagated between pores where the stress was highly concentrated.

2.3 Honeycomb Structures

Honeycombs are 2D cellular structures, which can be found in nature or fabricated artificially from metals or polymers. These types of metal cell structure are fabricated mostly by the expansion process, and from sheet metal rolls by cutting and bending. The production methods and mechanical properties of honeycombs are described in [59]. In general, regular honeycomb structures (with hexagonal cell shape) are used in engineering. However, irregular honeycomb structures can also be found based on the Voronoi cell distribution (Fig. 9).

There are some studies [61] to [70], where researchers investigated the fatigue and fracture behaviour of honeycomb cell structures. In articles

[61] and [62], the researchers studied the mechanisms of crack growth in random oriented (Voronoi) and repeated oriented honeycomb cell structures mathematically. Based on the experimental and numerical results, the authors concluded that the random oriented Voronoi honeycomb is more sensitive to fatigue than the repeated oriented honeycomb cell structure. The increased sensitivity arises from the stress distribution within the cell walls of the Voronoi honeycomb relative to the repeated oriented honeycomb cell structure.

2.4 Auxetic Cellular Structures

A recent type of cellular metals are the auxetic cellular structures (Fig. 10a), which exhibit a negative Poisson's ratio (counter intuitive behaviour: A material under compression becomes thinner in cross-section, and vice-versa in tension [71]). The advanced geometrical possibilities of auxetic cellular materials provide many opportunities for their wide application, due to their particular and unique mechanical properties. Initially, they were fabricated with transformation of conventional open-cell foam (Figs. 10b and c). However, their recent breakthrough is associated with current advances in additive manufacturing, that allow fabrication of new 3D auxetic structures [71].

In the article of Bezazi and Scarpa [73], the experimental study of tensile fatigue behaviour of conventional PU-PE open-cell foam and auxetic thermoplastic foam is described. Auxetic foam exhibits counter-intuitive deformation behaviour in comparison with the conventional materials. In the article, the experimental results showed that the auxetic foam has a higher static mechanical resistance and resistance to failure if compared to the conventional one. The auxetic foam also has a significant increase in energy absorption for compressive cyclic loading compared to the conventional foam.

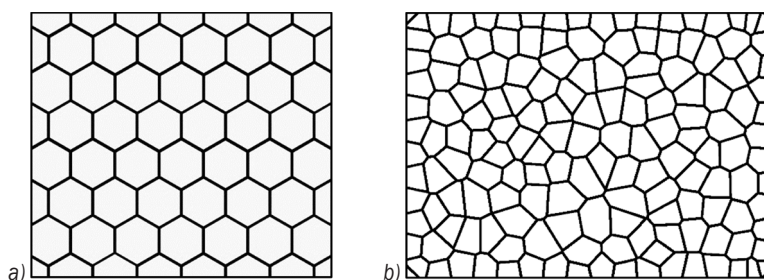


Fig. 9. Honeycomb cell structures [60]; a) regular cell distribution, b) irregular (Voronoi) cell distribution

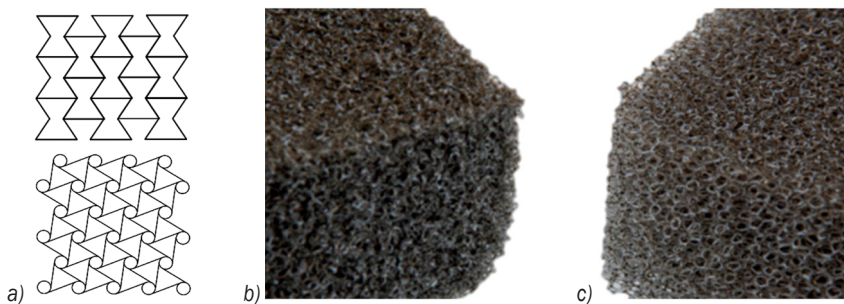


Fig. 10. Examples of: a) regular auxetic cellular structures [12] and [71], b) irregular auxetic foam, and c) irregular conventional foam [72]

3 COMPOSITES WITH CELLULAR CORES

Further advantages of cellular structures can be obtained in combinations of thin-walled tubes [74] and [75] or metal sheets [76]. In engineering applications, cellular structures are often used as cores: (i) filling the empty spaces in structural parts, or (ii) in sandwich panels (Fig. 11). The honeycomb cell structure is one of the most often used cellular cores of composite sandwich structures, which is shown in Fig. 11. Composite structures with cellular cores are being used increasingly in high-performance structural applications and many industries, from aerospace, automotive and furniture industries to packaging and logistics [64].

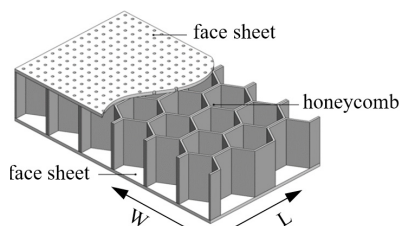


Fig. 11. Description of the honeycomb sandwich structure [77]

There are some articles [64] to [70] and [78] to [80] where researchers investigated the fatigue behaviour of honeycomb sandwich structures. Jen et al. [64] investigated the temperature dependent strengths and fatigue bending strengths of adhesively bonded aluminium honeycomb sandwich structures experimentally. In the articles [65] and [69], the authors performed fatigue tests of composites with two different sandwich cores (with aluminium core and with aramide fibres core) and with two different cell configurations (W- and L-configuration; see Fig. 11). The experimental results showed that the morphology and topology (cells' configuration) have a significant influence on the lifetime of the sandwich structure made of aramide fibres core. Sandwich structure with L-configuration had a larger lifetime

compared to the W-configuration. The difference in lifetime is a consequence of micro cracks formation, which lead to the shorter lifetime of the structure. In case of the sandwich structure made of aluminium core, the cells' configuration had no influence on the lifetime of the sandwich structure. The fatigue failure is constantly caused by cracking in the lower face of sandwich structure made of aluminium core. From the experimental results authors concluded that the lifetime of the honeycomb structure made of aluminium cores are significantly larger than the lifetime of material made of aramide fibres cores in all analysed structures. The lifetime values for both configurations are in the same range for two analysed materials and correspond to the 60 % of the maximum loading [69]. In [66], the authors investigated experimentally the influence of the load ratio (R) and frequency (f) at an arbitrary temperature on the fatigue response. In the articles [67] to [70] and [78], the experimental results are presented of the fatigue behaviour under four points' bending tests of different materials of the sandwich core and face sheets. The effect of the thickness of the face sheet on the bending fatigue strength of aluminium honeycomb sandwich beams have been studied by Jen and Chang [79], while the effect of the amount of adhesive on the bending fatigue strength of adhesively bonded aluminium honeycomb sandwich beams have been studied by Jen et al. [80].

4 CONCLUSIONS

The paper gives an overview of the fatigue behaviour of cellular structures with consideration of their fabrication and characterization. The review is focused on some of the most typical cellular structures, which are divided into three main groups: (1) pre-designed regular cellular structures, (2) irregular cellular structures, and (3) composites with cellular cores.

For the first group (pre designed regular cellular structures), the experimental investigations have

shown that the fabrication methods SLM, or EBM, and the shape of the base cell (diamond, cube, rhombic dodecahedron etc.), have a significant influence on the observed mechanical properties, i.e. yield stress, maximum compressive stress and modulus of elasticity. The extended fatigue testing of these structures indicated that the EBM-cellular structures with diamond basic cells have the highest fatigue strength, while the lowest fatigue strength corresponds to the SLM-cellular structures with rhombic dodecahedron basic cells.

Closed- and open-cell foams, lotus cellular structures, honeycomb cellular structures and auxetic cellular structures have been analysed in the framework of the second group. The following conclusions could be made:

- The available information on the fatigue and fracture behaviour of closed- and open-cell foams is very limited. However, the experimental studies of the fatigue crack propagation of closed- and open-cell foams made of different materials have shown that the shape of cell and the microstructure of the base material of the treated foam have a significant influence on the crack growth rate. Furthermore, the open-cell foams made of titanium and stainless steel have a higher Paris exponent than the foams made of aluminium alloys.
- The experimental and numerical investigations of the fatigue behaviour of lotus porous materials indicated that the fatigue strength in the direction parallel to the longitudinal axis of pores is higher than the fatigue strength in the perpendicular direction. Furthermore, the distribution of pores has a significant influence on the fatigue behaviour; the fatigue damage first appears around the large pores, and further propagates between pores where the stress is highly concentrated.
- The honeycomb cellular structures have also been studied experimentally and numerically. The results show that the random oriented Voronoi honeycomb is more sensitive to fatigue than the repeated oriented honeycomb cell structure. The increased sensitivity arises from the stress distribution within the cell walls of the Voronoi honeycomb relative to a repeated oriented honeycomb cell structure.
- Very limited investigations were conducted considering the fatigue behaviour of the auxetic cellular structures. The initial researches in this field have shown that the auxetic foams have a higher energy absorption under compressive

cyclic loading if compared to the conventional foams.

In the framework of the third research group (composites with cellular cores), the available experimental results are related to the aluminium honeycomb sandwich structures. The results showed that the morphology and topology (configuration) have significant influence on the lifetime of the treated structure at a constant load level.

Finally, it can be concluded that the cellular materials and structures show huge potential to become important light-weight structural materials of the future, with further development of additive manufacturing technologies, or with introduction of some new, more cost effective manufacturing techniques. However, the knowledge of the fatigue behaviour of such structures is relatively poor, and should be the subject of the further investigations. The latter is especially related to the auxetic cellular structures, which provide many opportunities for their wide applications due to their advanced physical characteristics. The auxetic cellular structures have also a huge potential in medical applications like cardiovascular expandable stents. The main purpose of the cardiovascular expandable stent is to restore patency of blood vessels, where the volume of the bloodstream is reduced. In the bloodstream, cardiovascular expandable stents are loaded with a cyclic load in high cycle fatigue regime. From that respect, the opportunity for the further research work could be design of a new geometry of the cardiovascular expandable stents made of auxetic cellular structures and further investigation of the fatigue behaviour of such structures.

5 ACKNOWLEDGEMENT

The authors acknowledge the financial support of the Research Core Funding (No. P2-0063) and the basic research project (No. J2-8186) from the Slovenian Research Agency.

6 REFERENCES

- [1] Gibson, L.J., Ashby, M.F., (1997). *Cellular Solids*. Cambridge University Press, Cambridge.
- [2] Borovinšek, M. (2009). *Computational Modeling of Irregular Cellular Structures*. PhD thesis, University of Maribor, Faculty of Mechanical Engineering, Maribor. (in Slovene)
- [3] Persheng, L., Bing, Y., Anmin, H., Karming, L. (2001). Development in applications of porous metals. *Transactions of Nonferrous Metals Society of China*, vol. 11, no. 5, p. 629-638.

- [4] Ashby, M.F., Evans, A.G., Fleck, N.A., Gibson, L.J., Hutchinson, J.W., Wadley, H.N.G., (2000). *Metal foams: a design guide*. Elsevier Science, Burlington, DOI:10.1016/b978-075067219-1/50001-5.
- [5] Nečemer, B., Zupanič, F., Ren, Z. (2016). Cellular metal materials. *Vakuumist*, vol. 36, no. 1, p. 13-18.
- [6] Niknam, H., Akbarzadeh, A.H. (2018). In-plane and out-of-plane buckling of architected cellular plates: Numerical and experimental study. *Composite Structures*, vol. 206, p. 739-749, DOI:10.1016/j.compstruct.2018.08.026.
- [7] Lehmhus, D., Marschner, C., Banhart, J., Bomas, H. (2002). Influence of heat treatment on compression fatigue of aluminium foams. *Journal of Materials Science*, vol. 37, no. 16, p. 3447-3451, DOI:10.1023/A:1016506905271.
- [8] Krupp, U., Poltersdorf, P., Nestic, S., Baumeister, J., Weise, J. (2014). Monotonic and cyclic deformation behaviour of Fe-36Ni (INVAR) syntactic foam. *Materialwissenschaft und Werkstofftechnik*, vol. 45, no. 12, p. 10921098, DOI:10.1002/mawe.201400357.
- [9] Hung, H.-H., Sung, Y.-C., Chang, K.-C., Yin, S.-H., Yeh, F.-Y. (2016). Experimental testing and numerical simulation of a temporary rescue bridge using GFRP composite materials. *Construction and Building Materials*, vol. 114 p. 181-193, DOI:10.1016/j.conbuildmat.2016.03.199.
- [10] Tabacu, S., Ducu, C. (2018). Experimental testing and numerical analysis of FDM multi-cell inserts and hybrid structures. *Thin-Walled Structures*, vol. 129, p. 197-212, DOI:10.1016/j.tws.2018.04.009.
- [11] Banhart, J. (2001). Manufacture, characterisation and application of cellular metals and metal foams. *Progress in Materials Science*, vol. 46, no. 6, p. 559-632, DOI:10.1016/S0079-6425(00)00002-5.
- [12] Lehmhus, D., Vesenjak, M., Schampheleire, S., Fiedler, T. (2017). From Stochastic Foam to Designed Structure: Balancing Cost and Performance of Cellular Metals. *Materials*, vol. 10, no. 8, p. 922, DOI:10.3390/ma10080922.
- [13] Loeber, L., Biamino, S., Ackelid, U., Sabbadini, S., Epicoco, P., Fino, P., Eckert, J. (2011). Comparison of selective laser and electron beam melted titanium aluminides. *22nd Solid Freeform Fabrication Symposium. An Additive Manufacturing Conference*, Austin, p. 547-556.
- [14] Aşik, E.E., Bor, Ş. (2015). Fatigue behavior of Ti-6Al-4V foams processed by magnesium space holder technique. *Materials Science and Engineering: A*, vol. 621, p. 157-165, DOI:10.1016/j.msea.2014.10.068.
- [15] Liu, Y.J., Wang, H.L., Li, S.J., Wang, S.G., Wang, W.J., Hou, W.T., Hao, Y.L., Yang, R., Zhang, L.C. (2017). Compressive and fatigue behavior of beta-type titanium porous structures fabricated by electron beam melting. *Acta Materialia*, vol. 126, p. 58-66, DOI:10.1016/j.actamat.2016.12.052.
- [16] Amin Yavari, S., Ahmadi, S.M., Wauthle, R., Pouran, B., Schrooten, J., Weinans, H., Zadpoor, A.A. (2015). Relationship between unit cell type and porosity and the fatigue behavior of selective laser melted meta-biomaterials. *Journal of the Mechanical Behavior of Biomedical Materials*, vol. 43, p. 91-100, DOI:10.1016/j.jmbbm.2014.12.015.
- [17] Hedayati, R., Amin Yavari, S., Zadpoor, A.A. (2017). Fatigue crack propagation in additively manufactured porous biomaterials. *Materials Science and Engineering: C*, vol. 76 p. 457-463, DOI:10.1016/J.MSEC.2017.03.091.
- [18] Zaharin, H.A., Abdul Rani, A.M., Azam, F.I., Ginta, T.L., Sallih, N., Ahmad, A., Yunus, N.A., Zulkifli, T.Z.A. (2018). Effect of unit cell type and pore size on porosity and mechanical behavior of additively manufactured Ti6Al4V scaffolds. *Materials*, vol. 11, no. 12, p. 2402, DOI:10.3390/ma11122402.
- [19] Hedayati, R., Amin Yavari, S., Zadpoor, A.A. (2017). Fatigue crack propagation in additively manufactured porous biomaterials. *Materials Science and Engineering: C*, vol. 76, p. 457-463, DOI:10.1016/j.msec.2017.03.091.
- [20] Zhao, S., Li, S.J., Hou, W.T., Hao, Y.L., Yang, R., Misra, R.D.K. (2016). The influence of cell morphology on the compressive fatigue behavior of Ti-6Al-4V meshes fabricated by electron beam melting. *Journal of the Mechanical Behavior of Biomedical Materials*, vol. 59, p. 251-264, DOI:10.1016/j.jmbbm.2016.01.034.
- [21] Van Hooreweder, B., Apers, Y., Lietaert, K., Kruth, J.P. (2017). Improving the fatigue performance of porous metallic biomaterials produced by Selective Laser Melting. *Acta Biomaterialia*, vol. 47 p. 193-202, DOI:10.1016/j.actbio.2016.10.005.
- [22] de Krijger, J., Rans, C., Van Hooreweder, B., Lietaert, K., Pouran, B., Zadpoor, A.A. (2017). Effects of applied stress ratio on the fatigue behavior of additively manufactured porous biomaterials under compressive loading. *Journal of the Mechanical Behavior of Biomedical Materials*, vol. 70, p. 7-16, DOI:10.1016/j.jmbbm.2016.11.022.
- [23] Li, F., Li, J., Huang, T., Kou, H., Zhou, L. (2017). Compression fatigue behavior and failure mechanism of porous titanium for biomedical applications. *Journal of the Mechanical Behavior of Biomedical Materials*, vol. 65, p. 814-823, DOI:10.1016/j.jmbbm.2016.09.035.
- [24] Amin Yavari, S., Wauthle, R., van der Stok, J., Riemsdag, A.C., Janssen, M., Mulier, M., Kruth, J.P., Schrooten, J., Weinans, H., Zadpoor, A.A. (2013). Fatigue behavior of porous biomaterials manufactured using selective laser melting. *Materials Science and Engineering: C*, vol. 33, no. 8, p. 4849-4858, DOI:10.1016/j.msec.2013.08.006.
- [25] Zargarian, A., Esfahanian, M., Kadkhodapour, J., Ziaei-Rad, S. (2016). Numerical simulation of the fatigue behavior of additive manufactured titanium porous lattice structures. *Materials Science and Engineering: C*, vol. 60 p. 339-347, DOI:10.1016/j.msec.2015.11.054.
- [26] Campoli, G., Borleffs, M.S., Amin Yavari, S., Wauthle, R., Weinans, H., Zadpoor, A.A. (2013). Mechanical properties of open-cell metallic biomaterials manufactured using additive manufacturing. *Materials and Design*, vol. 49, p. 957-965, DOI:10.1016/J.MATDES.2013.01.071.
- [27] Yan, C., Hao, L., Hussein, A., Raymond, D. (2012). Evaluations of cellular lattice structures manufactured using selective laser melting. *International Journal of Machine Tools and Manufacture*, vol. 62, p. 32-38, DOI:10.1016/j.ijmachtools.2012.06.002.
- [28] Li, S.J., Xu, Q.S., Wang, Z., Hou, W.T., Hao, Y.L., Yang, R., Murr, L.E. (2014). Influence of cell shape on mechanical properties of Ti-6Al-4V meshes fabricated by electron beam melting

- method. *Acta Biomaterialia*, vol. 10, no. 10, p. 4537-4547, DOI:10.1016/j.actbio.2014.06.010.
- [29] Hrabe, N.W., Heinel, P., Flinn, B., Körner, C., Bordia, R.K. (2011). Compression-compression fatigue of selective electron beam melted cellular titanium (Ti-6Al-4V). *Journal of Biomedical Materials Research - Part B Applied Biomaterials*, vol. 99B, no. 2, p. 313-320, DOI:10.1002/jbm.b.31901.
- [30] Liu, Y.J., Li, S.J., Wang, H.L., Hou, W.T., Hao, Y.L., Yang, R., Sercombe, T.B., Zhang, L.C. (2016). Microstructure, defects and mechanical behavior of beta-type titanium porous structures manufactured by electron beam melting and selective laser melting. *Acta Materialia*, vol. 113, p. 56-67, DOI:10.1016/j.actamat.2016.04.029.
- [31] Open cell metal foam - Wikimedia Commons. from https://commons.wikimedia.org/wiki/File:Erg_open_cell_metal_foam.JPG, accessed on 2019-08-13.
- [32] Closed cell metal foam with large cell size - Wikimedia Commons. from https://commons.wikimedia.org/wiki/File:Closed_cell_metal_foam_with_large_cell_size.JPG, accessed on 2019-08-13
- [33] Zettl, B., Mayer, H., Stanzl-Tschegg, S.E., Degischer, H.P. (2000). Fatigue properties of aluminium foams at high numbers of cycles. *Materials Science and Engineering: A*, vol. 292, no. 1, p. 1-7, DOI:10.1016/S0921-5093(00)01033-9.
- [34] Zettl, B., Mayer, H., Stanzl-Tschegg, S.E. (2001). Fatigue properties of Al-1Mg-0.6Si foam at low and ultrasonic frequencies. *International Journal of Fatigue*, vol. 23, no. 7, p. 565-573, DOI:10.1016/S0142-1123(01)00025-1.
- [35] McCullough, K.Y.G., Fleck, N.A. (2000). The stress - life fatigue behaviour of aluminium alloy foams. *Fatigue & Fracture of Engineering Materials & Structures*, vol. 23, p. 199-208, DOI:10.1046/j.1460-2695.2000.00261.x.
- [36] Kashef, S., Asgari, A., Hilditch, T.B., Yan, W., Goel, V.K., Quadbeck, P., Hodgson, P.D. (2013). Fracture mechanics of stainless steel foams. *Materials Science and Engineering: A*, vol. 578, p. 115-124, DOI:10.1016/j.msea.2013.03.062.
- [37] Kashef, S., Asgari, A., Hilditch, T.B., Yan, W., Goel, V.K., Hodgson, P.D. (2011). Fatigue crack growth behavior of titanium foams for medical applications. *Materials Science and Engineering: A*, vol. 528, no. 3, p. 1602-1607, DOI:10.1016/j.msea.2010.11.024.
- [38] Zhao, M., Fan, X., Wang, T.J. (2016). Fatigue damage of closed-cell aluminum alloy foam: Modeling and mechanisms. *International Journal of Fatigue*, vol. 87 p. 257-265, DOI:10.1016/j.ijfatigue.2016.02.009.
- [39] Amsterdam, E., De Hosson, J.Th.M., Onck, P.R. (2006). Failure mechanisms of closed-cell aluminum foam under monotonic and cyclic loading. *Acta Materialia*, vol. 54, no. 17, p. 4465-4472, DOI:10.1016/j.actamat.2006.05.033.
- [40] Fan, X., Zhao, M., Wang, T. (2017). Experimental investigation of the fatigue crack propagation in a closed-cell aluminum alloy foam. *Materials Science and Engineering: A*, vol. 708, p. 424-431, DOI:10.1016/j.msea.2017.09.120.
- [41] Taherishargh, M., Katona, B., Fiedler, T., Orbulov, I.N. (2016). Fatigue properties of expanded perlite/aluminum syntactic foams. *Journal of Composite Materials*, DOI:10.1177/0021998316654305.
- [42] Ingraham, M.D., DeMaria, C.J., Issen, K.A., Morrison, D.J. (2009). Low cycle fatigue of aluminum foam. *Materials Science and Engineering: A*, vol. 504, no. 1-2, p. 150-156, DOI:10.1016/j.msea.2008.10.045.
- [43] Linul, E., Şerban, D.A., Marsavina, L., Kovacic, J. (2017). Low-cycle fatigue behaviour of ductile closed-cell aluminium alloy foams. *Fatigue and Fracture of Engineering Materials and Structures*, vol. 40, no. 4, p. 597-604, DOI:10.1111/ffe.12535.
- [44] Motz, C., Friedl, O., Pippan, R. (2005). Fatigue crack propagation in cellular metals. *International Journal of Fatigue*, vol. 27, no. 10-12, p. 1571-1581, DOI:10.1016/j.ijfatigue.2005.06.044.
- [45] Olurin, O., McCullough, K.Y.G., Fleck, N.A., Ashby, M.F. (2001). Fatigue crack propagation in aluminium alloy foams. *International Journal of Fatigue*, vol. 23, no. 5, p. 375-382, DOI:10.1016/S0142-1123(01)00010-X.
- [46] Hu, X., Wouterson, E.M., Liu, M. (2013). Polymer Foam Technology. *Handbook of Manufacturing Engineering and Technology*, Springer, London, p. 1-35, DOI:10.1007/978-1-4471-4976-7_23-5.
- [47] Zenkert, D., Burman, M. (2009). Tension, compression and shear fatigue of a closed cell polymer foam. *Composites Science and Technology*, vol. 69, no. 6, p. 785-792, DOI:10.1016/j.compscitech.2008.04.017.
- [48] Nakajima, H., Ikeda, T., Hyun, S.K. (2004). Fabrication of lotus-type porous metals and their physical properties. *Advanced Engineering Materials*, vol. 6, no. 6, p. 377-384, DOI:10.1002/adem.200405149.
- [49] Yang, Q.-Q., Liu, Y., Li, Y.-X., Zhang, Y. (2014). Pore structure of unidirectional solidified lotus-type porous silicon. *Transactions of Nonferrous Metals Society of China*, vol. 24, no. 11, p. 3517-3523, DOI:10.1016/S1003-6326(14)63496-8.
- [50] Nakajima, H. (2007). Fabrication, properties and application of porous metals with directional pores. *Progress in Materials Science*, vol. 52, no. 7, p. 1091-1173, DOI:10.1016/j.pmatsci.2006.09.001.
- [51] Vesenjaj, M., Kovačić, A., Tane, M., Borovinšek, M., Nakajima, H., Ren, Z. (2012). Compressive properties of lotus-type porous iron. *Computational Materials Science*, vol. 65, p. 37-43, DOI:10.1016/j.commatsci.2012.07.004.
- [52] Ide, T., Tane, M., Ikeda, T., Hyun, S.K., Nakajima, H. (2006). Compressive properties of lotus-type porous stainless steel. *Journal of Materials Research*, vol. 21, no. 1, p. 185-193, DOI:10.1557/jmr.2006.0016.
- [53] Kovačić, A., Borovinšek, M., Vesenjaj, M., Ren, Z., (2018). Indirect reconstruction of pore morphology for parametric computational characterization of unidirectional porous iron. *Materials*, vol. 11, no. 2, p. 193-204, DOI:10.3390/ma11020193.
- [54] Seki, H., Tane, M., Nakajima, H. (2007). Effects of anisotropic pore structure and fiber texture on fatigue properties of lotus-type porous magnesium. *Journal of Materials Research*, vol. 22, no. 11, p. 3120-3129, DOI:10.1557/jmr.2007.0385.
- [55] Seki, H., Tane, M., Nakajima, H., (2008). Fatigue crack initiation and propagation in lotus-type porous copper. *Materials Transactions*, vol. 49, no. 1, p. 144-150, DOI:10.2320/matertrans.mra2007623.

- [56] Glodež, S., Dervaric, S., Kramberger, J., Šraml, M., (2016). Fatigue crack initiation and propagation in lotus-type porous material. *Fracture and Structural Integrity*, vol. 10, no. 35 p. 152-160, DOI:10.3221/igf-esis.35.18.
- [57] Kramberger, J., Šraml, M., Glodež, S. (2016). Computational study of low-cycle fatigue behaviour of lotus-type porous material. *International Journal of Fatigue*, vol. 92 p. 623-632, DOI:10.1016/j.ijfatigue.2016.02.037.
- [58] Kramberger, J., Šori, M., Šraml, M., Glodež, S. (2017). Multiaxial low-cycle fatigue modelling of lotus-type porous structures. *Engineering Fracture Mechanics*, vol. 174, p. 215-226, DOI:10.1016/j.engfracmech.2016.11.014.
- [59] Hexcel Composites (1999). *Honeycomb Attributes and Properties, A comprehensive guide to standard Hexcel honeycomb materials, configurations, and mechanical properties*. Honeycomb Data Sheets, p. 1-40.
- [60] He, J., Liu, Q., Wu, Z., Jiang, Y. (2018). Geothermal-related thermo-elastic fracture analysis by numerical manifold method. *Energies*, vol. 11, no. 6, p. 1380, DOI:10.3390/en11061380.
- [61] Huang, J.-S., Liu, S.-Y. (2001). Fatigue of honeycombs under in-plane multiaxial loads. *Materials Science and Engineering: A*, vol. 308, no. 1-2, p. 45-52, DOI:10.1016/S0921-5093(00)01996-1.
- [62] Schaffner, G., Guo, X.-D.E., Silva, M.J., Gibson, L.J. (2000). Modelling fatigue damage accumulation in two-dimensional Voronoi honeycombs. *International Journal of Mechanical Sciences*, vol. 42, no. 4, p. 645-656, DOI:10.1016/S0020-7403(99)00031-4.
- [63] Huang, J.S., Lin, J.Y. (1996). Fatigue of cellular materials. *Acta Materialia*, vol. 44, no. 1, p. 289-296, DOI:10.1016/1359-6454(95)00170-4.
- [64] Jen, Y.-M., Lin, H.B. (2013). Temperature-dependent monotonic and fatigue bending strengths of adhesively bonded aluminum honeycomb sandwich beams. *Materials and Design*, vol. 45 p. 393-406, DOI:10.1016/j.matdes.2012.09.028.
- [65] Abbadi, A., Azari, Z., Belouettar, S., Gilgert, J., Freres, P. (2010). Modelling the fatigue behaviour of composites honeycomb materials (aluminium/aramide fibre core) using four-point bending tests. *International Journal of Fatigue*, vol. 32, no. 11, p. 1739-1747, DOI:10.1016/j.ijfatigue.2010.01.005.
- [66] Kanny, K., Mahfuz, H. (2005). Flexural fatigue characteristics of sandwich structures at different loading frequencies. *Composite Structures*, vol. 67, no. 4, p. 403-410, DOI:10.1016/j.compstruct.2004.01.021.
- [67] Belingardi, G., Martella, P., Peroni, L. (2007). Fatigue analysis of honeycomb-composite sandwich beams. *Composites Part A: Applied Science and Manufacturing*, vol. 38, no. 4, p. 1183-1191, DOI:10.1016/j.compositesa.2006.06.007.
- [68] Abbadi, A., Tixier, C., Gilgert, J., Azari, Z., (2015). Experimental study on the fatigue behaviour of honeycomb sandwich panels with artificial defects. *Composite Structures*, vol. 120 p. 394-405, DOI:10.1016/j.compstruct.2014.10.020.
- [69] Belouettar, S., Abbadi, A., Azari, Z., Belouettar, R., Freres, P. (2009). Experimental investigation of static and fatigue behaviour of composites honeycomb materials using four point bending tests. *Composite Structures*, vol. 87, no. 3, p. 265-273, DOI:10.1016/j.compstruct.2008.01.015.
- [70] Hussain, M., Khan, R., Abbas, N. (2019). Experimental and computational studies on honeycomb sandwich structures under static and fatigue bending load. *Journal of King Saud University - Science*, vol. 31, no. 2, p. 222-229, DOI:10.1016/j.jksus.2018.05.012.
- [71] Novak, N., Vesenjaj, M., Ren, Z. (2016). Auxetic Cellular Materials - a Review. *Strojniški vestnik - Journal of Mechanical Engineering*, vol. 62, no. 9, p. 485-493, DOI:10.5545/sv-jme.2016.3656.
- [72] Foster, L., Peketi, P., Allen, T., Senior, T., Duncan, O., Alderson, A. (2018). Application of auxetic foam in sports helmets. *Applied Sciences*, vol. 8, no. 3, p. 354, DOI:10.3390/app8030354.
- [73] Bezazi, A., Scarpa, F. (2009). Tensile fatigue of conventional and negative Poisson's ratio open cell PU foams. *International Journal of Fatigue*, vol. 31, no. 3, p. 488-494, DOI:10.1016/j.ijfatigue.2008.05.005.
- [74] Duarte, I., Vesenjaj, M., Krstulović-Opara, L., Anžel, I., Ferreira, J.M.F. (2015). Manufacturing and bending behaviour of in situ foam-filled aluminium alloy tubes. *Materials and Design*, vol. 66, p. 532-544, DOI:10.1016/j.matdes.2014.04.082.
- [75] Duarte, I., Vesenjaj, M., Krstulović-Opara, L., Ren, Z. (2018). Crush performance of multifunctional hybrid foams based on an aluminium alloy open-cell foam skeleton. *Polymer Testing*, vol. 67, p. 246-256, DOI:10.1016/j.polymeresting.2018.03.009.
- [76] Meraghni, F., Desrumaux, F., Benzeggagh, M.L. (1999). Mechanical behaviour of cellular core for structural sandwich panels. *Composites Part A: Applied Science and Manufacturing*, vol. 30, no. 6, p. 767-779, DOI:10.1016/S1359-835X(98)00182-1.
- [77] Dannemann, M., Kucher, M., Kunze, E., Modler, N., Knobloch, K., Enghardt, L., Sarradj, E., Höschler, K. (2018). Experimental study of advanced helmholtz resonator liners with increased acoustic performance by utilising material damping effects. *Applied Sciences*, vol. 8, no. 10, p. 1923, DOI:10.3390/app8101923.
- [78] Jen, Y.-M., Teng, F.-L., Teng, T.-C. (2014). Two-stage cumulative bending fatigue behavior for the adhesively bonded aluminum honeycomb sandwich panels. *Materials & Design*, vol. 54, p. 805-813, DOI:10.1016/j.matdes.2013.09.010.
- [79] Jen, Y.-M., Chang, L.-Y. (2009). Effect of thickness of face sheet on the bending fatigue strength of aluminum honeycomb sandwich beams. *Engineering Failure Analysis*, vol. 16, no. 4, p. 1282-1293, DOI:10.1016/j.engfailanal.2008.08.004.
- [80] Jen, Y.-M., Ko, C.-W., Lin, H.-B. (2009). Effect of the amount of adhesive on the bending fatigue strength of adhesively bonded aluminum honeycomb sandwich beams. *International Journal of Fatigue*, vol. 31, no. 3, p. 455-462, DOI:10.1016/j.ijfatigue.2008.07.008.

Vsebina

Strojniški vestnik - Journal of Mechanical Engineering

letnik 65, (2019), številka 9
Ljubljana, september 2019
ISSN 0039-2480

Izhaja mesečno

Razširjeni povzetki (extended abstracts)

Janez Luznar, Janko Slavič, Miha Boltežar: Simuliranje strukturnega hrupa pri PWM vzbujanju s pomočjo razširjene metode rekonstrukcije magnetnega polja in modalne dekompozicije	SI 59
Mario Sokac, Djordje Vukelic, Zivana Jakovljevic, Zeljko Santosi, Miodrag Hadzistevic, Igor Budak: Mehka hibridna metoda za rekonstrukcijo 3D-modelov na osnovi podatkov CT/MRI	SI 60
Wojciech Depczyński: Izbrane mikrostrukturne in mehanske lastnosti kovinske pene z odprto poroznostjo	SI 61
Shahin Ghanbari, Kourosh Javaherdeh: Eksperimentalna analiza turbulentnega konvektivnega prenosa toplote in tlačnega padca v kolobarjih z nenevtonskim nanofluidom z nanoporoznim grafenom	SI 62
Min Song, Hongliang Wang, Haiou Liu, Pai Peng, Xianhui Wang, Dawei Pi, Chen Yang, Gang He: Dvonivojsko vodenje sklopke mehanskega samodejnega menjalnika med speljevanjem gospodarskega vozila	SI 63
Branko Nečemer, Matej Vesenjaj, Srečko Glodež: Utrujanje celičnih struktur - pregled	SI 64

Simuliranje strukturnega hrupa pri PWM vzbujanju s pomočjo razširjene metode rekonstrukcije magnetnega polja in modalne dekompozicije

Janez Luznar¹ – Janko Slavič^{2,*} – Miha Boltežar²

¹Domel, d.o.o., Slovenija

²Univerza v Ljubljani, Fakulteta za strojništvo, Slovenija

Cilji raziskave so:

- Predstaviti metodo hitrega izračuna hrupa pri PWM vzbujanju, ki temelji na nedavno predstavljeni razširjeni metodi rekonstrukcije magnetnega polja (EFRM).
- Predstavljena metoda naj omogoča učinkovit in točen izračun strukturnega hrupa pri različnih PWM vzbujanjih.
- Z uporabo predstavljene metode je možen izračun parametrične analize hrupa pri različnih PWM preklopnih frekvencah, ki vodi do 30 dB(A) razlike v celotni ravni zvočne moči.

Hitrost in navor elektronsko komutiranih motorjev krmilimo s pomočjo pulzno-širinske modulacije (PWM). Slednja vpliva na fazne tokove motorja, kjer se poleg osnovne, zelene frekvenčne komponente, pojavijo tudi številni visoko-frekvenčni preklopni harmoniki. Ti se odražajo v vzbujevalnih elektromagnetnih silah, vibracijskem odzivu in končnemu strukturnemu hrupu. Slednji predstavlja multifizikalni problem, ki ga lahko simuliramo z uporabo MKE analiz za popis električne, elektromagnetne, strukturne in akustične domene. Tak pristop je računsko neučinkovit in zato neprimeren za parametrične analize, s katerimi bi lahko določili ustrezno PWM preklopno frekvenco za zmanjšanje hrupa.

Metodologija raziskovanja omenjene problematike obsega pregled literature in numerično modeliranje. Numeričen model opisuje multifizikalno dogajanje elektronsko komutiranega motorja, ki vključuje naslednja znanstvena področja: elektroniko, elektromagnetiko, strukturno dinamiko in akustiko. Na podlagi pregleda literature omenjenih področij in upoštevanja zadnjih dognanj na področju numeričnega modeliranja hrupa je razvita in predlagana metoda hitrega simuliranja hrupa pri PWM vzbujanju.

Predstavljena metoda hitrega simuliranja strukturnega hrupa pri PWM vzbujanju je validirana s pomočjo komercialnega paketa ANSYS 18.1. Glavna prednost predstavljene metode je računsko učinkovitost, zaradi česar je omogočen izračun parametričnih analiz. Slednjo smo izvedli za 197 različnih PWM vzbujanj, ki jih s predstavljenimi metodo izračunamo v 10 minutah, medtem ko bi z uporabo le komercialnih orodij izračun trajal več kot 600 dni (tj. bistveno daljši čas). S pomočjo parametrične analize smo ugotovili, da ustrezna izbira PWM preklopne frekvence lahko zmanjša celotno raven zvočne moči tudi do 30 dB(A).

Predstavljena metoda hitrega izračuna hrupa pri PWM vzbujanju temelji na uporabi EFRM, katera zanemara križno korelacijo magnetenja d in q osi. V nadaljevanju bi lahko raziskali še detajlni vpliv te zanemaritve in možnosti izboljšanja.

Detajlna dinamska sklopljenost med PWM vzbujanjem in strukturnim hrupom motorja je bila nedavno raziskana že eksperimentalno, v tem članku pa je predstavljena še možnost numeričnega simuliranja. Najprej je preučen konvencionalni pristop z uporabo MKE analiz, ki je pri podobnih raziskavah pogosto uporabljen, a je za primer PWM vzbujanja računsko zelo zahteven in posledično neprimeren za parametrične analize. Zato smo razvili in validirali metodo hitrega izračuna hrupa pri različnih PWM vzbujanjih, ki temelji na uporabi razširjene metode rekonstrukcije magnetnega polja (EFRM) za pohitritev tranzientnih magnetnih MKE analiz. V primerjavi z drugimi raziskavami smo tako prvi vpeljali EFRM za reševanje vibroakustičnih problemov elektronsko komutiranih motorjev. Uporabljena EFRM v kombinaciji z metodo modalne dekompozicije omogoča računsko učinkovito simuliranje strukturnega hrupa pri PWM vzbujanju in posledično tudi numerično določitev dinamske sklopljenosti med elektronsko komutacijo in strukturnim hrupom.

Ključne besede: elektromagnetne sile, modalna dekompozicija, preklopna frekvenca PWM, razširjena metoda rekonstrukcije magnetnega polja, strukturni hrup

Mehka hibridna metoda za rekonstrukcijo 3D-modelov na osnovi podatkov CT/MRI

Mario Sokac¹ – Djordje Vukelic^{1,*} – Zivana Jakovljevic² – Zeljko Santosi¹ – Miodrag Hadzistevic¹ – Igor Budak¹

¹Univerza v Novem Sadu, Fakulteta tehniških znanosti, Srbija

²Univerza v Beogradu, Fakulteta za strojništvo, Srbija

Segmentacija neizboljšanih medicinskih posnetkov je lahko zelo težavno in zamudno opravilo. Segmentacija in izločanje površin zaradi nedoslednosti ali prisotnosti šuma na medicinskih posnetkih tudi ne daje vedno natančnih rezultatov. To je lahko posledica nejasnih struktur na slabo prikazanih medicinskih posnetkih ali pa prisotnosti homogenih obdajajočih struktur. Za natančnejšo segmentacijo je zato potrebna predobdelava in izboljšanje kakovosti posnetkov. V raziskavi je podan predlog hibridne metode za izboljšanje natančnosti segmentacije rekonstruiranih 3D-modelov iz podatkov posnetkov, pridobljenih z računalniško tomografijo/magnetno resonanco (CT/MRI).

Točna segmentacija posnetkov CT/MRI ima pomembno vlogo pri točni izvedbi diagnostičnega postopka. Te sodobne naprave zagotavljajo podatkovne množice 3D-posnetkov, ki vsebujejo točne informacije za ustvarjanje modelov 3D-površin. Podan je predlog polsamodejne hibridne metode na osnovi kombinacije razporejanja v gruče z mehko metodo k-središč (FCM) in rasti regij (RG). Pristop uporablja FCM kot prvi korak predobdelave za klasifikacijo in izboljšanje posnetkov z dodeljevanjem slikovnih točk gručam, do katerih imajo največjo pripadnost, ter ročno izbiro karte intenzivnosti pripadnosti z najboljšim kontrastom. Temu sledi samodejna izbira semen za RG z novim parametrom – standardno deviacijo (STD) intenzivnosti slikovnih točk. Ta poteka na osnovi izbire začetnega semena v regiji z maksimalno vrednostjo STD.

Informacije, zbrane iz medicinskih posnetkov, imajo velik vpliv na pravilno diagnostično obravnavo in zdravljenje. Pri zajemu 2D-posnetkov se lahko izgubi nekaj informacij, ta izguba informacij pa zmanjša kakovost posnetka in, kar je še bolj pomembno, vpliva na točnost segmentacije in geometrijske rekonstrukcije. Preboj dodatnih izdelovalnih tehnologij na področju medicine je omogočil izdelavo fizičnih anatomskih struktur, ki je v veliki meri odvisna od vhodnih podatkov za oblikovanje vsadkov po meri pacienta in medicinskih modelov. Ustrezna segmentacija posnetkov in rekonstrukcija 3D-modelov je zato ključna za njihovo uporabo na tem področju. Razvoj nove metode za izboljšanje posnetkov in točno segmentacijo omogoča izločanje točnejših informacij iz medicinskih posnetkov.

Vrednotenje zmogljivosti predlaganih metod je bilo opravljeno na dveh podatkovnih množicah 3D-posnetkov, ustvarjenih po postopku računalniške tomografije s šopastim izvorom žarkov (CBCT), in na dveh podatkovnih množicah 3D-posnetkov MRI. Povprečne stopnje občutljivosti in točnosti za podatkovni množici CBCT 1 in CBCT 2 so bile 99 % in 98,4 % ter 47,2 % in 89,9 %. Povprečne stopnje občutljivosti za podatkovni množici MRI 1 in MRI 2 so bile 99,1 % in 100 % ter 75,6 % in 99,6 %. Povprečne vrednosti koeficienta Dice in Jaccardovega indeksa za podatkovni množici CBCT1 in CBCT 2 so bile 95,88 in 0,88 ter 0,6 in 0,51, za podatkovni množici MRI 1 in MRI 2 pa 0,96 in 0,93 ter 0,81 in 0,7. S tem je bila potrjena visoka natančnost predlagane metode.

Prihodnje delo bo usmerjeno v dodatne izboljšave pri samodejnem določanju števila gruč po metodi FCM in tako bodo odpravljeni uporabniški posegi v tej fazi obdelave. Pripravljen bo tudi do uporabnika prijaznejši grafični uporabniški vmesnik za predlagano metodo, ki bo omogočil bolj interaktivno uporabo. Čeprav so bili v tej študiji uporabljeni samo posnetki naprav CBCT in MRI, pa s tem ni omejena uporabnost predlagane metode tudi za posnetke drugih slikovnih sistemov, ki bodo vključeni v prihodnje raziskave.

Novost v tem članku je razvoj nove metode za samodejno izbiro začetnih semen za RG, ki vključuje vrednost STD kot merilo za izbiro semen. To v kombinaciji z izboljšavami slike na osnovi FCM zaokroža celoten proces segmentacije podatkovnih množic 3D-posnetkov. Predlagana metoda je namenjena izboljšavi slabo vidnih struktur v podatkovnih množicah CBCT in MRI, s tem pa izboljšuje segmentacijo in izločanje površin. S kombiniranjem obeh metod se je izboljšala točnost segmentacije, kar potrjujejo tudi različni kazalniki, kot so koeficient Dice, Jaccardov indeks, občutljivost in točnost.

Ključne besede: razporejanje v gruče z mehko metodo k-središč, rast regij, segmentacija posnetkov, 3D-model površine, računalniška tomografija s snopastim šopom žarkov, slikanje z magnetno resonanco

Izbrane mikrostrukturne in mehanske lastnosti kovinske pene z odprto poroznostjo

Wojciech Depczyński*

Tehniška univerza Kielce, Fakulteta za mehatroniko in strojništvo, Poljska

Članek obravnava pripravo kovinskih pen z odprto poroznostjo po postopkih metalurgije prahov. Cilj preizkusov, ki so bili opravljeni na posebnem preizkuševališču, je bil opredelitev sposobnosti pen na osnovi Fe za absorpcijo udarcev.

Tehnologija priprave pene vključuje dodajanje oksida, ki se enostavno reducira z vodikom. Oksid pri tem odigra vlogo penila in zaseda prostor v strukturi. V študiji je bil uporabljen Fe (III) oksid, ki med sintranjem reagira z nadzorovano atmosfero. Ko se z vodikom iz disociiranega amoniaka reducira v železo, v materialu ostanejo praznine.

Naslednji pomembni dejavnik pri izdelavi celične strukture je prisotnost vodne pare in CO oz. CO₂. Ti plini delujejo kot penilna sredstva: ko se sproščajo iz prostorov, ki jih zaseda sintran prah, ustvarjajo odprte povezane celice.

Kot kovinski prekursorji so bili uporabljeni prahovi, ki so prosto dostopni na trgu. Izbrane so bile štiri zmesi z oznakami ASC100.29, ASC100.29 + C, DISTALOY SE in DISTALOY SE + C. Vsem sta bila dodana baker kot katalizator za difuzijo in Fe (III) oksid, ki deluje kot penilno sredstvo in zaseda prostor. Vse sestavine zmesi so bile v obliki prahov. Zmesi prahov niso bile stisnjene in na zrna je vplivala samo sila težnosti. Preizkušanci so bili po sintranju preneseni v hladilno komoro. Visoka temperatura in prisotnost vodika sta prispevali k redukciji železovega (III) oksida, v trdni strukturi pa so se oblikovali prazni prostori.

Določitev povprečne velikosti por zaradi njihove naključne porazdelitve ni preprosta naloga. Premer por, ki je znašal približno 100 μm, je bil določen na osnovi meritev OM s programsko opremo Nikon NIS-Element AR. Pri ocenjevanju velikosti por je bilo uporabljeno Cavalieri-Hacquetovo načelo. Poroznost penastih materialov je bila določena z optično mikroskopijo, za ASC, ASC + C, SE in SE + C pa je znašala 67,9, 77,8, 75,7 in 80,3. Analiza gibanja udarnega kladiva z maso 2,3 kg je bila opravljena s programsko opremo TEMA Motion. Na osnovi podatkov programske opreme TEMA Motion je bil določen pojemek kladiva, ki je znašal približno 8000 m/s² oz. 800 G. Hitrost v trenutku udarca je bila 11 m/s, udarec je trajal približno 25,5 ms in kinetična energija udarca je bila 139,15 J. Vsak preizkušaneec je absorbiral drugačno količino kinetične energije udarca, odvisno od lastnosti pene.

Primerjava rezultatov udarnega preizkusa je težavna, ker ne obstajajo standardi za meritve absorpcije energije in interpretacijo rezultatov na področju pen z odprto in zaprto poroznostjo ter sintaktičnih pen. Lažja je primerjava rezultatov statičnih preizkusov, kot so npr. preizkusi kvazistatičnega stiskanja. Opisani rezultati dinamičnih preizkusov so bili pridobljeni pri razmeroma majhni energiji udarcev (pod 140 J), ki izhaja iz zasnove preizkuševališča.

Obravnavani materiali so bili izdelani z nekonvencionalno tehniko sintranja in imajo edinstvene lastnosti. Pomemben korak procesa priprave je redukcija Fe (III) oksida, ki deluje kot penilo in zaseda prostor. Analizirane so bile štiri zmesi prahov: ASC100.29, ASC100.29 + C, DISTALOY SE in DISTALOY SE + C. Preizkusi so bili opravljeni na posebnem preizkuševališču in ugotovljeno je bilo, da imajo kovinske pene na osnovi Fe zaradi velike poroznosti visoko sposobnost absorpcije udarcev. Relacije med lastnostma bodo podrobneje preučene v prihodnjih raziskavah. Pene na osnovi Fe z odprto poroznostjo, izdelane na predstavljeni način, bodo uporabne v aplikacijah kot so lahke konstrukcije, sistemi za disipacijo in absorpcijo energije, katalizatorji in prenosniki toplote.

Ključne besede: kovinske pene z odprto poroznostjo, pene na osnovi Fe, redukcija kovinskih oksidov, tehnika zasedanja prostora, disipacija energije

Eksperimentalna analiza turbulentnega konvektivnega prenosa toplote in tlačnega padca v kolobarjih z nenevtonskim nanofluidom z nanoporoznim grafenom

Shahin Ghanbari – Kouros Javaherdeh*

Univerza v Gilanu, Fakulteta za strojništvo, Iran

Predmet raziskovalne naloge je bila preiskava možnosti za izboljšanje koeficienta turbulentne konvektivne toplotne prenosnosti in tlačnega padca nenevtonskega nanofluida z nanoporoznim grafenom v območju razvoja toka v cevi kolobarjastega prereza. Nanofluid je bil pripravljen z različnimi koncentracijami nanoporoznega grafena 0,05 ut. %, 0,1 ut. % in 0,2 ut. % v vodni raztopini karboksimetil celuloze (CMC).

Ovrednotene so bile vse termofizikalne in reološke lastnosti in za vse vzorce je bilo ugotovljeno psevdoplastično reološko obnašanje.

Iz rezultatov sledi sklep, da je z dodatkom 0,2 ut. % nanoporoznega grafena v osnovni fluid mogoče izboljšati toplotno prevodnost in toplotno prestopnost za 12,4 oz. 39,4 %. Trend izboljšanja je pri koncentracijah pod 0,1 ut. % skoraj linearen, nato pa stopnja izboljšanja znatno upade. Rezultati so poleg tega pokazali, da se pri uporabi 0,05 in 0,1 ut. % nanoporoznega grafena faktor toplotne učinkovitosti (TPF) poveča za 8,7 oz. 16,7 %, s podvojitvijo koncentracije nanodelcev z 0,1 na 0,2 ut. % pa vrednosti TPF ni bilo mogoče izboljšati. Ob upoštevanju tlačnega padca se je toplotna prestopnost celo zmanjšala za 2,5 %.

S povečanjem Reynoldsovega števila se je toplotna prestopnost pri vseh vzorcih povečala. Kot robni pogoj je bil uporabljen konstanten toplotni tok na notranji steni z izolirano zunanjo steno. Nanofluidi so bili pripravljene z dispergiranjem različnih koncentracij nanoporoznega grafena v vodni raztopini CMC. Nanofluidi, pripravljene v štiriurnem postopku ultrazvočne obdelave z 0,2 ut. % CMC v vlogi surfaktanta, izkazujejo dobro stabilnost. Z dodatkom 0,05 ut. %, 0,1 ut. % in 0,2 ut. % nanoporoznega grafena v osnovno raztopino se je toplotna prestopnost povečala za 16,1 %, 30,3 % oz. 39,4 %. Vrednost toplotne prestopnosti se do koncentracije 0,1 ut. % povečuje praktično linearno, nato pa stopnja izboljšanja upade. Upad stopnje izboljšanja toplotne prestopnosti pri višjih koncentracijah ter vplivi nasičenja, sedimentacije in povečanja tlačnega padca v nenevtonski tekočini privedejo do tega, da podvojitve koncentracije z 0,1 ut. % na 0,2 ut. % toplotne učinkovitosti ne izboljša, ampak jo celo zmanjša za 2,5 %.

Kljub temu, da je toplotna prestopnost nanofluida z 0,2 ut. % nanodelcev pri danem Reynoldsovem številu v povprečju za 9,1 % večja kot pri vzorcu z 0,1 ut. % nanodelcev, so meritve v cevi kolobarjastega prereza pokazale, da ima ob upoštevanju tlačnega padca in rabe energije zaradi optimalne vsebnosti nanoporoznega grafena prednost nanofluid z 0,1 ut. % nanodelcev.

Ključne besede: nanoporozni grafen, nanofluid, cev kolobarjastega prereza, faktor toplotne učinkovitosti, tlačni padec

Dvonivojsko vodenje sklopke mehanskega samodejnega menjalnika med speljevanjem gospodarskega vozila

Min Song¹ – Hongliang Wang^{1,*} – Haiou Liu² – Pai Peng¹ –
Xianhui Wang¹ – Dawei Pi¹ – Chen Yang¹ – Gang He¹

¹Znanstveno-tehniška univerza v Nanjingu, Oddelek za strojništvo, Kitajska

²Šola za strojništvo in avtomobilsko tehniko, Inštitut za tehnologijo v Pekingu, Kitajska

Regulacija vklapljanja sklopke mehanskega samodejnega menjalnika med speljevanjem vozila pomembno vpliva na varnost, udobje, življenjsko dobo, rabo energije in emisije. Vse obstoječe strategije vodenja uporabljajo enonivojsko regulacijo, ki pa vodi do slabe prilagodljivosti na temperaturne spremembe. V članku je predstavljena dvonivojska strategija vodenja za izboljšanje zmogljivosti speljevanja vozila na podlagi samodejnega aktuatorja. Preučene so lastnosti krmilnika vrtilne frekvence dizelskega motorja in podan je opis načela delovanja in modela samodejnega aktuatorja. Zasnovana in opravljena je bila simulacija speljevanja vozila. Dvonivojska strategija vodenja je bila končno preverjena še na eksperimentalnem vozilu. Rezultati eksperimentov in simulacije kažejo, da dvonivojska strategija vodenja omogoča krajši čas speljevanja, manj sunkov in manjše torni delo, s čimer je bila dokazana uspešnost in uporabnost te strategije. Zasnovana je bila dvonivojska strategija vodenja na osnovi samodejnega aktuatorja sklopke in regulatorja. Temperaturne spremembe vplivajo na vklapljanje sklopke med procesom zagona vozila. Rezultati primerjave potrjujejo prednosti predstavljenega pristopa z vidika časa speljevanja, sunkov in tornega dela. Eksperimenti s pravim vozilom so še dodatno potrdili predlagano strategijo vodenja.

V članku je predstavljena zasnova dvonivojske strategije vodenja za izboljšanje zmogljivosti speljevanja vozila na podlagi samodejnega aktuatorja sklopke. Dejanska hitrost vklapljanja sklopke vedno odstopa od želene hitrosti zaradi okoljskih dejavnikov, kot so temperaturne spremembe.

Rezultati simulacij in eksperimentov so pokazali, da je z uporabo dvonivojske strategije vodenja mogoče zmanjšati vpliv temperaturnih sprememb na zmogljivost speljevanja.

Rezultati simulacij in eksperimentov kažejo tudi na izboljšavo zmogljivosti speljevanja pri dvonivojski strategiji vodenja v primerjavi z enonivojsko strategijo.

Možna smer prihodnjega dela bo razvoj samoučeče regulacije z nevronskimi mrežami za izboljšanje dvonivojske strategije vodenja. Za dodatno izboljšanje zmogljivosti speljevanja vozila bi bilo mogoče upoštevati tudi spremembe obrabe in temperature tornih oblog lamel sklopke.

Ključne besede: mehanski samodejni menjalnik, postopek speljevanja, regulacija vklapljanja sklopke, dvonivojsko vodenje

Utrujanje celičnih struktur - pregled

Branko Nečemer* – Matej Vesenjāk – Srečko Glodež

Univerza v Mariboru, Fakulteta za strojništvo, Slovenija

Celične strukture se zaradi ugodne kombinacije mehanskih in fizikalnih lastnosti vse pogosteje uporabljajo v sodobni inženirski praksi. V zgodnji fazi raziskav so bili najprej preučevani naravni celični materiali, kot so les, kosti, satovje čebeljih panjev ipd., ki so po svoji zasnovi porozni, kar je vzpodbudilo zanimanje številnih raziskovalcev po celotnem svetu. V samem začetku raziskovanja celičnih materialov je bilo razvitih veliko različnih vrst celičnih struktur, ki jih lahko v grobem delimo na odprte in zaprte celične strukture, ter glede na razporeditev por/celice na urejene in neurejene celične strukture. Med celične strukture spadajo tudi avksetične celične strukture, katerih glavna posebnost je negativno Poissonovo razmerje. Slednje je posledica rotiranja medceličnih povezav, ko se zaradi delovanja zunanje obremenitve spremeni volumen obravnavane strukture. Do sedaj so bile izvedene številne študije mehanske karakterizacije ter nekaj študij z vidika utrujanja celičnih struktur. Zaradi lažjega pregleda področja z vidika utrujanja celičnih struktur je bil izdelan pregledni članek, v katerem so zbrane številne študije na temo utrujanja celičnih struktur. Pregled je osredotočen na nekatere tipične in pogosto uporabljene celične strukture, ki so razdeljene v tri glavne skupine: (1) predhodno načrtovane celične strukture, (2) nepravilne celične strukture in (3) kompoziti s celičnimi jedri. Za vsako skupino je predstavljena trenutna proizvodna tehnika za izdelavo določene celične strukture, ki pripada tej skupini. Poleg tega je za analizirane celične strukture razloženo stanje tehnike utrujanja. Za prvo skupino (predhodno načrtovane celične strukture) so eksperimentalne raziskave pokazale, da oblika osnovne celice kot tudi proizvodna tehnologija le-te pomembno vplivata na mehanske lastnosti in utrujanje obravnavanih celičnih struktur. V okviru druge skupine so analizirane zaprte in odprte celične pene, lotus celične strukture, celične strukture satovja in avksetične celične strukture. Na podlagi številnih raziskav so bili sprejeti naslednji sklepi:

- razpoložljive informacije z vidika utrujanja zaprtih in odprtih celičnih pen so zelo omejene. Hitrost rasti utrujenostne razpoke je zelo odvisna od oblike celice in mikrostrukture osnovnega materiala, iz katerega so izdelane pene.
- Eksperimentalne in numerične raziskave utrujanja lotus poroznih materialov so pokazale, da je trajna dinamična trdnost v smeri vzporedno z vzdolžno osjo por višja od trajne dinamične trdnosti v pravokotni smeri. Poleg tega porazdelitev por pomembno vpliva na mehansko obnašanje z vidika utrujanja. Utrujenostne razpoke se najprej pojavijo v okolici velikih por in se nato širijo med porami v smeri največjih napetosti.
- Eksperimentalni in numerični rezultati celičnih struktur satovja kažejo, da je naključno usmerjeno satovje bolj občutljivo na ciklično obremenitev v primerjavi z urejeno strukturo satovja. Povečana občutljivost izhaja iz porazdelitve napetosti v celičnih stenah satovja.
- Na področju utrujanja avksetičnih celičnih struktur so bile izvedene zelo omejene preiskave. Začetne raziskave na tem področju so pokazale, da imajo avksetične pene višjo absorpcijo energije pri tlačni ciklični obremenitvi v primerjavi s konvencionalnimi penami.

V okviru tretje skupine (kompoziti s celičnimi jedri) so razpoložljivi eksperimentalni rezultati povezani s sendvič strukturami, katerih jedro predstavlja celično satovje. Rezultati so pokazali, da morfologija in topologija pomembno vplivata na življenjsko dobo sendvič strukture pri konstantni obremenitvi.

Na podlagi ugotovitev v tem pregledu lahko sklepamo, da celične strukture kažejo velik potencial, da postanejo pomembni konstrukcijski materiali prihodnosti z nadaljnjim razvojem aditivnih proizvodnih tehnologij ali z uvedbo nekaterih novih, stroškovno ugodnejših proizvodnih tehnologij. Poznavanje obnašanja takih struktur z vidika utrujanja je relativno slabo in bi moralo biti predmet nadaljnjih raziskav. Slednje je še posebej povezano z avksetičnimi celičnimi strukturami, ki zaradi svojih naprednih fizikalnih lastnosti zagotavljajo veliko možnosti za njihovo široko uporabo. Avksetične celične strukture imajo tudi velik potencial v medicinskih aplikacijah, kot so srčno-žilne opornice. S tega vidika bi lahko bila priložnost za nadaljnje raziskovalno delo zasnovane nove geometrije kardiovaskularnih razširitvenih opornic, izdelanih iz avksetičnih celičnih struktur in nadaljnje preiskave utrujenosti teh struktur.

Ključne besede: celične strukture, avksetične celične strukture, odprte in zaprte celične pene, utrujanje, dinamična trdnost, rast razpoke

Information for Authors

All manuscripts must be in English. Pages should be numbered sequentially. The manuscript should be composed in accordance with the Article Template given above. The maximum length of contributions is 10 pages. Longer contributions will only be accepted if authors provide justification in a cover letter. For full instructions see the Information for Authors section on the journal's website: <http://en.sv-jme.eu>.

SUBMISSION:

Submission to SV-JME is made with the implicit understanding that neither the manuscript nor the essence of its content has been published previously either in whole or in part and that it is not being considered for publication elsewhere. All the listed authors should have agreed on the content and the corresponding (submitting) author is responsible for having ensured that this agreement has been reached. The acceptance of an article is based entirely on its scientific merit, as judged by peer review. Scientific articles comprising simulations only will not be accepted for publication; simulations must be accompanied by experimental results carried out to confirm or deny the accuracy of the simulation. Every manuscript submitted to the SV-JME undergoes a peer-review process.

The authors are kindly invited to submit the paper through our web site: <http://ojs.sv-jme.eu>. The Author is able to track the submission through the editorial process - as well as participate in the copyediting and proofreading of submissions accepted for publication - by logging in, and using the username and password provided.

SUBMISSION CONTENT:

The typical submission material consists of:

- A **manuscript** (A PDF file, with title, all authors with affiliations, abstract, keywords, highlights, inserted figures and tables and references),
 - Supplementary files:
 - a **manuscript** in a WORD file format
 - a **cover letter** (please see instructions for composing the cover letter)
 - a ZIP file containing **figures** in high resolution in one of the graphical formats (please see instructions for preparing the figure files)
 - possible **appendices** (optional), cover materials, video materials, etc.
- Incomplete or improperly prepared submissions will be rejected with explanatory comments provided. In this case we will kindly ask the authors to carefully read the Information for Authors and to resubmit their manuscripts taking into consideration our comments.

COVER LETTER INSTRUCTIONS:

Please add a **cover letter** stating the following information about the submitted paper:

1. **Paper title, list of authors and their affiliations.**
2. **Type of paper:** original scientific paper (1.01), review scientific paper (1.02) or short scientific paper (1.03).
3. A **declaration** that neither the manuscript nor the essence of its content has been published in whole or in part previously and that it is not being considered for publication elsewhere.
4. State the **value of the paper** or its practical, theoretical and scientific implications. What is new in the paper with respect to the state-of-the-art in the published papers? Do not repeat the content of your abstract for this purpose.
5. We kindly ask you to suggest at least two **reviewers** for your paper and give us their names, their full affiliation and contact information, and their scientific research interest. The suggested reviewers should have at least two relevant references (with an impact factor) to the scientific field concerned; they should not be from the same country as the authors and should have no close connection with the authors.

FORMAT OF THE MANUSCRIPT:

The manuscript should be composed in accordance with the Article Template. The manuscript should be written in the following format:

- A **Title** that adequately describes the content of the manuscript.
- A list of **Authors** and their **affiliations**.
- An **Abstract** that should not exceed 250 words. The Abstract should state the principal objectives and the scope of the investigation, as well as the methodology employed. It should summarize the results and state the principal conclusions.
- 4 to 6 significant **key words** should follow the abstract to aid indexing.
- 4 to 6 **highlights**; a short collection of bullet points that convey the core findings and provide readers with a quick textual overview of the article. These four to six bullet points should describe the essence of the research (e.g. results or conclusions) and highlight what is distinctive about it.
- An **Introduction** that should provide a review of recent literature and sufficient background information to allow the results of the article to be understood and evaluated.
- A **Methods** section detailing the theoretical or experimental methods used.
- An **Experimental section** that should provide details of the experimental set-up and the methods used to obtain the results.
- A **Results** section that should clearly and concisely present the data, using figures and tables where appropriate.
- A **Discussion** section that should describe the relationships and generalizations shown by the results and discuss the significance of the results, making comparisons with previously published work. (It may be appropriate to combine the Results and Discussion sections into a single section to improve clarity.)
- A **Conclusions** section that should present one or more conclusions drawn from the results and subsequent discussion and should not duplicate the Abstract.
- **Acknowledgement** (optional) of collaboration or preparation assistance may be included. Please note the source of funding for the research.
- **Nomenclature** (optional). Papers with many symbols should have a nomenclature that defines all symbols with units, inserted above the references. If one is used, it must contain all the symbols used in the manuscript and the definitions should not be repeated in the text. In all cases, identify the symbols used if they are not widely recognized in the profession. Define acronyms in the text, not in the nomenclature.
- **References** must be cited consecutively in the text using square brackets [1] and collected together in a reference list at the end of the manuscript.
- **Appendix(-ices)** if any.

SPECIAL NOTES

Units: The SI system of units for nomenclature, symbols and abbreviations should be followed closely. Symbols for physical quantities in the text should be written in italics (e.g. v , T , n , etc.). Symbols for units that consist of letters should be in plain text (e.g. ms^{-1} , K, mm, etc.). Please also see: <http://physics.nist.gov/cuu/pdf/sp811.pdf>.

Abbreviations should be spelt out in full on first appearance followed by the abbreviation in parentheses, e.g. variable time geometry (VTG). The meaning of symbols and units

belonging to symbols should be explained in each case or cited in a **nomenclature** section at the end of the manuscript before the References.

Figures (figures, graphs, illustrations digital images, photographs) must be cited in consecutive numerical order in the text and referred to in both the text and the captions as Fig. 1, Fig. 2, etc. Figures should be prepared without borders and on white grounding and should be sent separately in their original formats. If a figure is composed of several parts, please mark each part with a), b), c), etc. and provide an explanation for each part in Figure caption. The caption should be self-explanatory. Letters and numbers should be readable (Arial or Times New Roman, min 6 pt with equal sizes and fonts in all figures). Graphics (submitted as supplementary files) may be exported in resolution good enough for printing (min. 300 dpi) in any common format, e.g. TIFF, BMP or JPG, PDF and should be named Fig1.jpg, Fig2.tif, etc. However, graphs and line drawings should be prepared as vector images, e.g. CDR, AI. Multi-curve graphs should have individual curves marked with a symbol or otherwise provide distinguishing differences using, for example, different thicknesses or dashing.

Tables should carry separate titles and must be numbered in consecutive numerical order in the text and referred to in both the text and the captions as Table 1, Table 2, etc. In addition to the physical quantities, such as t (in italics), the units [s] (normal text) should be added in square brackets. Tables should not duplicate data found elsewhere in the manuscript. Tables should be prepared using a table editor and not inserted as a graphic.

REFERENCES:

A reference list must be included using the following information as a guide. Only cited text references are to be included. Each reference is to be referred to in the text by a number enclosed in a square bracket (i.e. [3] or [2] to [4] for more references; do not combine more than 3 references, explain each). No reference to the author is necessary.

References must be numbered and ordered according to where they are first mentioned in the paper, not alphabetically. All references must be complete and accurate. Please add DOI code when available. Examples follow.

Journal Papers:

Surname 1, Initials, Surname 2, Initials (year). Title. Journal, volume, number, pages, DOI code.

- [1] Hackenschmidt, R., Alber-Laukant, B., Rieg, F. (2010). Simulating nonlinear materials under centrifugal forces by using intelligent cross-linked simulations. *Strojniški vestnik - Journal of Mechanical Engineering*, vol. 57, no. 7-8, p. 531-538, DOI:10.5545/sv-jme.2011.013.

Journal titles should not be abbreviated. Note that journal title is set in italics.

Books:

Surname 1, Initials, Surname 2, Initials (year). Title. Publisher, place of publication.

- [2] Groover, M.P. (2007). *Fundamentals of Modern Manufacturing*. John Wiley & Sons, Hoboken.

Note that the title of the book is italicized.

Chapters in Books:

Surname 1, Initials, Surname 2, Initials (year). Chapter title. Editor(s) of book, book title. Publisher, place of publication, pages.

- [3] Carbone, G., Ceccarelli, M. (2005). Legged robotic systems. Kordić, V., Lazinica, A., Merdan, M. (Eds.), *Cutting Edge Robotics*. Pro literatur Verlag, Mammendorf, p. 553-576.

Proceedings Papers:

Surname 1, Initials, Surname 2, Initials (year). Paper title. Proceedings title, pages.

- [4] Štefanič, N., Martinčević-Mikić, S., Tošanović, N. (2009). Applied lean system in process industry. *MOTSP Conference Proceedings*, p. 422-427.

Standards:

Standard-Code (year). Title. Organisation. Place.

- [5] ISO/DIS 16000-6.2:2002. *Indoor Air - Part 6: Determination of Volatile Organic Compounds in Indoor and Chamber Air by Active Sampling on TENAX TA Sorbent, Thermal Desorption and Gas Chromatography using MSD/FID*. International Organization for Standardization. Geneva.

WWW pages:

Surname, Initials or Company name. Title, from <http://address>, date of access.

- [6] Rockwell Automation. Arena, from <http://www.arenasimulation.com>, accessed on 2009-09-07.

EXTENDED ABSTRACT:

When the paper is accepted for publishing, the authors will be requested to send an **extended abstract** (approx. one A4 page or 3500 to 4000 characters). The instruction for composing the extended abstract are published on-line: <http://www.sv-jme.eu/information-for-authors/>.

COPYRIGHT:

Authors submitting a manuscript do so on the understanding that the work has not been published before, is not being considered for publication elsewhere and has been read and approved by all authors. The submission of the manuscript by the authors means that the authors automatically agree to transfer copyright to SV-JME when the manuscript is accepted for publication. All accepted manuscripts must be accompanied by a Copyright Transfer Agreement, which should be sent to the editor. The work should be original work by the authors and not be published elsewhere in any language without the written consent of the publisher. The proof will be sent to the author showing the final layout of the article. Proof correction must be minimal and executed quickly. Thus it is essential that manuscripts are accurate when submitted. Authors can track the status of their accepted articles on <http://en.sv-jme.eu/>.

PUBLICATION FEE:

Authors will be asked to pay a publication fee for each article prior to the article appearing in the journal. However, this fee only needs to be paid after the article has been accepted for publishing. The fee is 380 EUR (for articles with maximum of 6 pages), 470 EUR (for articles with maximum of 10 pages), plus 50 EUR for each additional page. The additional cost for a color page is 90.00 EUR. These fees do not include tax.

Strojniški vestnik - Journal of Mechanical Engineering
Aškerčeva 6, 1000 Ljubljana, Slovenia,
e-mail: info@sv-jme.eu



<http://www.sv-jme.eu>

Contents

Papers

- 471 Janez Luznar, Janko Slavič, Miha Boltežar:
Structure Borne Noise at PWM Excitation Using an Extended Field Reconstruction Method and Modal Decomposition
- 482 Mario Sokac, Djordje Vukelic, Zivana Jakovljevic, Zeljko Santosi, Miodrag Hadzistevic, Igor Budak:
Fuzzy Hybrid Method for the Reconstruction of 3D Models Based on CT/MRI Data
- 495 Wojciech Depczyński:
Selected Microstructural and Mechanical Properties of Open-Cell Metal Foams
- 503 Shahin Ghanbari, Kourosh Javaherdeh:
Experimental Assessment of Turbulence Convective Heat Transfer and Pressure Drop in Annuli Using Nanoporous Graphene Non-Newtonian Nanofluid
- 515 Min Song, Hongliang Wang, Haiou Liu, Pai Peng, Xianhui Wang, Dawei Pi, Chen Yang, Gang He:
Double-layer Control of an Automatic Mechanical Transmission Clutch during Commercial Vehicle Start-up
- 525 Branko Nečemer, Matej Vesenjok, Srečko Glodež:
Fatigue of Cellular Structures – a Review